

POLITECNICO DI MILANO  
SCUOLA DI INGEGNERIA INDUSTRIALE E DELL'INFORMAZIONE  
LAUREA MAGISTRALE IN INGEGNERIA MATEMATICA



# **3D Finite Element Drift-Diffusion Simulation of Semiconductor Devices**

Relatore: Prof. Riccardo SACCO  
Correlatore: Dott. Aurelio MAURI

Tesi di Laurea di:  
Andrea BORTOLOSSI  
Matr. n. 783023

Anno Accademico 2013–2014



# Contents

<b>Estratto della tesi</b>	<b>ix</b>
<b>Introduction</b>	<b>xi</b>
<b>1 Physical models for charge transport in semiconductor material</b>	<b>1</b>
1.1 Basic Device Physics . . . . .	1
1.1.1 Intrinsic semiconductor . . . . .	1
1.1.2 Extrinsic semiconductor . . . . .	4
1.1.3 Carrier densities at nonequilibrium condition . . . . .	7
1.1.4 Carrier transport in a semiconductor . . . . .	7
1.2 Drift Diffusion Model for semiconductors . . . . .	10
1.2.1 Drift Diffusion formulation . . . . .	11
1.2.2 Generation and Recombination phenomenon . . . . .	12
1.2.3 Mobility models . . . . .	15
<b>2 Solution of the DD system</b>	<b>19</b>
2.1 Geometry and boundary conditions . . . . .	19
2.2 Iteration algorithms . . . . .	22
2.2.1 Newton's method . . . . .	23
2.2.2 Fully coupled Newton's method . . . . .	25
2.2.3 Gummel map algorithm . . . . .	25
<b>3 Finite element discretization</b>	<b>29</b>
3.1 Non Linear Poisson Equation: weak form . . . . .	29
3.2 Continuity Equations: weak form . . . . .	31
3.3 Numerical approximation . . . . .	32
3.3.1 Geometrical discretization . . . . .	33
3.3.2 Linearized Non Linear Poisson equation . . . . .	34
3.3.3 Continuity equations . . . . .	39

<b>4</b>	<b>Simulation results</b>	<b>43</b>
4.1	Test cases . . . . .	43
4.1.1	p-n junction . . . . .	43
4.1.2	p-n junction in oxide . . . . .	50
4.1.3	n-channel MOSFET . . . . .	56
4.2	Current evaluation at the Ohmic contacts . . . . .	64
4.2.1	Simulation results . . . . .	66
<b>5</b>	<b>The current calculation problem</b>	<b>79</b>
5.1	Drift-Diffusion formula . . . . .	79
5.2	Edge average techniques . . . . .	81
5.2.1	Scharfetter-Gummel 1D . . . . .	81
5.2.2	Scharfetter-Gummel 2D . . . . .	82
5.2.3	Scharfetter-Gummel 3D . . . . .	83
5.3	Upwinding techniques . . . . .	86
5.3.1	Results . . . . .	89
	<b>Conclusions and future work</b>	<b>93</b>
	<b>Bibliografia</b>	<b>94</b>
	<b>Ringraziamenti</b>	<b>99</b>

# List of Figures

1.1	Two typical examples of state density occupation ( $g(E)$ ) and probability distribution ( $f(E)$ ). . . . .	2
1.2	Construction of the band diagram. . . . .	5
1.3	Band diagrams of extrinsic silicon for (1.18) and (1.19). . . . .	6
2.1	(a) MOS device with net dopant concentration distributed according to a gaussian profile and $\Gamma_D$ colored in black. The oxide layer is colored in light blue. (b) Outline of the MOS device with $\Gamma_{int}$ in light gray. . . . .	20
2.2	Flow chart of Gummel. . . . .	27
3.1	(a) Number of iteration against residual for different voltages in a diode test case. (b) Magnitude of the damping parameter $t_k$ . . . . .	38
3.2	Evaluation of the Zikatanov condition over a simple partition. Red elements do not satisfy condition (3.36) over four edges while blue elements fully satisfy the criterion. . . . .	41
4.1	p-n junction. . . . .	44
4.2	1D plots of the solutions and the quasi fermi potential levels along the line parallel to the Z-axis and placed at the center of the device. On the left is presented the test case at $V_A = 0.3[V]$ while on the right at $V_A = 1.0[V]$ . . . . .	45
4.3	p-n junction 0.3[V] - Electrostatic Potential. . . . .	46
4.4	p-n junction 0.3[V] - Electron density. . . . .	46
4.5	p-n junction 0.3[V] - Hole density. . . . .	46
4.6	p-n junction 1.0[V] - Electrostatic Potential. . . . .	47
4.7	p-n junction 1.0[V] - Electron density. . . . .	47
4.8	p-n junction 1.0[V] - Hole density. . . . .	47
4.9	Total time Gummel Map. . . . .	48

4.10	Time to solve the NLP and DD equations, and number of iterations of the Gummel map. . . . .	49
4.11	Initial guess for different bias compared with the final solution. . . . .	49
4.12	Test case p-n junction in oxide. . . . .	50
4.13	1D plots of the solutions and the quasi Fermi potential levels along the line parallel to the Z-axis and placed at the center of the device. On the left test case at $V_A = 0.3[V]$ is reported while on the right at $V_A = 1.0[V]$ . . . . .	51
4.14	p-n junction in oxide 0.3[V] - ElectrostaticPotential. . . . .	52
4.15	p-n junction in oxide 0.3[V] - Electron density. . . . .	52
4.16	p-n junction in oxide 0.3[V] - Hole density. . . . .	52
4.17	p-n junction in oxide 1.0[V] - Electrostatic Potential. . . . .	53
4.18	p-n junction in oxide 1.0[V] - Electron density. . . . .	53
4.19	p-n junction in oxide 1.0[V] - Hole density. . . . .	53
4.20	Test case dide p-n in oxide 0.3[V] - Electric field. . . . .	54
4.21	$E_y$ along a line parallel to Y-axis, $z = 0.22[\mu m]$ and $x = 0.1[\mu m]$ . . . . .	55
4.22	Geometry of a n-channel MOSFET. . . . .	56
4.23	Energy band levels for a n-MOSFET along the channel. . . . .	57
4.24	Channel of the n-MOSFET. . . . .	58
4.25	Electric field - $V_G = 2.0[V]$ . . . . .	58
4.26	Electrostatic potential - $V_G = 0.0[V]$ . . . . .	59
4.27	Electron density - $V_G = 0.0[V]$ . . . . .	59
4.28	Hole density - $V_G = 0.0[V]$ . . . . .	59
4.29	Electrostatic potential - $V_G = 2.0[V]$ . . . . .	60
4.30	Electron density - $V_G = 2.0[V]$ . . . . .	60
4.31	Hole density - $V_G = 2.0[V]$ . . . . .	60
4.32	Negative carriers spots for the electron density solution. . . . .	62
4.33	Electron density with finer mesh. . . . .	62
4.34	Zikatanov condition. . . . .	62
4.35	Electrostatic potential - Reverse bias. . . . .	63
4.36	Hole density - Reverse bias. . . . .	63
4.37	Diode characteristic. . . . .	67
4.38	SRH and Auger RG contribution. . . . .	67
4.39	p-n junction in oxide current at contact - Forward bias. . . . .	68
4.40	p-MOSFET. . . . .	70
4.41	$I_D - V_G$ n-MOSFET characteristic - mobility models. . . . .	71
4.42	$I_S - V_G$ p-MOSFET characteristic - mobility models. . . . .	72
4.43	$I_D - V_G$ n-MOSFET - several drain voltages. . . . .	74
4.44	$I_S - V_G$ p-MOSFET - several source voltages. . . . .	74
4.45	pMOSFET mesh. . . . .	76

4.46	Contribution of the impact ionization with the Van Over- straeten - de Man model inside the n-MOSFET $V_D = 0.5[V]$ . .	77
4.47	Contribution of the impact ionization with the Van Over- straeten - de Man model inside the p-MOSFET $V_S = 0.5[V]$ . .	77
4.48	Contribution of the impact ionization with the Van Over- straeten - de Man model inside the p-MOSFET $V_S = 1.2[V]$ . .	77
4.49	Reverse bias of the n-MOSFET. . . . .	78
4.50	Reverse bias of the p-MOSFET. . . . .	78
5.1	Effect of high electric field over the current density of electron.	82
5.2	1D plot p-n junction - $V_A = 1.0[V]$ . . . . .	90
5.3	1D plot p-n junction - $V_A = 1.0[V]$ . . . . .	91
5.4	1D plot p-n junction - $V_A = 1.0[V]$ . . . . .	91
5.5	1D plot p-n junction - $V_A = 1.0[V]$ . . . . .	92





# List of Tables

1.1	List of parameters in the Shockley-Read-Hall generation/recombination model. . . . .	14
1.2	List of parameters in Auger generation/recombination model. . . . .	15
1.3	List of parameters in van Overstraeten-de Man model. . . . .	16
1.4	List of parameters for mobility models including scattering from lattice thermal vibrations. . . . .	16
1.5	List of parameters for models including scattering from ionized dopant impurities. . . . .	17
1.6	List of parameters for mobility models including scattering from velocity saturation. . . . .	18
4.1	p-n junction - list of settings, parameters and models. . . . .	44
4.2	p-n junction in oxide - list of settings, parameters and models. . . . .	50
4.3	n-MOSFET - list of settings, parameters and models. . . . .	57
4.4	n-MOSFET (reverse bias) - list of settings, parameters and models. . . . .	61
4.5	p-n junction (characteristic) - list of settings, parameters and models. . . . .	66
4.6	p-n junction in oxide - list of settings, parameters and models. . . . .	69
4.7	n-MOSFET (low drain bias characteristic) - list of settings, parameters and models. . . . .	71
4.8	pMOSFET (low drain bias characteristic) - list of settings, parameters and models. . . . .	72
4.9	n-MOSFET (different drain bias) - list of settings, parameters and models. . . . .	73
4.10	p-MOSFET (different drain bias) - list of settings, parameters and models. . . . .	73
4.11	n-MOSFET (off-state characteristic) - list of settings, parameters and models. . . . .	76
4.12	p-MOSFET (off-state characteristic) - list of settings, parameters and models. . . . .	76



# Estratto della tesi

Nel 1947 John Bardeen, William Shockley e Walter Brattain inventarono il transistor bipolare dando inizio ad una crescita esponenziale delle industrie di dispositivi a semiconduttore. Prima di raggiungere le funzionalità dei dispositivi moderni alcuni passi fondamentali sono stati fatti: nel 1958 venne prodotto il primo circuito integrato (IC), seguito dall'introduzione del MOSFET (1960) e dal CMOS (1963). Queste prime scoperte portarono all'invenzione del primo microprocessore (1971): da allora un incessante sviluppo ed una continua opera di miniaturizzazione di tali dispositivi, hanno portato le industrie di microelettronica alla soglia della VLSI era (Very-Large-Scale-Integration).

Negli ultimi trenta anni questo processo ha garantito performance superiori e riduzione dei costi della produzione dei moderni computer, unità wireless e sistemi di comunicazione, influenzando drasticamente lo stile di vita odierno.

Gli investimenti spesi nello sviluppo delle tecnologie VLSI, costituiscono ancora oggi una forza trainante nello sviluppo di dispositivi ad alta densità di integrazione e superiore velocità di risposta.

In questo ambiente dove la ricerca e le dinamiche aziendali si incontrano, l'obiettivo delle simulazioni numeriche è la comprensione dei fenomeni fisici che governano il funzionamento dei moderni dispositivi.

Il progetto FEMOS (*Finite Element Method Oriented Solver*) è stato progettato al fine di simulare le interazioni fra i diversi fenomeni che caratterizzano il funzionamento dei più moderni dispositivi. All'interno di FEMOS sono già presenti i moduli che si occupano delle dinamiche chimiche, meccaniche e termiche. In questo lavoro di tesi abbiamo sviluppato la parte relativa ai semiconduttori.

Nel primo capitolo richiamiamo brevemente le proprietà fisiche dei semiconduttori ed enunciamo le principali relazioni che intercorrono fra le grandezze fondamentali (potenziale elettrostatico, campo elettrico, densità di portatori e di corrente). Presentiamo inoltre il modello Drift-Diffusion e alcuni dei principali modelli di mobilità dei portatori e dei fenomeni di generazione/ri-

combinazione.

Il secondo capitolo è diviso in due sezioni. Nella prima ci occupiamo di introdurre le geometrie considerate durante le simulazioni e le notazioni utilizzate. Nella seconda parte illustriamo gli algoritmi usati al fine di trattare il modello esposto nel primo capitolo.

Il terzo capitolo illustra la buona posizione delle equazioni trattate e i metodi utilizzati per discretizzarle.

Il quarto capitolo contiene i risultati ottenuti su dispositivi a semiconduttore tipici (diodo, MOSFET). La validazione dei risultati è stata condotta confrontandosi con un software commerciale (SDEVICE). La parte finale del capitolo riguarda l'estensione del metodo dei residui al caso 3D per il calcolo della corrente di contatto [GS74].

# Introduction

In 1947 John Bardeen, William Shockley and Walter Brattain (three scientists of Bell Telephone Labs) invented the bipolar transistor and since that crucial point there has been a growth of the semiconductor industry never known before, with serious impact on the way people work and live today.

Before reach the functionality and the miniaturization of modern devices, some fundamental steps has been made. In 1958 the first integrated circuits (IC) was produced, followed by the introduction of the first MOSFET(1960) and CMOS(1963). Into these inventions the first micro-processor(1971) sank his roots and since that time until present, an ever-increasing progress has continued, according to the indication of *Moore's Law* (formulated by Gordon Moore in 1965).

These events led microelectronic industry at the doors of the VLSI era (Very-Large-Scale-Integration). Indeed in the last thirty years the benefits of miniaturization have been the key in the evolutionary progress leading to today's computers, wireless units, and communication systems that offer superior performance, dramatically reduced cost per function, and much reduced physical size.

The large worldwide investment in VLSI technology constitutes a formidable driving force that guarantee the continued progress in IC integration density and speed, for as long as physical principles will allow.

From this point we want start and remark that the aim of numerical simulations is the comprehension of the physical phenomenon which lies behind the function of modern device.

Even if many commercial software are able to resolve different physic situations, they are often specialized on particular physic branch: obviously this strategic choice guarantees more efficiency but it implies a lost in generality. The consequence is that the work of device engineer becomes harder when he had to analyze electrical response coming from different phenomena.

Let us consider, as example, the functionality of a new device, which its electric behaviour is strong influenced by its mechanical response. Basically you are interested to the resolution of Maxwell's law (which is well

performed by SDEVICE simulator) and the Navier-Lamè equations (which is well performed by COMSOL simulator). Now the question is: how to put in communication the different outputs? Because it's not possible known precisely how the above programs resolves the equations, a relevant risk occurs when you decide to combine the solutions. In other words the development of an own code is at least desirable and possibly helpful: the main advantage is the control on simulation procedure and the possibility of fully customization, the major drawback is that this requires time and human resources, which in many cases are not available.

The FEMOS project (*Finite Element Method Oriented Solver*) tries to overcome the above limitations. FEMOS is designed for the treatment of chemical, mechanical, thermal and fluid phenomena. In this project we can't avoid the treatment of the classical semiconductor devices, this thesis found its origin in the development of this achievement.

In the first chapter we briefly recall the semiconductor material properties, physical behaviours and relations between the fundamental quantity (e.g. electrostatic potential, electric field, carrier densities and current densities). The classical Drift-Diffusion model has been detailed discussed; with the needed models for carrier mobility and generation/recombination phenomena.

The second chapter consists of two main sections. The first one presents the geometry framework and introduce some useful notations. The second one illustrates the algorithms used in order to treat the equations of the first chapter (decoupled Gummel map approach).

The third chapter the well-posedness analysis and the numerical approximation of the equations has been detailed discussed.

The fourth chapter contains numerical results of the simulations of typical test case (diode, MOS). The tests are compared with the results of a commercial code (SDEVICE). At the end the calculation of the current at contacts have been performed, extending the *residual method* [GS74] in the 3D case.

The fifth chapter **capitolo ancora in fase di costruzione.**

# Chapter 1

## Physical models for charge transport in semiconductor material

In this chapter we present the basic physical properties of semiconductor materials according with the quantum mechanics theory [YT09] and the Drift-Diffusion model [Jac84].

### 1.1 Basic Device Physics

As the most used material in the fabrication of VLSI devices is silicon, the description of physics is based on this material choice.

#### 1.1.1 Intrinsic semiconductor

In a silicon crystal each atom has four valence electrons to share with its four nearest neighboring atoms. The valence electrons are shared in a paired configuration called covalent bond. The quantum mechanical description of electrons in a solid, is that the allowed energy levels of electrons are grouped into bands separated by regions of not allowed energy, the so-called forbidden gaps. The highest energy band completely filled by electrons at 0[K] is called the *valence band* ( $E_V$ ), the next energy band levels are called *conduction band* ( $E_C$ ).

Because in silicon the band gap is 1.11 [eV] [BGB00] also at room temperature a small fraction of the electrons are excited into the conduction band, leaving behind vacancies (called *holes*) in the valence band. In contrast, an insulator has a much larger forbidden gap making room-temperature conduc-

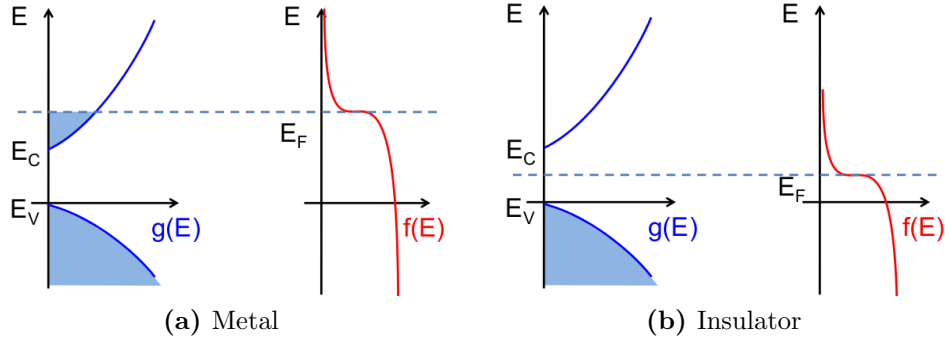


**Figure 1.1:** Two typical examples of state density occupation ( $g(E)$ ) and probability distribution ( $f(E)$ ).

tion virtually impossible, while metals have partially filled conduction bands even at absolute zero temperature, making them excellent conductors at any temperature.

A suitable formulation of the electron concentration in the conduction band is given by the following integral

$$n = \int_{E_c}^{\infty} g(E)f(E) dE \quad (1.1)$$

where  $g(E)dE$  represents the number of electronic states per unit volume with an energy between  $E$  and  $E + dE$  in the conduction band and  $f(E)$  is the *Fermi-Dirac distribution function*, which gives the probability that an electronic state at energy  $E$  is occupied by an electron,

$$f_D(E) = \frac{1}{1 + \exp\left(\frac{E - E_f}{k_B T}\right)}. \quad (1.2)$$

In (1.2)  $k_B = 1.38 \times 10^{-23}[J/K]$  is Boltzmann's constant,  $T$  is the absolute temperature and  $E_f$  is the *Fermi level*. Fig.1.1 shows the state density occupation  $g(E)$  and the probability distribution  $f(E)$  for a metal and a semiconductor. Because the emission of electrons are located mainly at the bottom of the conduction band, in order to obtain an analytic formula for the state density occupation  $g(E)$ , we can consider the following parabolic approximation of the conduction band

$$E = E_c + \frac{\hbar^2}{2m_e^*} k^2 \quad (1.3)$$

where  $\hbar = h/2\pi$  and  $h = 6.63 \times 10^{-34}[Js]$  is Planck's constant,  $m_e^*$  is the electron effective mass,  $E_c$  is the minimum value of the conduction band



and  $k$  is the wavenumber. This approach is well described in [PN] and the resulting formula for the conduction band density of states is

$$g(E) = \frac{m_e^* \sqrt{2m_e^*(E - E_c)}}{\pi^2 \hbar^3}. \quad (1.4)$$

In general (1.1) is a Fermi integral of order  $1/2$  and must be evaluated numerically.

**Definition 1.1.** The Fermi level ( $E_f$ ) is the energy at which the probability of occupation of an energy state by an electron is equal to  $1/2$ .

In most cases, when the energy is at least several  $k_B T$  above or below the Fermi level (case of non degenerate semiconductor), equation (1.2) can be well approximated by the Maxwell-Boltzmann statistics for classical particles, which reads as follows:

$$f_D(E) \simeq f_{MB}(E) = \begin{cases} \exp\left(-\frac{E - E_f}{k_B T}\right) & E \gg E_f \\ 1 - \exp\left(-\frac{E_f - E}{k_B T}\right) & E \ll E_f. \end{cases} \quad (1.5)$$

The Fermi level plays an essential role in characterizing the equilibrium state of a system. With this regard it is important to keep in mind the following observation.

*Observation 1.1.* When two systems in intimate contact are in thermal equilibrium with no current flow between them, their Fermi levels must be equal: in other words for a continuous region (of metals or semiconductors in contact), the Fermi level at thermal equilibrium is flat (spatially constant throughout the region).

Replacing (1.5) and (1.4) into (1.1) we obtain

$$n = N_c \exp\left(-\frac{E_c - E_f}{k_B T}\right). \quad (1.6)$$

Formulas similar to (1.1) and (1.4) can be used to compute the hole concentration  $p$  in the valence band and find

$$p = N_v \exp\left(-\frac{E_f - E_v}{k_B T}\right). \quad (1.7)$$

$N_c$  and  $N_v$  are the *effective density of states* while  $E_v$  is the maximum value of the valence band. In an intrinsic semiconductor  $n = p$  and the *intrinsic Fermi level*  $E_i$  can be calculated using equations (1.6) and (1.7) to get:

$$E_i = E_f = \frac{E_c + E_v}{2} - \frac{k_B T}{2} \ln \left( \frac{N_c}{N_v} \right). \quad (1.8)$$

By replacing (1.8) in (1.6) we determine the expression of the intrinsic carrier concentration  $n_i = n = p$

$$n_i = \sqrt{N_c N_v} \exp \left( -\frac{E_g}{2k_B T} \right) \quad (1.9)$$

where  $E_g = E_c - E_v$  is the semiconductor energy gap.

*Observation 1.2.* Since the thermal energy,  $k_B T$  is much smaller than the usual semiconductor bandgap  $E_g$ , the intrinsic Fermi level is very close to the midpoint between the conduction band and the valence band (called midgap energy level).

Equations (1.6) and (1.7) can be rewritten in terms of the intrinsic carrier density ( $n_i$ ) and energy ( $E_i$ ) :

$$n = n_i \exp \left( \frac{E_f - E_i}{k_B T} \right) \quad (1.10)$$

$$p = n_i \exp \left( \frac{E_i - E_f}{k_B T} \right). \quad (1.11)$$

Finally we remark a fundamental relation that holds at thermal equilibrium

$$np = n_i^2. \quad (1.12)$$

This relation is usually referred to the *mass action law*.

The analysis of the work principles of devices can be effectively done by the band diagram (Fig.1.2), which summarizes the information presented above.

### 1.1.2 Extrinsic semiconductor

At room temperature an intrinsic semiconductor has an extremely low free-carrier concentration, therefore, its resistivity is very high. In order to improve the conductivity of the semiconductor, impurities atoms are added in the material. This introduce additional energy levels in the forbidden gap: these impurities are easily ionized adding either electrons to the conduction band or holes to the valence band, in such a way that the electrical conductivity is dominated by the type and concentration of the impurity atoms.

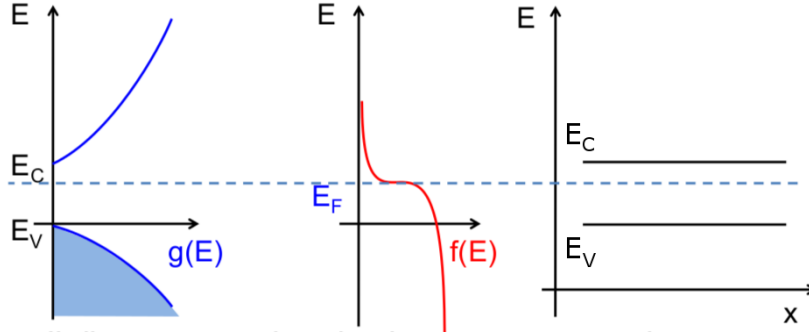


**Figure 1.2:** Construction of the band diagram.

In the case of silicon two are the types of impurities which are electrically active: those from column V of the Periodic Table such as arsenic or phosphorus, and those from column III such as boron or indium.

In most cases, the thermal energy at room temperature is sufficient to ionize the impurities and free the extra electron to the conduction band (column V) or accept an electron from valence band (column III). Column V impurities are called *donors*; they become positively charged when ionized. Silicon material doped with column-V impurities or donors is called *n-type* silicon.

Column III impurities are called *acceptors*: they become negatively charged when ionized. Silicon material doped with column-III impurities or acceptors is called *p-type* silicon.

A p-type or an n-type is named as *extrinsic* silicon. In terms of the energy-band diagram, donors add allowed electron states in the bandgap close to the conduction-band edge, while acceptors add allowed states just above the valence-band edge.

The Fermi level in n-type silicon moves up towards the conduction band while in p-type silicon it moves down towards the valence band. This behaviour is well depicted by the band diagrams presented in Fig.1.3. The exact position of the Fermi level depends on both the ionization energy and the concentration of dopants. For the sake of simplicity we consider that at room temperature all impurities are ionized ( $N_d = N_d^+$  and  $N_a = N_a^-$ ). For an n-type material with a donor impurity concentration,  $N_d$ , the charge neutrality condition requires that

$$n = N_d^+ + p \quad (1.13)$$

where  $N_d^+$  is the density of ionized donors. Similarly for a p-type material with acceptor impurity concentration  $N_a$  we have

$$p = N_a^- + n \quad (1.14)$$

Because the magnitude of impurities is between  $10^{16} \div 10^{20}[cm^{-3}]$ , and intrinsic carrier concentration in the order of  $10^{10}[cm^{-3}]$ , in typical case we can approximate the carrier concentrations as:

$$\begin{aligned} n &\simeq N_d^+, & p &\simeq \frac{n_i^2}{N_d^+} & (n - type) \\ p &\simeq N_a^-, & n &\simeq \frac{n_i^2}{N_a^-} & (p - type). \end{aligned} \quad (1.15)$$

Replacing (1.15) in (1.6) and (1.7) in (1.13) and (1.14) and solving the corresponding algebraic equation, we have:

$$E_c - E_f = k_B T \ln \left( \frac{N_c}{N_d^+} \right) \quad (1.16)$$

$$E_f - E_v = k_B T \ln \left( \frac{N_v}{N_a^-} \right). \quad (1.17)$$

Equation (1.16) and (1.17) can be written in a more useful form using (1.9) and (1.8) (for  $n_i$  and  $E_i$ ):

$$E_f - E_i = k_B T \ln \left( \frac{N_d^+}{n_i} \right) \quad (1.18)$$

$$E_i - E_f = k_B T \ln \left( \frac{N_a^-}{n_i} \right). \quad (1.19)$$

*Observation 1.3.* The distance between the Fermi level and the intrinsic Fermi level (near the midgap) is a logarithmic function of doping concentration.

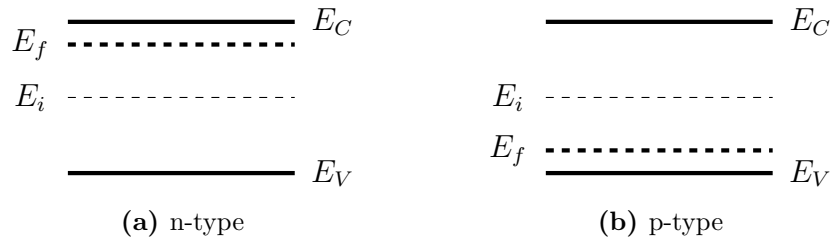


**Figure 1.3:** Band diagrams of extrinsic silicon for (1.18) and (1.19).

### 1.1.3 Carrier densities at nonequilibrium condition

In VLSI device a nonequilibrium condition is often possible where the densities of one or both types of carriers depart from their equilibrium values given by (1.10) and (1.11). In particular, the minority carrier concentration can be easily overwhelmed by injection from neighboring regions. Under these circumstances, while electrons and holes are in local equilibrium with themselves, they are not in equilibrium with each other. In order to extend the relationship between Fermi level and densities discussed above, we can introduce different Fermi levels for electrons and holes. They are called *quasi Fermi levels* defined as follows:

$$E_{fn} = E_i + k_B T \ln \left( \frac{n}{n_i} \right) \quad (1.20)$$

$$E_{fp} = E_i - k_B T \ln \left( \frac{p}{n_i} \right). \quad (1.21)$$

Considering the well known relation between electrostatic potential and energy  $\varphi = -E/q$ , (1.20) and (1.21) can be written as:

$$n = n_i \exp \left( \frac{\varphi_i - \varphi_n}{k_B T / q} \right) \quad (1.22)$$

$$p = n_i \exp \left( \frac{\varphi_p - \varphi_i}{k_B T / q} \right) \quad (1.23)$$

where  $\varphi_n$  and  $\varphi_p$  are the quasi Fermi electrostatic potential levels and  $\varphi_i$  is the midgap electrostatic potential level, while  $q = 1.602e^{-19}[C]$  is the elementary charge.

*Observation 1.4.* In non equilibrium condition quasi Fermi levels have the same physical interpretation in terms of the state occupancy as the Fermi level, therefore the electron (hole) density in the conduction band can be calculated using  $E_{fn}$  ( $E_{fp}$ ).

### 1.1.4 Carrier transport in a semiconductor

Carrier transport or current flow in silicon is driven by two different mechanisms:

- the **drift** of carriers, which is caused by the presence of an electric field;
- the **diffusion** of carriers, which is caused by a spatial gradient of electron or hole concentration.

### Drift current - Ohm's law

When an electric field is applied to a silicon device, the free carriers are accelerated and acquire a drift velocity superimposed upon their random thermal motion.

*Observation 1.5.* The drift velocity of holes ( $h$ ) is in the direction of the applied field, and the drift velocity of electrons ( $e$ ) is opposite to the field.

The velocity of the carriers does not increase indefinitely under field acceleration, since they are scattered frequently and lose their acquired momentum after each collision. During their motion throughout the lattice structure, carriers travel at an average speed defined by

$$\mathbf{v}_d^e = -\frac{q\mathbf{E}\tau_e}{m_e^*} \quad \mathbf{v}_d^h = +\frac{q\mathbf{E}\tau_h}{m_h^*} \quad (1.24)$$

where  $\mathbf{E}$  is the electric field,  $\tau_e, \tau_h$  are the average times between two consecutive scattering events and  $m_e^*, m_h^*$  are the effective masses of electron and hole respectively. The coefficient  $q\tau_e/m_e$  ( $q\tau_p/m_p$ ) characterizes how quickly a carrier can move through the lattice and is better known as carrier mobility [ $\text{cm}^2\text{V}^{-1}\text{s}^{-1}$ ]. In general, to include different scattering mechanisms to the mobility the *Matthiessen's rule* is used

$$\frac{1}{\mu} = \frac{1}{\mu_L} + \frac{1}{\mu_I} + \dots \quad (1.25)$$

where  $\mu_L$  and  $\mu_I$  correspond to the lattice and impurity scattering (for a more detailed description of mobility models see [YT09]).

Therefore the drift electron (hole) current density, reads as follows:

$$\mathbf{J}_n = -qn\mathbf{v}_d^n = qn\mu_n\mathbf{E} = \sigma_n\mathbf{E} \quad (1.26)$$

$$\mathbf{J}_p = +qp\mathbf{v}_d^p = qp\mu_p\mathbf{E} = \sigma_p\mathbf{E}. \quad (1.27)$$

The scalar coefficient  $qn\mu_n$  ( $qp\mu_p$ ) is called electron (hole) conductivity  $\sigma_n$  ( $\sigma_p$ ).

Relations (1.26) and (1.27) express the well known *Ohm's law* stating that the current density is directly proportional to the applied electric field.

### Diffusion current - Fick's law

In semiconductor devices it is very common to have different profiles of dopant in order to allow specifically targeted electrical behaviors. This implies a non uniform concentration of carriers which also diffuse as a result of

a concentration gradient. This leads to an additional current contribution accordingly to the classical *Fick's law*:

$$\mathbf{J}_n = -D_n(-q\nabla n) \quad (1.28)$$

$$\mathbf{J}_p = -D_p(+q\nabla p). \quad (1.29)$$

The constants  $D_n$  and  $D_p$  are called electron and hole diffusion coefficients and have units of  $[cm^2s^{-1}]$ . Drift and diffusion are closely associated with the random thermal motion of carriers and their collisions with the silicon lattice in thermal equilibrium. The *Einstein relation* (1.30) expresses the relation between diffusivity and mobility

$$D_n = \frac{k_B T}{q} \mu_n, \quad D_p = \frac{k_B T}{q} \mu_p. \quad (1.30)$$

### Drift-Diffusion transport equations

By considering (1.26), (1.27), (1.28) and (1.29), the electron and hole current densities become [Sie84]

$$\mathbf{J}_n = qn\mu_n\mathbf{E} + qD_n\nabla n \quad (1.31)$$

$$\mathbf{J}_p = qp\mu_p\mathbf{E} - qD_p\nabla p. \quad (1.32)$$

The total conduction current density is  $\mathbf{J} = \mathbf{J}_n + \mathbf{J}_p$ .

Equations (1.31) and (1.32) are called constitutive laws and they can be rewritten in two other ways highlighting different physical explanations of the same phenomenon. These reinterpretations give also different starting points for the discrete solver algorithm.

Considering that the electric field is related to the scalar potential through the quasi-static approximation

$$\mathbf{E} = -\nabla\varphi, \quad (1.33)$$

using (1.30) the current densities can be written as:

$$\mathbf{J}_n = -qn\mu_n \left( \nabla\varphi - \frac{k_B T}{qn} \nabla n \right) \quad (1.34)$$

$$\mathbf{J}_p = -qp\mu_p \left( \nabla\varphi + \frac{k_B T}{qp} \nabla p \right). \quad (1.35)$$

Considering equations (1.22) and (1.23) the above can be written as:

$$\mathbf{J}_n = -qn\mu_n \nabla \varphi_n \quad (1.36)$$

$$\mathbf{J}_p = -qp\mu_p \nabla \varphi_p. \quad (1.37)$$

With these equations we underly an important aspect which occurs in a semiconductor material:

*Observation 1.6.* The current density is proportional to the gradient of the quasi Fermi potential.

The third way to represent the current density is based on *Slotboom variables* which are particularly suited for the mathematical analysis of the semiconductor equations:

$$u_n = n_i \exp \left( -\frac{\varphi_n}{V_{th}} \right) \quad (1.38)$$

$$u_p = n_i \exp \left( \frac{\varphi_p}{V_{th}} \right) \quad (1.39)$$

where  $V_{th} = k_B T/q$ . Using the above equations into (1.31) and (1.32) we obtain:

$$\mathbf{J}_n = qD_n \exp \left( \frac{\varphi}{V_{th}} \right) \nabla u_n \quad (1.40)$$

$$\mathbf{J}_p = -qD_p \exp \left( -\frac{\varphi}{V_{th}} \right) \nabla u_p. \quad (1.41)$$

*Observation 1.7.* The drift-diffusion current density in a semiconductor is a purely diffusive flux of a new kind of carrier with a properly modified diffusion coefficient.

## 1.2 Drift Diffusion Model for semiconductors

The study of an integrated device works on several different scales, the *Drift Diffusion model* (DD) being the most widely used mathematical tool for industrial simulation. In this section we show how it is possible to deduce the DD model.



### 1.2.1 Drift Diffusion formulation

The system of Maxwell equations describes the propagation of electromagnetic signal in a medium [Jac84]:

$$\nabla \times \mathbf{H} = \mathbf{J} + \frac{\partial \mathbf{D}}{\partial t} \quad (1.42)$$

$$\nabla \times \mathbf{E} = -\frac{\partial \mathbf{B}}{\partial t} \quad (1.43)$$

$$\nabla \cdot \mathbf{D} = \rho \quad (1.44)$$

$$\nabla \cdot \mathbf{B} = 0 \quad (1.45)$$

with the following set of constitutive laws that characterize the electromagnetic properties of the medium:

$$\begin{aligned} \mathbf{D} &= \epsilon \mathbf{E} \\ \mathbf{B} &= \mu_m \mathbf{H} \end{aligned} \quad (1.46)$$

where  $\epsilon$  is the material dielectric permittivity [ $Fcm^{-1}$ ] and  $\mu_m$  is the magnetic permeability [ $Hcm^{-1}$ ]. Since  $\nabla \cdot (\nabla \times \mathbf{A}) = 0$  for any vector  $\mathbf{A}$ , (1.45) is satisfied by introducing a vector potential  $\mathbf{A}$  such that  $\mathbf{B} = \nabla \times \mathbf{A}$ . We replace it in (1.43) to obtain

$$\nabla \times \left( \mathbf{E} + \frac{\partial \mathbf{A}}{\partial t} \right) = 0. \quad (1.47)$$

From this we can state that there exists a scalar potential  $\varphi$  such that

$$\mathbf{E} + \frac{\partial \mathbf{A}}{\partial t} = -\nabla \varphi. \quad (1.48)$$

Applying the divergence operator and using (1.33), (1.46) and (1.44), relation (1.48) becomes

$$\rho + \frac{\partial \rho}{\partial t} = -\nabla \cdot (\epsilon \nabla \varphi). \quad (1.49)$$

We now assume that  $\frac{\partial \rho}{\partial t} = 0$  (quasi static approximation) and we have the *Poisson Equation*

$$\nabla \cdot (\epsilon \nabla \varphi) = \rho. \quad (1.50)$$

Applying the divergence operator to (1.42) we get the *Continuity Equation*

$$\frac{\partial \rho}{\partial t} + \nabla \cdot \mathbf{J} = 0. \quad (1.51)$$

To close system (1.50) (1.51), we need to specify the mathematical form of the electric charge density ( $\rho$ ) and the electric conduction current density ( $\mathbf{J}$ ). Considering (1.15)  $\rho$  can be expressed as

$$\rho = \underbrace{q(p - n)}_{\rho_{free}} + \underbrace{q(N_D - N_A)}_{\rho_{fixed}} \quad (1.52)$$

in which we can distinguish the two following contributions:

- free charge ( $\rho_{free}$ ) (free electron and holes carriers),
- fixed charge ( $\rho_{fixed}$ ) (ionized dopant impurities).

Notice that we assume  $N_D$  and  $N_A$  to be time invariant ( $\partial N_D / \partial t = \partial N_A / \partial t = 0$ ).

Splitting the continuity equation (1.51) into two distinct equations (for holes and electrons) Drift Diffusion (DD) model formulation reads as follows:

$$\left\{ \begin{array}{l} \nabla \cdot (-\epsilon \nabla \varphi) = q(p - n + N_D^+ - N_A^-) \\ -q \frac{\partial n}{\partial t} + \nabla \cdot (-q \mu_n n \nabla \varphi + q D_n \nabla n) = qR \\ q \frac{\partial p}{\partial t} + \nabla \cdot (-q \mu_p p \nabla \varphi - q D_p \nabla p) = -qR \end{array} \right. \quad (1.53)$$

where the arbitrarily introduced function  $R = R(\mathbf{x}, t)$  can be considered as the net rate of generation and recombination. The system is an incompletely parabolic initial value/boundary problem in three scalar unknown dependent variables  $\varphi(\mathbf{x}, t)$ ,  $n(\mathbf{x}, t)$  and  $p(\mathbf{x}, t)$ : the presence of the drift terms ( $n \nabla \varphi$  and  $p \nabla \varphi$ ) makes (1.53) a nonlinear coupled system of PDE's.

From Maxwell equations we are able to guarantee only that  $\mathbf{J}$  is a solenoidal field. The stationary form can be easily deduced from (1.53) by neglecting the temporal derivatives.

### 1.2.2 Generation and Recombination phenomenon

The modelling of  $R(\mathbf{x}, t)$  is fundamental for device simulation due to its important role in determining the current-voltage characteristic.

It is important to keep in mind that electrons and holes are in continuous fluctuation due to their thermal energy, but the macroscopic result is that the net recombination rate at equilibrium is identically zero. Our interest is to analyze the deviations from this condition.

While generation events are usually due to thermal agitation or an external input source the recombination events happen in order to neutralize an excess of charge.

The phenomenological model for the net recombination rate  $R$  is often given by

$$R(n, p) = (pn - n_i^2)F(n, p) \quad (1.54)$$

where  $F$  is a function accounting for specific recombination/generation (R/G) events. In the following we present the classical theory that includes three specific kind of contributions.

### Shockley-Read-Hall recombination (SRH)

Electron and hole generation and recombination can take place directly between the valence band and the conduction band, or mediated via trap centers in the energy gap. Shockley-Read-Hall phenomena is a two-particle process which mathematically expresses the probability that:

- an electron in the conduction band neutralizes a hole at the valence band through the mediation of an unoccupied trapping level located at the energy gap ( $R_{SRH}$ ),
- an electron is emitted from the valence band to the conduction band, through the mediation of an unoccupied trapping level located at the energy gap ( $G_{SRH}$ ).

The modeling function  $F$  is

$$F_{SRH}(n, p) = \frac{1}{\tau_n \left( p + n_i \cosh \left( \frac{E_T}{k_B T} \right) \right) + \tau_p \left( n + n_i \cosh \left( \frac{E_T}{k_B T} \right) \right)} \quad (1.55)$$

where  $E_T$  is the energy level of the traps,  $\tau_n$  and  $\tau_p$  are called *carrier lifetimes* and are physically defined as the reciprocals of the capture rates. The typical order of magnitude of the lifetimes lies in the range of  $10^{-3}\mu s \div 1\mu s$  (see [VOT83] and [GH92]).

Parameter	Unit	Electrons	Holes
$\tau$	s	$1.0 \times 10^{-5}$	$3.0 \times 10^{-6}$
$E_T$	eV	0.0	0.0

**Table 1.1:** List of parameters in the Shockley-Read-Hall generation/recombination model.

### Auger recombination (AU)

Auger R/G is a three-particle process and takes place directly between the valence band and the conduction band. We distinguish four cases which depend on the kind of carriers involved in the phenomena:

$R_{AU}^{2n,1p}$  a high-energy electron in the conduction band moves to the valence band where it neutralizes a hole, transmitting the excess energy to another electron in the conduction band;

$G_{AU}^{2n,1p}$  an electron in the valence band moves to the conduction band by taking the energy from a high energy electron in the conduction band and leaves a hole in the valence band;

$R_{AU}^{2p,1n}$  an electron in the conduction band moves to the valence band where it neutralizes a hole, transmitting the excess energy to another hole in the valence band;

$G_{AU}^{2p,1n}$  an electron in the valence band moves to the conduction band by taking the energy from a high energy hole in the valence band and leaves a hole in the valence band.

The modeling function  $F$  is

$$F_{AU}(n, p) = C_n n + C_p p \quad (1.56)$$

where the quantities  $C_n$  and  $C_p$  are the so called Auger capture coefficients typically in the order of magnitude of  $10^{-25}[cm^6 s^{-1}]$  [LH80]. Note that Auger R/G is relevant only when both carrier densities attain high values.

### Impact ionization (II)

The impact ionization mechanism is a three-particle phenomena where carrier generation is triggered by the presence of a high electric field: due to this field an electron could gain enough energy to excite an electron-hole pair out of a silicon lattice bond. Then the process can be repeated until an avalanche

Parameter	Unit	Magnitude
$C_n$	$cm^6 s^{-1}$	$2.9 \times 10^{-31}$
$C_p$	$cm^6 s^{-1}$	$1.028 \times 10^{-31}$

**Table 1.2:** List of parameters in Auger generation/recombination model.

of generated carriers is produced within the region: this process can not be described by a relation of the form (1.54).

Among the different formulations for the impact ionization generation we choose the van Overstraeten - de Man model [vOdM70], based on the Chynoweth law [Chy58]:

$$G_{II}(n, p) = \alpha_n n |\mathbf{v}_n| + \alpha_p p |\mathbf{v}_p| \quad (1.57)$$

where:

$$\alpha(E_{ava}) = \gamma \exp\left(-\frac{\gamma b}{E_{ava}}\right) \quad (1.58)$$

$$\gamma = \frac{\tanh\left(\frac{\hbar\omega_{op}}{2k_B T_0}\right)}{\tanh\left(\frac{\hbar\omega_{op}}{2k_B T}\right)} \quad (1.59)$$

where  $\hbar\omega_{op}$  is the phonon energy and  $\gamma$  expresses the temperature dependence of the phonon gas against which carriers are accelerated,  $E_{ava}$  is the driving force that can be computed as:

- the component of the electrostatic field in the direction of current flow

$$E_{ava}^{n,p} = \frac{\mathbf{E} \cdot \mathbf{J}_{n,p}}{||\mathbf{J}_{n,p}||} \quad (1.60)$$

- the module of the quasi fermi gradient

$$E_{ava}^{n,p} = |\nabla \varphi_{n,p}|. \quad (1.61)$$

### 1.2.3 Mobility models

In this section we illustrate the most common phenomenological models to describe carrier mobilities. The main physical phenomena underlying a mobility reduction are:

Parameter	Unit	Electrons	Holes	Valid range of electric field
$E_0$	$V\text{ cm}^{-1}$	$4.0 \times 10^5$	$4.0 \times 10^5$	
$a_{high}$	1	$7.03 \times 10^5$	$6.71 \times 10^5$	$E_0$ to $6.0 \times 10^5$
$a_{low}$	1	$7.03 \times 10^5$	$1.582 \times 10^6$	$1.75 \times 10^5$ to $E_0$
$b_{high}$	1	$1.231 \times 10^6$	$1.693 \times 10^6$	$E_0$ to $6.0 \times 10^5$
$b_{low}$	1	$1.231 \times 10^6$	$2.036 \times 10^6$	$1.75 \times 10^5$ to $E_0$
$\hbar\omega_{op}$	eV	0.063	0.063	

**Table 1.3:** List of parameters in van Overstraeten-de Man model.

- interaction with the silicon atoms (due to thermal vibrations);
- interaction with ionized dopant impurities in the crystal.

### Scattering with lattice

Carrier mobility is a decreasing function of temperature, as we expect collisions to become more and more frequent as  $T$  gets higher (see [Lom88]). This can be represented as follows

$$\mu_\nu^L = \mu_\nu^0 \left( \frac{T}{T_0} \right)^{-\beta_\nu} \quad \nu = n, p \quad (1.62)$$

where  $\mu_\nu^0$  is the low-field mobility,  $\beta_\nu$  are positive numbers and  $T_0$  is a reference temperature  $T_0 = 300[K]$ .

Parameter	Unit	Electrons	Holes
$\mu^0$	$cm^2V^{-1}s^{-1}$	1417.0	470.5
$\beta$	1	2.5	2.2

**Table 1.4:** List of parameters for mobility models including scattering from lattice thermal vibrations.

### Scattering from ionized impurities

Dopant ionized impurities represent local perturbations of the periodic silicon lattice, they strongly influence the carrier motion through electrostatic interaction, reducing the mobility. To take into account this physical effect the following model has been proposed in [MS83]

$$\mu = \mu_{min1} \exp\left(-\frac{P_c}{N_{tot}}\right) + \frac{\mu^L - \mu_{min2}}{1 + \left(\frac{N_{tot}}{C_r}\right)^\alpha} - \frac{\mu_1}{1 + \left(\frac{C_s}{N_{tot}}\right)^\beta} \quad (1.63)$$

where  $N_{tot} = N_D^+ + N_A^-$ ,  $\mu_\nu^L$  is given by (1.62),  $\mu_{min1}$  and  $\mu_{min2}$  are the minimum values of  $\mu$ ;  $P_c$ ,  $C_r$  and  $C_s$  are reference doping values.

Parameter	Unit	Electrons	Holes
$\mu_{min1}$	$cm^2V^{-1}s^{-1}$	52.2	44.9
$\mu_{min2}$	$cm^2V^{-1}s^{-1}$	52.2	0
$\mu_1$	$cm^2V^{-1}s^{-1}$	43.4	29.0
$P_c$	$cm^{-3}$	0	$9.23 \times 10^{16}$
$C_r$	$cm^{-3}$	$9.68 \times 10^{16}$	$2.23 \times 10^{17}$
$C_s$	$cm^{-3}$	$3.43 \times 10^{20}$	$6.10 \times 10^{20}$
$\alpha$	1	0.680	0.719
$\beta$	1	2.0	2.0

**Table 1.5:** List of parameters for models including scattering from ionized dopant impurities.

### Veclocity saturation at high electric field

Under the assumption of low electric field, mobilities are reasonably constant and the carrier drift velocity is proportional to the electric field. As the applied field strength increases, the above assumption predicts an unbounded carrier velocity as  $|\mathbf{E}| \rightarrow \infty$ . This outcome is physical incorrect, indeed at high fields carriers lose their energy by optical-phonon emission [YT09], resulting in a decrease of carrier velocity according to the following mathematical expression

$$\lim_{|\mathbf{E}| \rightarrow \infty} \mu|\mathbf{E}| = v_{sat}. \quad (1.64)$$

A common adopted formula is the *Canali model* [Can75] with temperature dependent parameters

$$\mu = \frac{\mu_L}{\left[1 + \left(\frac{\mu_L|\mathbf{E}|}{v_{sat}}\right)^\beta\right]^{1/\beta}} \quad (1.65)$$

where  $\mu_L$  is (1.62) while  $v_{sat}$  and  $\beta$  are given by

$$v_{sat} = v_0 \exp\left(\frac{300}{T}\right)^{v_{exp}} \quad \beta = \beta_0 \left(\frac{T}{300}\right)^{\beta_{exp}}. \quad (1.66)$$

where  $v_0$  and  $\beta_{exp}$  are fitting parameters.

Parameter	Unit	Electrons	Holes
$v_0$	$cm\ s^{-1}$	$1.07 \times 10^7$	$8.37 \times 10^6$
$v_{exp}$	1	0.87	0.52
$\beta_0$	1	1.109	1.213
$\beta_{exp}$	1	0.66	0.17

**Table 1.6:** List of parameters for mobility models including scattering from velocity saturation.



# Chapter 2

## Solution of the DD system

In this chapter we introduce geometry and boundary conditions for the stationary form of system (1.53) and we discuss the functional iteration algorithms used to decouple the problem.

### 2.1 Geometry and boundary conditions

In order to close the *Poisson equation* and the *Drift Diffusion equation* for electrons and holes in the stationary form of problem (1.53), suitable boundary conditions must be considered.

Let us consider the device domain as the union of two open disjoint subsets,  $\Omega_{Si}$  (doped silicon part), and  $\Omega_{ox}$  (oxide part), such that their intersection  $\partial\Omega_{Si} \cap \partial\Omega_{ox} = \Gamma_{int}$  is the interface. The oxide region  $\Omega_{ox}$  is assumed to be a perfect insulator so that:

$$\begin{aligned} n &= p = 0 \\ \mathbf{J}_n &= \mathbf{J}_p = \mathbf{0}. \end{aligned} \tag{2.1}$$

The device boundary  $\partial\Omega$  is divided into two disjoint subsets:  $\partial\Omega_c$  and  $\partial\Omega_a$ . The subset  $\partial\Omega_c$  includes the so called *ohmic contacts* (with ohmic contacts we define every electrical terminal of the device on which the external input voltages are applied). Ohmic contacts are assumed to be *ideal*, they are equipotential surfaces and no voltage drop occurs at the interface between the contact and the neighbouring domain. This is well represented by suitable Dirichlet boundary conditions, therefore in the following we set  $\partial\Omega_c = \Gamma_D$  and enforce:

$$\begin{aligned} \varphi &= \varphi_D \\ n &= n_D \\ p &= p_D \end{aligned} \quad \text{on } \Gamma_D. \tag{2.2}$$

We point that in the case of a perfect insulator domain, (2.2) reduces to the only condition on the electrostatical potential.

Artificial boundaries ( $\partial\Omega_a$ ) are needed in order to obtain a self-contained simulation domain. On these boundaries no electric and current flux is exchanged with the surrounding environment, this fact being well represented by homogeneous Neumann boundary conditions ( $\partial\Omega_a = \Gamma_N$ ):

$$\begin{aligned} \mathbf{D} \cdot \mathbf{n} &= 0 \\ \mathbf{J}_n \cdot \mathbf{n} &= 0 \\ \mathbf{J}_p \cdot \mathbf{n} &= 0 \end{aligned} \quad \text{on } \Gamma_N \quad (2.3)$$

where  $\mathbf{n}$  is the outward unit normal vector defined over  $\partial\Omega$ . As we noted before on  $\partial\Omega_{ox} \cap \Gamma_N$  condition (2.3) is reduced to the first equation.

When oxide is present the silicon boundaries for continuity equations become

$$\begin{aligned} \Gamma_{D,Si} &= \Gamma_D \cap \partial\Omega_{Si} \\ \Gamma_{N,Si} &= \Gamma_N \cap \partial\Omega_{Si} \cup \Gamma_{int}. \end{aligned} \quad (2.4)$$

Fig.2.1 shows an example of boundary setting for a MOS device: in Fig.2.1a contacts are colored in black and in Fig.2.1b with light gray we indicate the interface between oxide and silicon.

Thermodynamical equilibrium and charge neutrality are the physical characterizing conditions of an ideal contact. These conditions correspond to the

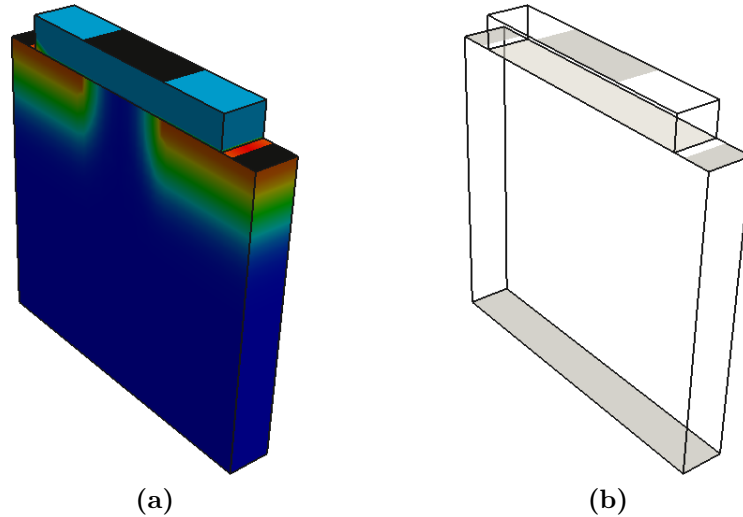


**Figure 2.1:** (a) MOS device with net dopant concentration distributed according to a gaussian profile and  $\Gamma_D$  colored in black. The oxide layer is colored in light blue. (b) Outline of the MOS device with  $\Gamma_{int}$  in light gray.

following algebraic system for  $n_D$  and  $p_D$ :

$$\begin{cases} p_D n_D &= n_i^2 \\ p_D - n_D + N_D - N_A &= 0 \end{cases} \quad (2.5)$$

Solving (2.5) on  $\Gamma_{D,Si}$  we have:

$$n_D = \frac{D + \sqrt{D^2 + 4n_i^2}}{2} \quad (2.6)$$

$$p_D = \frac{-D + \sqrt{D^2 + 4n_i^2}}{2} \quad (2.7)$$

where  $D := N_D^+ - N_A^-$  is the net doping concentration. Furthermore at each contact, the quasi Fermi potential levels of silicon are aligned with the external applied voltage  $V_{ext}$

$$\varphi_n = \varphi_p = \varphi_f = V_{ext}. \quad (2.8)$$

where  $\varphi_f = -E_f/q$  is the unique quasi Fermi potential level defined at the contacts. As a consequence, we can easily determine potential condition on  $\Gamma_{D,Si}$  using (1.10) and (1.11)

$$\varphi_D = \varphi_f + V_{th} \ln \left( \frac{n_D}{n_i} \right) = \varphi_f - V_{th} \ln \left( \frac{p_D}{n_i} \right) \quad (2.9)$$

When  $\Omega_{ox} \neq \emptyset$  we set  $\varphi_D$  equal to the external applied voltage on  $\Gamma_D/\Gamma_{D,Si}$ .

The stationary form of (1.53) can be now written in closed form as:

$$\begin{aligned} -\Delta \epsilon \varphi - q(p - n) &= qD & \text{in } \Omega = \Omega_{ox} \cup \Omega_{Si} \\ \varphi &= \varphi_D & \text{on } \Gamma_D \\ \nabla \varphi \cdot \mathbf{n} &= 0 & \text{on } \Gamma_N \\ \\ \nabla \cdot (q\mu_n n \nabla \varphi - qD_n \nabla n) &= -qR & \text{in } \Omega_{Si} \\ n &= n_D & \text{on } \Gamma_{D,Si} \\ \nabla n \cdot \mathbf{n} &= 0 & \text{on } \Gamma_{N,Si} \\ \\ \nabla \cdot (-q\mu_p p \nabla \varphi - qD_p \nabla p) &= -qR & \text{in } \Omega_{Si} \\ p &= p_D & \text{on } \Gamma_{D,Si} \\ \nabla p \cdot \mathbf{n} &= 0 & \text{on } \Gamma_{N,Si}. \end{aligned} \quad (2.10)$$

The highly nonlinear coupled nature of system (2.10) makes an analytical treatment very difficult, if not even impossible. For this reason, numerical schemes must be used to compute an approximate solution.

## 2.2 Iteration algorithms

The most used algorithms for the iterative treatment of (2.10) are *the fully coupled Newton's method* and *the decoupled Gummel map*. System (2.10) can be written in compact form as

$$\mathbf{F}(\mathbf{U}) = \mathbf{0} \quad (2.11)$$

where

$$\mathbf{U} := [\varphi, n, p]^T, \quad \mathbf{F}(\mathbf{U}) := \begin{bmatrix} F_1(\mathbf{U}) \\ F_2(\mathbf{U}) \\ F_3(\mathbf{U}) \end{bmatrix} \quad (2.12)$$

and having set:

$$\begin{aligned} F_1(\mathbf{U}) &= \nabla \cdot (-\epsilon \nabla \varphi) - q(p - n + D) \\ F_2(\mathbf{U}) &= \nabla \cdot (q\mu_n n \nabla \varphi - qD_n \nabla n) + qR \\ F_3(\mathbf{U}) &= \nabla \cdot (-q\mu_p p \nabla \varphi - qD_p \nabla p) + qR. \end{aligned}$$

Problem (2.11) is the generalization of the search of a zero for a real function  $f : \mathbb{R} \rightarrow \mathbb{R}$ . Because the vector function  $\mathbf{F}$  is a nonlinear differential operator, the associated problem which we intend to solve is: given a functional space  $V$  and the operator  $\mathbf{F} : V \rightarrow V$ , find  $\mathbf{U} \in V$  such that (2.11) is satisfied.

In our application, the function space  $V$  is typically a subset of the Sobolev space  $[H^1(\Omega)]^d$  (where  $d$  is the number of component of  $\mathbf{F}$ ). The general form of a Sobolev space for an integer  $m \geq 0$  is

$$H^m(\Omega) := \{v : D^\alpha v \in L^2(\Omega), \forall |\alpha| \leq m\}. \quad (2.13)$$

where  $L^2(\Omega)$  is the space of square integrable functions on  $\Omega$  defined as

$$L^2(\Omega) := \left\{ v : \int_{\Omega} |v|^2 d\Omega = \|v\|_{L^2(\Omega)}^2 < +\infty \right\}. \quad (2.14)$$

On these space, we shall use the semi-norm

$$|v|_{m,\Omega}^2 = \sum_{|\alpha|=m} \|D^\alpha v\|_{L^2(\Omega)}^2 \quad (2.15)$$

and the norm

$$\|v\|_{m,\Omega}^2 = \sum_{k \leq m} |D^\alpha v|_{k,\Omega}^2. \quad (2.16)$$

We shall also need to consider functions that vanish on either the entire or a part of the boundary:

$$H_0^1 := \{v : v \in H^1(\Omega), v|_{\partial\Omega} = 0\} \quad (2.17)$$

$$H_{0,\Gamma_D}^1 := \{v : v \in H^1(\Omega), v|_{\Gamma_D} = 0\} \quad (2.18)$$

For  $v \in H_0^1(\Omega), H_{0,\Gamma_D}^1(\Omega)$  we have the *Poincaré - Friedrich's inequality* [Sal10]

$$|v|_{0,\Omega} \leq C(\Omega)|v|_{1,\Omega} \quad (2.19)$$

from which it follows that the seminorm  $|\cdot|_\Omega$  is actually a norm in  $H^1(\Omega)$ , equivalent to  $\|\cdot\|_{1,\Omega}$ .

The above function spaces are used widely in the remainder of this work, especially during the well-posedness analysis as reported in Chapter 3 (for a more detailed description see [AF03]).

### 2.2.1 Newton's method

**Definition 2.1** (Frechét differentiability). Let be  $X$  and  $Y$  two vector spaces. Given  $f, g \in X$  and a functional  $F : X \rightarrow Y$ , the functional  $F$  is Frechét differentiable if there exists a linear bounded operator  $A_f : X \rightarrow Y$  such that

$$\lim_{\|g\| \rightarrow 0} \frac{\|F(f+g) - F(f) - A_f(g)\|_Y}{\|g\|_X} = 0, \quad (2.20)$$

where  $\|\cdot\|_X$  and  $\|\cdot\|_Y$  are the norms on  $X$  and  $Y$  respectively. If the above limit exists, we write  $DF(f) = A_f$  and call it the Frechét derivative of  $F$  at  $f$ .

Considering the functional operator (2.12) we can easily compute the associated *Jacobian matrix*  $\mathbf{F}'$ , whose  $(i, j)$ -th entry represents the Frechét derivative of the  $i$ -th row of the non linear operator with respect to the  $j$ -th variable, defined as

$$\mathbf{F}'_{ij}(\mathbf{U})[\mathbf{V}]_j := \lim_{\eta \rightarrow 0} \frac{F_i(\mathbf{U} + \eta[\mathbf{V}]_j) - F_i(\mathbf{U})}{\eta} \quad \mathbf{V} \in V \quad (2.21)$$

where  $[\mathbf{V}]_j \in V$  is the projection of  $\mathbf{V}$  in the  $j$ -th direction.

$\mathbf{F}'_{ij}(\cdot)$  is a linear operator from  $V$  into the space  $L(V, V)$  of linear continuous functionals from  $V$  into  $V$ , while  $\mathbf{F}'_{ij}(\mathbf{U})$  is the Frechét derivative of the functional  $F_i$  with respect the variable  $[\mathbf{U}]_j$ .

According to the above definitions the Newton method reads as follows:

**Newton's method**

Let  $X, Y$  be two vector spaces and  $\mathbf{F} : X \rightarrow Y$  a function operator Frechét differentiable, given an initial datum  $\mathbf{U}^0 \in X$  and  $toll > 0$ , for all  $k \geq 0$  solve the following linear problem:

$$\begin{aligned} \mathbf{F}'(\mathbf{U}^k)\delta\mathbf{U}^k &= -\mathbf{F}(\mathbf{U}^k) \\ \mathbf{U}^{k+1} &= \mathbf{U}^k + \delta\mathbf{U}^k \end{aligned} \quad (2.22)$$

until  $\|\mathbf{F}(\mathbf{U}^{k+1})\|_Y < toll$ .

The application of Newton's method has transformed the original problem (2.11) into the *fixed-point problem* of finding  $\mathbf{U} \in V$  such that

$$\mathbf{U} = T_{\mathbf{F}}(\mathbf{U}) \quad (2.23)$$

where

$$T_{\mathbf{F}}(\mathbf{U}) = \mathbf{F}'(\mathbf{U})^{-1}(\mathbf{F}'(\mathbf{U})\mathbf{U} - \mathbf{F}(\mathbf{U})) \quad (2.24)$$

is the *iteration function* associated with the Newton method. The main result about the convergence of this method is as follows.

**Theorem 2.1.** *Let  $\mathbf{U} \in V$  be a solution of problem (2.11). Assume that  $\mathbf{F}'$  is Lipschitz continuous in the ball  $\mathcal{B}(\mathbf{U}, \delta)$ , i.e., that there exists  $K > 0$  such that:*

$$\|\mathbf{F}'(\mathbf{v}) - \mathbf{F}'(\mathbf{z})\|_{L(V, V)} \leq K\|\mathbf{v} - \mathbf{z}\|_V \quad \forall \mathbf{v}, \mathbf{z} \in \mathcal{B}(\mathbf{U}, \delta), \mathbf{v} \neq \mathbf{z} \quad (2.25)$$

*Then there exists in correspondence  $\delta' > 0$ , with  $\delta' \leq \delta$ , such that for all  $\mathbf{U}^0 \in \mathcal{B}(\mathbf{U}, \delta')$  the sequence  $\{\mathbf{U}^k\}$  generated by (2.22) converges quadratically to  $\mathbf{U}$ , i.e., there exists  $C > 0$  such that, for a suitable  $k_0 \geq 0$  we have:*

$$\|\mathbf{U} - \mathbf{U}^{k+1}\|_V \leq C\|\mathbf{U} - \mathbf{U}^k\|_V^2 \quad \forall k \geq k_0 \quad (2.26)$$

### 2.2.2 Fully coupled Newton's method

If we consider the linearization of system (2.10) the Jacobian matrix of the Newton method is a 3x3 matrix and the associated problem is

$$\begin{bmatrix} F_{1,\varphi} & F_{1,n} & F_{1,p} \\ F_{2,\varphi} & F_{2,n} & F_{2,p} \\ F_{3,\varphi} & F_{3,n} & F_{3,p} \end{bmatrix} \begin{bmatrix} \delta\varphi \\ \delta n \\ \delta p \end{bmatrix} = \begin{bmatrix} -F_1(\varphi, n, p) \\ -F_2(\varphi, n, p) \\ -F_3(\varphi, n, p) \end{bmatrix}. \quad (2.27)$$

Each row of the above matrix is a PDE that can be discretized using the FEM. Denoting by  $N_{dof}$  the number of degrees of freedom (dofs) to represent  $\delta\varphi$ ,  $\delta n$  and  $\delta p$  we see that the structure of the discrete problem associated with (2.27) is the following linear algebraic system

$$\begin{bmatrix} \mathbf{K}_{1,\varphi} & \mathbf{K}_{1,n} & \mathbf{K}_{1,p} \\ \mathbf{K}_{2,\varphi} & \mathbf{K}_{2,n} & \mathbf{K}_{2,p} \\ \mathbf{K}_{3,\varphi} & \mathbf{K}_{3,n} & \mathbf{K}_{3,p} \end{bmatrix} \begin{bmatrix} \delta\varphi \\ \delta n \\ \delta p \end{bmatrix} = \begin{bmatrix} -\mathbf{F}_1(\varphi, n, p) \\ -\mathbf{F}_2(\varphi, n, p) \\ -\mathbf{F}_3(\varphi, n, p) \end{bmatrix} \quad (2.28)$$

where each matrix  $\mathbf{K}$  is a block of size  $N_{dof} \times N_{dof}$ . This implies that at every iteration step we have to solve a linear problem of  $3 \times N_{dof}$  variables. Moreover, to ensure convergence of the Newton iterative process, it is important to provide a very good initial guess vector  $[\varphi^0, n^0, p^0]$ . Because the problem variables have different orders of magnitude and the Jacobian matrix is often quite ill-conditioned, appropriate scaling and balancing techniques are needed in order to avoid problems associated with round-off error.

### 2.2.3 Gummel map algorithm

In 1964 H. K. Gummel proposed an original and alternative to (2.27) in order to solve system (2.10) in a semiconductor device in one spatial dimension [Gum64]. The main idea of the algorithm is to move the nonlinearity to the Poisson equation only, and once obtained the electric potential profile, both continuity equations are solved in linear form. This is possible if we consider the Maxwell-Boltzmann approximation for electrons (1.10) and holes (1.11) obtaining

$$F_1(\varphi) = \nabla \cdot (-\epsilon \nabla \varphi) - q(n_i(e^{(\varphi_p - \varphi)/V_{th}} - e^{(\varphi - \varphi_n)/V_{th}}) + D). \quad (2.29)$$

The Gummel algorithm is represented by the following iteration.

**Decoupled Gummel map.**

0. Give a suitable initial condition for  $\varphi^0$  and set a positive parameter  $toll_{GM} > 0$  (Gummel Map tolerance)
1. Fix a positive parameter  $toll_{NLP} > 0$  (Non Linear Poisson tolerance), solve the linearized Non Linear Poisson equation (NLP) in  $\Omega$  using the Newton method until  $\|F_1(\varphi^{k+1})\| > toll_{NLP}$ :

$$\begin{cases} \nabla \cdot (-\epsilon_{Si} \nabla \delta \varphi^k) + \frac{1}{V_{th}} \sigma_{Si}^k \delta \varphi^k = f_{Si}^k & \text{in } \Omega_{Si} \\ \nabla \cdot (-\epsilon_{ox} \nabla \delta \varphi^k) = f_{ox}^k & \text{in } \Omega_{ox} \\ \delta \varphi^k = 0 & \text{on } \Gamma_D \\ \nabla \delta \varphi^k \cdot \mathbf{n} = 0 & \text{on } \Gamma_N \\ \varphi^{k+1} = \varphi^k + \delta \varphi^k \end{cases} \quad (2.30)$$

having set:

$$\begin{aligned} \sigma_{Si}^k(\varphi^k) &= qn_i \left[ e^{(\varphi_p - \varphi^k)/V_{th}} - e^{(\varphi^k - \varphi_n)/V_{th}} \right] \\ f_{Si}^k(\varphi^k) &= \nabla \cdot (-\epsilon \nabla \varphi^k) + qn_i \left[ e^{(\varphi_p - \varphi^k)/V_{th}} - e^{(\varphi^k - \varphi_n)/V_{th}} + D \right] \\ f_{ox}^k(\varphi^k) &= \nabla \cdot (-\epsilon \nabla \varphi^k). \end{aligned}$$

2. Solve the Linear Electron Continuity Equation (LEC):

$$\begin{cases} \nabla \cdot (q\mu_n n \nabla \varphi^i - qD_n \nabla n) = -qR(n^{i-1}, p^{i-1}) & \text{in } \Omega_{Si} \\ n = n_D & \text{on } \Gamma_{D,Si} \\ \nabla n \cdot \mathbf{n} = 0 & \text{on } \Gamma_{N,Si} \end{cases} \quad (2.31)$$

3. Solve the Linear Hole Continuity Equation (LHC):

$$\begin{cases} \nabla \cdot (-q\mu_p p \nabla \varphi^i - qD_p \nabla p) = -qR(n^{i-1}, p^{i-1}) & \text{in } \Omega_{Si} \\ p = p_D & \text{on } \Gamma_{D,Si} \\ \nabla p \cdot \mathbf{n} = 0 & \text{on } \Gamma_{N,Si} \end{cases} \quad (2.32)$$

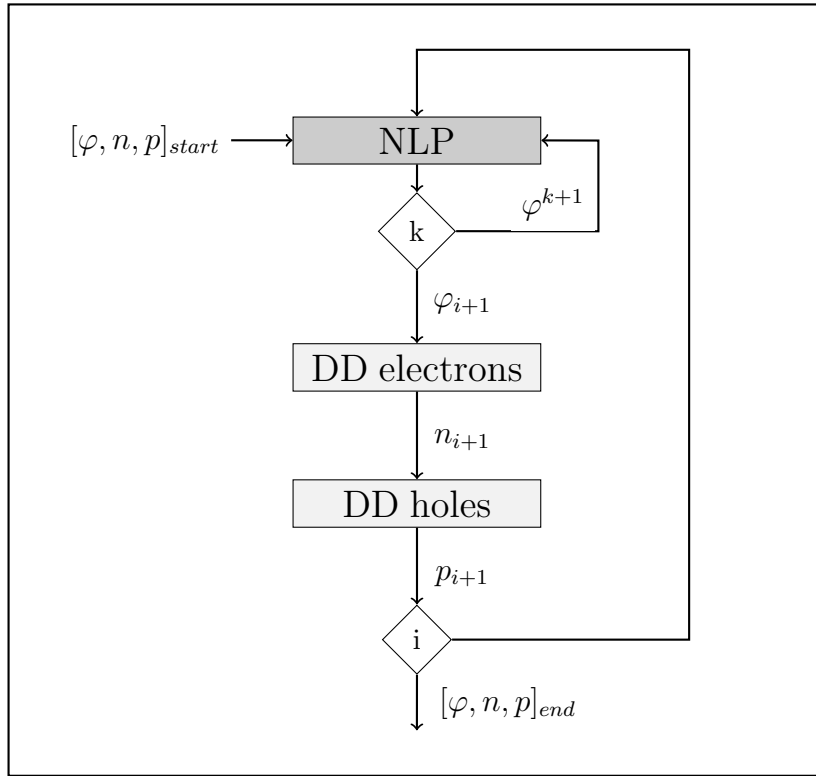
4. If  $\max\{\|\varphi^i - \varphi^{i-1}\|_{L^\infty}, \|p^i - p^{i-1}\|_{L^\infty}, \|n^i - n^{i-1}\|_{L^\infty}\} > toll_{GM}$  restart from step (1).



Fig.2.2 shows a flow chart of the Gummel algorithm where  $k$  is the iteration step of the inner loop, while  $i$  is the iteration step of the Gummel Map.

For the Gummel map, similar result as Thm.2.1 can be found in [Jer96], but the convergence rate is linear. However heuristic experience often shows superlinear convergence behaviour.

There are several advantages which make Gummel map algorithm better than the Fully Coupled Newton's Method, indeed simulations experience shows that the Gummel process is much more insensitive to the choice of the initial guess than Newton's method. This is particularly important in multidimensional problems where it is far from trivial to design a good starting point for initializing the iterative procedure. Another attractive feature is the reduced computational effort and memory cost: at each iteration step the Gummel algorithm requires the successive solution of three problems, each one of size equal to  $N_{dof} \times N_{dof}$ .



**Figure 2.2:** Flow chart of Gummel.

Let us discuss again on step 2-3 of *Decoupled Gummel map*. According with (1.54) the general R/G phenomenon can be separated in a reaction term

and a force term (except for the II which is only a force term contribution). Considering

$$\begin{aligned} R_n^{i-1}(n) &= \sigma_n^{i-1}n - f^{i-1} \\ R_p^{i-1}(p) &= \sigma_p^{i-1}p - f^{i-1} \end{aligned} \quad (2.33)$$

where

$$\begin{aligned} \sigma_n &= \frac{p^{i-1}}{F(p^{i-1}, n^{i-1})} & \sigma_p &= \frac{n^{i-1}}{F(p^{i-1}, n^{i-1})} \\ f &= \frac{n_i^2}{F(p^{i-1}, n^{i-1})} \end{aligned} \quad (2.34)$$

we can rewrite systems (2.31) and (2.32) as:

$$\begin{cases} \nabla \cdot (q\mu_n n \nabla \varphi^i - qD_n \nabla n) + q\sigma_n^{i-1}n = qf^{i-1} & \text{in } \Omega_{Si} \\ n = n_D & \text{on } \Gamma_{D, Si} \\ \nabla n \cdot \mathbf{n} = 0 & \text{on } \Gamma_{N, Si} \end{cases} \quad (2.35)$$

$$\begin{cases} \nabla \cdot (-q\mu_p p \nabla \varphi^i - qD_p \nabla p) + q\sigma_p^{i-1}p = qf^{i-1} & \text{in } \Omega_{Si} \\ p = p_D & \text{on } \Gamma_{D, Si} \\ \nabla p \cdot \mathbf{n} = 0 & \text{on } \Gamma_{N, Si} . \end{cases} \quad (2.36)$$

The above splitting of R/G term is called *lagging approach* [Jer96] and corresponds to extending to the non-linear case the classical *Jacobi* method for the iterative solution of linear algebraic systems. Since equations are sequentially solved, it is possible take advantage of the solution at the present step. Indeed an alternative approach would be use the solution of the first solved equation to compute the R/G contribution in the second equation. In such a case, the lagging method corresponds to extending to the nonlinear case the classical *Gauss-Seidel* method for the iterative solution in linear algebraic systems.

# Chapter 3

## Finite element discretization

In this chapter we present the weak formulation of problems (2.30), (2.35) and (2.36). For each weak problem we discuss the well-posedness analysis and describe the finite element discretization.

### 3.1 Non Linear Poisson Equation: weak form

Let us write problem (2.30) in compact form:

$$\left\{ \begin{array}{ll} \nabla \cdot (-\epsilon \nabla \delta \varphi^k) + \sigma^k \delta \varphi^k &= f^k & \text{in } \Omega \\ \delta \varphi^k &= 0 & \text{on } \Gamma_D \\ \nabla \delta \varphi^k \cdot \mathbf{n} &= 0 & \text{on } \Gamma_N \\ \varphi^{k+1} &= \varphi^k + \delta \varphi^k & \end{array} \right. \quad (3.1)$$

having set:

$$\begin{aligned} \epsilon &= \epsilon_s \mathcal{I}_{\Omega_{Si}} + \epsilon_{ox} \mathcal{I}_{\Omega_{ox}} \\ f &= f_s \mathcal{I}_{\Omega_{Si}} + f_{ox} \mathcal{I}_{\Omega_{ox}} \\ \sigma &= \sigma_s \mathcal{I}_{\Omega_{Si}} \end{aligned}$$

where  $\mathcal{I}_A(\mathbf{x})$  is equal to 1 if  $\mathbf{x} \in A$  and 0 otherwise. System (3.1) is a Diffusion-Reaction (DR) problem in  $\Omega$ , with respect to the dependent variable  $\delta \varphi^k$ . Now we multiply the first equation in (3.1) by a test function  $v \in H_{\Gamma_D}^1(\Omega)$  and integrating over all the domain we obtain

$$-\int_{\Omega} \nabla \cdot (-\epsilon \nabla \delta \varphi^k) v \, d\Omega + \int_{\Omega} \sigma^k \delta \varphi^k v \, d\Omega = \int_{\Omega} f^k v \, d\Omega \quad \forall v \in H_{\Gamma_D}^1(\Omega). \quad (3.2)$$

Applying the Green formula and considering the boundary conditions, we obtain the weak formulation of (3.1) which reads: find  $\delta\varphi^k \in H_{\Gamma_D}^1(\Omega)$  such that

$$\int_{\Omega} \epsilon \nabla \delta\varphi^k \nabla v \, d\Omega + \int_{\Omega} \sigma^k \delta\varphi^k v \, d\Omega = \int_{\Omega} f^k v \, d\Omega \quad \forall v \in H_{\Gamma_D}^1(\Omega). \quad (3.3)$$

We are able to define the following bilinear form

$$a : H_{\Gamma_D}^1(\Omega) \times H_{\Gamma_D}^1(\Omega) \rightarrow \mathbb{R}, \quad a(u, v) = \int_{\Omega} \epsilon \nabla u \nabla v \, d\Omega + \int_{\Omega} \sigma^k uv \, d\Omega. \quad (3.4)$$

and the linear and bounded functional

$$F : H_{\Gamma_D}^1(\Omega) \rightarrow \mathbb{R}, \quad F(v) = \int_{\Omega} f^k v \, d\Omega \quad (3.5)$$

In order to prove the existence and uniqueness of the solution of (3.3), we apply the *Lax-Milgram theorem* [Sal10]. Well-posedness is ensured by several physical hypotheses:

- $\epsilon \in L^\infty(\Omega)$  and  $\epsilon(\mathbf{x}) > 0$  a.e. in  $\Omega$ ;
- $\forall k \geq 0$   $\sigma^k \in L^\infty(\Omega)$  and  $\sigma^k(\mathbf{x}) > 0$  a.e. in  $\Omega_{Si}$ .

We define some useful quantities:

$$\begin{aligned} \epsilon_M &= \max_{\Omega} \epsilon & \epsilon_m &= \min_{\Omega} \epsilon \\ \sigma_M &= \max_{\Omega} \sigma & \sigma_m &= \min_{\Omega} \sigma = 0 \end{aligned}$$

Take into account the above hypotheses it's possible to demonstrate:

- **Continuity of the bilinear form:**

$$\forall u, v \in H_{\Gamma_D}^1$$

$$\begin{aligned} \left| \int_{\Omega} \epsilon \nabla u \nabla v + \int_{\Omega} \sigma^k uv \right| &\leq \epsilon_M \|\nabla u\|_{L^2} \|\nabla v\|_{L^2} + \sigma_M \|u\|_{L^2} \|v\|_{L^2} \\ &\leq \max\{\epsilon_M, \sigma_M\} (\|\nabla u\|_{L^2} \|\nabla v\|_{L^2} + \|u\|_{L^2} \|v\|_{L^2}) \\ &\leq \max\{\epsilon_M, \sigma_M\} \|u\|_{H_{\Gamma_D}^1} \|v\|_{H_{\Gamma_D}^1}. \end{aligned}$$

- **Coercivity of the bilinear form:**

$$\forall u \in H_{\Gamma_D}^1$$

$$\begin{aligned} \left| \int_{\Omega} \epsilon \nabla u \nabla u + \int_{\Omega} \sigma^k u^2 \right| &\geq \epsilon_m \|\nabla u\|_{L^2}^2 + \sigma_m \|u\|_{L^2}^2 \\ &= \epsilon_m \|\nabla u\|_{L^2}^2 \\ &= \epsilon_m \|\nabla u\|_{H_{\Gamma_D}^1}^2 \equiv \epsilon_m \|u\|_{H_{\Gamma_D}^1}^2. \end{aligned}$$

- **Continuity of the functional:**

$$|\int_{\Omega} f^k v| \leq \|f^k\|_{L^2} \|v\|_{H_{\Gamma_D}^1} \quad \forall v \in H_{\Gamma_D}^1.$$

Then we can state that  $\forall k \geq 0$  there exists a unique weak solution of the linearized Non Linear Poisson equation.

### 3.2 Continuity Equations: weak form

Without loss of generality we consider only the electron continuity equation. System (2.35) is a diffusion-advection-reaction (DAR) problem in conservative form. With a suitable change of variables we are able to treat these PDE likewise the linearized Non Linear Poisson equation in the previous section. Consider the Slotboom variable (1.38), we can rewrite system (2.35) as:

$$\begin{cases} \nabla \cdot (-q D_n e^{\varphi^i/V_{th}} \nabla u_n) + \sigma_n^{i-1} e^{\varphi^i/V_{th}} u_n = f^{i-1} & \text{in } \Omega_{Si} \\ u_n = n_D e^{-\varphi^i/V_{th}} & \text{on } \Gamma_{D,Si} \\ \nabla u_n \cdot \mathbf{n} = 0 & \text{on } \Gamma_{N,Si}. \end{cases} \quad (3.6)$$

Proceeding as in Section 3.1, the weak formulation of the Electron Continuity equation is:

find  $u_n \in H_{\Gamma_{D,Si}}^1(\Omega)$  such that

$$\int_{\Omega_{Si}} q D_n e^{\varphi^i/V_{th}} \nabla u_n \nabla v \, d\Omega + \int_{\Omega_{Si}} \sigma_n^{i-1} e^{\varphi^i/V_{th}} u_n v \, d\Omega = \int_{\Omega_{Si}} f^{i-1} v \, d\Omega \quad \forall v \in H_{\Gamma_{D,Si}}^1. \quad (3.7)$$

Existence and uniqueness of the unknown variable  $u_n$  ensures the same properties on  $n$ , thanks to the relation (1.38) between  $u_n$  and  $n$ . Further hypotheses on the coefficients  $\forall i \geq 0$ :

- $q D_n e^{\varphi^i/V_{th}} \in L^\infty(\Omega_{Si})$  and  $D_n(\mathbf{x}) > 0$  a.e. in  $\Omega_{Si}$ ;
- $\sigma_n^{i-1} e^{\varphi^i/V_{th}} \in L^\infty(\Omega_{Si})$  and  $\sigma_n^{i-1}(\mathbf{x}) > 0$  a.e. in  $\Omega_{Si}$ .

We define the bilinear form

$$a(u, v) = \int_{\Omega_{Si}} q D_n e^{\varphi^i/V_{th}} \nabla u_n \nabla v \, d\Omega + \int_{\Omega_{Si}} \sigma_n^{i-1} e^{\varphi^i/V_{th}} u_n v \, d\Omega \quad (3.8)$$

and the linear and bounded functional

$$F(v) = \int_{\Omega_{Si}} f^{i-1} v \, d\Omega \quad (3.9)$$

Well-posedness of problem (3.7) is verified using the same arguments as in Section 3.1.

### 3.3 Numerical approximation

In this section we introduce the Galerkin method to approximate the weak formulations (3.3) and (3.7) (see [QV08]). Each of them can be represented in compact form as:

find  $u \in V$  such that

$$a(u, v) = F(v) \quad \forall v \in V \quad (3.10)$$

where  $V$  is the space of admissible functions, e.g.  $H_{\Gamma_D}^1(\Omega)$  or  $H_{\Gamma_D, Si}^1(\Omega_{Si})$ . Let us introduce  $V_h$  which is a family of finite-dimensional subspaces of  $V$ , depending on a positive parameter  $h$ , such that

$$V_h \subset V, \quad \dim V_h < \infty \quad \forall h > 0 \quad (3.11)$$

The *Galerkin problem* reads:

find  $u_h \in V_h$  such that

$$a(u_h, v_h) = F(v_h) \quad \forall v_h \in V_h. \quad (3.12)$$

Unique solvability of (3.12) is an immediate consequence of the analysis carried out in Sections 3.1 and 3.2.

Let  $\mathcal{T}_h$  be a partition of  $\Omega$ , and  $K$  a generic element of  $\mathcal{T}_h$  such that  $\bar{\Omega} = \bigcup \bar{K}$ . In this case the parameter  $h$  represents the characteristic dimension of each element  $K$ . For  $n \geq 1$  let us introduce the general finite element spaces of the polynomial element wise functions

$$X_h^r(\Omega) := \{v_h \in C^0(\bar{\Omega}) : v_h|_K \in \mathbb{P}_r(K), \forall K \in \mathcal{T}_h\} \quad (3.13)$$

and the associated space where functions vanish on boundaries

$$X_{h, \Gamma_D}^r(\Omega) := \{v_h \in X_h^r : v_h|_{\Gamma_D} = 0\}. \quad (3.14)$$

If  $\Omega \subset \mathbb{R}^3$  we have

$$\dim \mathbb{P}_r(K) := \binom{3+r}{r} \quad (3.15)$$

We approximate  $H_{\Gamma_D}^1(\Omega)$  with  $X_{h,\Gamma_D}^1(\Omega)$  and  $H_{\Gamma_{D,Si}}^1(\Omega_{Si})$  with  $X_{h,\Gamma_{D,Si}}^1(\Omega_{Si})$ . Therefore according to (3.15) we have:

$$\begin{aligned}\dim \mathbb{P}_1(K) &= 4 \\ \dim X_h^1 &= N_h \\ \dim X_{h,\Gamma_D}^1 &= N_h - N_g\end{aligned}$$

where  $N_h$  is the number of vertices of the partition  $\mathcal{T}_h$  and  $N_g$  is the number of vertices that belong to the Dirichlet boundary.

We denote by  $\{\psi_j\}_{j=1}^{N_h}$  the Lagrangian basis of the space  $X_h^1$  in such a way that

$$u_h(\mathbf{x}) = \sum_{j=1}^{N_h} u_j \psi_j(\mathbf{x}). \quad (3.16)$$

Since each function of  $V_h$  is a linear combination of  $\psi_i$  for  $i = 1, \dots, N_h$ , the Galerkin problem (3.12) becomes:

find  $[u_1, u_2, \dots, u_{N_h}]^T \in \mathbb{R}^{N_h}$  such that

$$\sum_{j=1}^{N_h} u_j a(\psi_j, \psi_i) = F(\psi_i) \quad \forall i = 1, \dots, N_h. \quad (3.17)$$

In order to implement problem (3.17) it's convenient to express the bilinear form  $a(\cdot, \cdot)$  and the linear functional  $F(\cdot)$  with respect to each element of the partition  $\mathcal{T}_h$  as

$$\sum_{j=1}^{N_h} u_j \sum_{K \in \mathcal{T}_h} a_K(\psi_j, \psi_i) = \sum_{K \in \mathcal{T}_h} F_K(\psi_i) \quad \forall i = 1, \dots, N_h. \quad (3.18)$$

### 3.3.1 Geometrical discretization

Each element  $K \in \mathcal{T}_h$  is a tetrahedron of volume  $|K|$ . From now on, we assume that there exists a constant  $\delta > 0$  such that

$$\frac{h_K}{\rho_K} \leq \delta \quad \forall K \in \mathcal{T}_h \quad (3.19)$$

where  $h_K = \text{diam}(K) = \max_{x,y \in K} |x - y|$  and  $\rho_K$  is the diameter of the sphere inscribed in the tetrahedral  $K$ . Condition (3.19) is the so called *mesh regularity condition* [Qua08] [QV08]. We denote with  $\mathcal{E}_h$ ,  $\mathcal{V}_h$  and  $\mathcal{F}_h$  the set

of all the edges, vertices and faces of  $\mathcal{T}_h$  respectively, and for each  $K \in \mathcal{T}_h$  we denote by  $\partial K$  and  $\mathbf{n}_{\partial K}$  the boundary of the element and its outward unit normal.

We notice that  $\mathcal{T}_h$  is built in such a way that every  $K$  belongs to a single region, while it is possible that vertices belong to different regions.

### 3.3.2 Linearized Non Linear Poisson equation

Concerning with the linearized NLP equation we have

$$a(\psi_j, \psi_i) = \int_{\Omega} \epsilon \nabla \psi_j \nabla \psi_i d\Omega + \int_{\Omega} \sigma^k \psi_j \psi_i d\Omega \quad (3.20)$$

and the restriction on each element  $K$  is

$$a_K(\psi_j, \psi_i) = \int_K \epsilon \nabla \psi_j \nabla \psi_i dK + \int_K \sigma^k \psi_j \psi_i dK. \quad (3.21)$$

Equation (3.21) contains two distinct contributions: the first one identifies the diffusive contribution and generates the so-called *stiffness matrix*, while the second refers to the reaction term and generates the *mass matrix*.

The coefficient  $\epsilon$  is a piece wise constant function, which changes on different material regions. Therefore  $\epsilon$  is constant over each element and the first integral in (3.21) become easier to compute.

As a consequence of choosing the discrete space  $X_h^1$ , we can not expect a better convergence rate than the first order in  $\|\cdot\|_{1,\Omega}$  with respect to  $h$  [QV08]. This implies that is not necessary to make use of an high-order quadrature rule, so that the trapezoidal rule is enough accurate. The main consequence of the using trapezoidal quadrature rule is that the mass-matrix becomes diagonal. This technique is well known as *lumping procedure* applied on the mass-matrix.

The contributions of the local system matrix  $A_K^k$  is

$$[A_K^k]_{ij} = \epsilon_K L_{ij} + \frac{|K|}{4} \sigma_i^k \quad (3.22)$$

having set

$$\begin{aligned} L_{ij} &= \int_K \nabla \psi_i \nabla \psi_j d\Omega \\ \sigma_i^k &= \sigma^k(\mathbf{x}_i). \end{aligned} \quad (3.23)$$

The construction of the right hand side of (3.18) using the trapezoidal rule yields:



$$[F_K]_i^k = f_i^k \frac{|K|}{4} \simeq \int_{\Omega} f^k \psi_i d\Omega. \quad (3.24)$$

The local contributions of each element  $K$  are assembled in the global matrix  $A$  as follows. Let  $I$  be the global index of a generic vertex belonging to the partition  $\mathcal{T}_h$ . We denote by  $\mathcal{J}_K : \mathcal{V}_{\mathcal{T}_h} \rightarrow \mathcal{V}_K$  the map which connects  $I$  to its corresponding local index  $i = 1, \dots, 4$  in the element  $K$ . Then we have

$$A_{IJ}^k = \sum_{\substack{\forall K \in \mathcal{T}_h \text{ s.t.} \\ \mathcal{J}_K(I), \mathcal{J}_K(J) \subset \mathcal{V}_K}} [A_K]_{ij}^k. \quad (3.25)$$

Analogously for the force term  $\mathbf{b}^k$

$$b_I^k = \sum_{\substack{\forall K \in \mathcal{T}_h \text{ s.t.} \\ \mathcal{J}_K(I) \subset \mathcal{V}_K}} [F_K]_i^k. \quad (3.26)$$

Once we have built the global matrix  $A^k$  and the global vector  $\mathbf{b}^k$  we need to take into account the essential boundary conditions. In fact the displacement formulation is a primal method which enforces Dirichlet boundary condition in a strong manner. Therefore we have to modify the algebraic system. We choose the *diagonalization* technique which does not alter the matrix pattern nor introduce ill-conditioning in the linear system. Let  $i_D$  be the generic index of a Dirichlet node, we denote by  $[\delta\varphi_D]_i$  (which in this case is equal to zero) the known value of the solution  $\delta\varphi$  at the node. We consider the Dirichlet condition as an equation of the form  $\beta[\delta\varphi]_i = \beta[\delta\varphi_D]_i$ , where  $\beta \neq 0$  is a suitable coefficient. In order to avoid degradation of the global matrix condition number, we take  $\beta$  equal to the diagonal element of the matrix at row  $i_D$ .

Finally, the discretization of step 1 in the Gummel algorithm, reads:

$$\begin{cases} A^k \delta\varphi^k &= \mathbf{b}^k \\ \varphi^{k+1} &= \varphi^k + \delta\varphi^k. \end{cases} \quad (3.27)$$

As every iteration procedure, problem (3.27) needs a suitable convergence break criterion. A good approach is based on checking the satisfaction of the fixed point equation (2.11) by the  $k$ -th solution. In this case the inner loop of the Gummel Map reads as: given a tolerance  $toll > 0$  solve problem (3.27) until

$$\|\mathbf{b}(\varphi^{k+1})\|_2 > toll \quad (3.28)$$

where  $\|\cdot\|_2$  is the usual Euclidean norm for a vector.

### Damping

Despite the validity of Thm.2.1, the use of the Newton's method may be affected by numerical difficulties. The main problem is the tendency of the method to overestimate the length of the correction step. This phenomenon is frequently indicated as *overshoot*. In the case of the semiconductor equations this overshoot problem can be treated by simply limiting the size of the correction vector ( $\delta\varphi$ ) determined by Newton's method. The usual established modifications to avoid overshoot are given by the following formulation:

$$\tilde{A}(\varphi_k) = \frac{1}{t_k} A(\varphi_k) \quad (3.29)$$

where  $t_k$  is a positive parameter to be properly chosen, with  $t_k = 1$  the modified Newton method reduces to the classical Newton method. For the case (3.29) a simple criterion suggested by Deuffhard [Deu74], prescribes that  $t_k$  is taken in  $(0, 1]$  in such a way that for any norm, we have

$$\|A(\varphi_k)^{-1} \mathbf{b}(\varphi_k - t_k A(\varphi_k)^{-1} \mathbf{b}(\varphi_k))\| < \|A(\varphi_k)^{-1} \mathbf{b}(\varphi_k)\|. \quad (3.30)$$

Satisfying condition (3.30) guarantees that the norm of the residual is decreasing with  $k$ . This condition is hardly to be evaluated because the presence of the inverse of  $A$ . If the solution is accomplished using a direct method like the  $LU$  factorization, the evaluation of the argument of the norm on the left hand side of (3.30) is reduced to a forward and backward substitution and the evaluation of  $\mathbf{b}(\varphi)$ . However we use an iterative method (BCG solver based on [PTVF07]) and this implies serious difficulties to the application of the criterion (3.30). In order to overcome this problem we consider another valid possibility, replacing  $A$  in (3.30) with the main diagonal  $D(\varphi_k)$ :

$$\|D(\varphi_k)^{-1} \mathbf{b}(\varphi_k - t_k D(\varphi_k)^{-1} \mathbf{b}(\varphi_k))\| < \|D(\varphi_k)^{-1} \mathbf{b}(\varphi_k)\|. \quad (3.31)$$

This criterion has been adopted in our code. However the value to use for  $t_k$  is a question of trial and error. Frequently the following sequences are used:

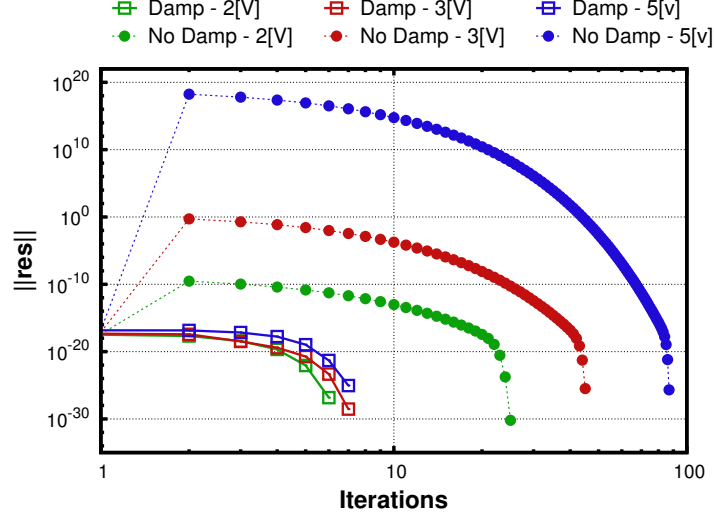
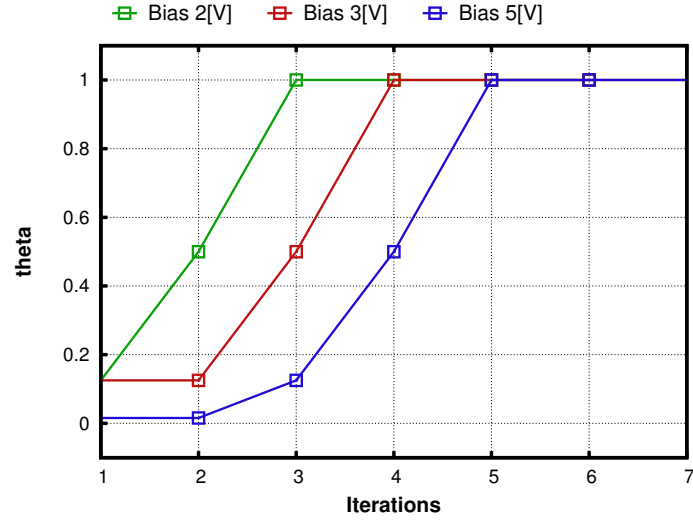
$$t_k = \frac{1}{2^i} \quad (3.32)$$

$$t_k = \frac{1}{\frac{i(i+1)}{2} \cdot 2} \quad (3.33)$$

where  $i$  is the number of subiterations of the damping procedure needed to satisfy (3.31). Close to the solution, (3.30) (and so (3.31)) will be satisfied with  $t_k = 1$  so that the quadratic convergence properties of the classical Newton method are recovered.

The benefits due to the damping technique are visible in Fig.3.1a, where for different voltages applied to a p-n junction, the evolution of the residual, for the first Gummel map iteration, is shown. When damping is switched-off first iterations are critical, because the solution found is very far from the real one. When damping is switched-on this problem is solved and the scheme converges with fewer iterations. In some heuristic sense this procedure guarantees a progressive approaching of the solution to the ball mentioned in Thm.2.1, where the convergence rate is quadratical. In Fig.3.1b the evolution of the coefficient  $t_k$  is depicted. The curves are monotonic from 0 to 1 below and this means that damping procedure is more relevant in the first iterations than in the last, where the standard Newton method is recovered.

Finally, we notice that for high voltages the scheme needs more iterations to converge. This phenomena is strictly related to the shape of the initial guess and we see it in detailed in Section 4.1.1.

(a) *Non Linear Poisson residual: damping benefit prodedure.*(b)  $t_k$  parameter.

**Figure 3.1:** (a) Number of iteration against residual for different voltages in a diode test case. (b) Magnitude of the damping parameter  $t_k$ .

### 3.3.3 Continuity equations

Concerning with equation (3.6) we can write the bilinear form as

$$a(u, v) = \int_{\Omega_{Si}} q D_n e^{\varphi^i/V_{th}} \nabla \psi_j \nabla \psi_i d\Omega + \int_{\Omega_{Si}} \sigma_n^{i-1} e^{\varphi^i/V_{th}} \psi_j \psi_i d\Omega. \quad (3.34)$$

Even if this form allows an immediate analysis of well-posedness, the choice of using Slotboom variables  $u_n$  and  $u_p$  causes the onset of overflow problems due to the evaluation of  $\exp(\varphi/V_{th})$ , which can be a rapidly varying function according to the behaviour of the potential  $\varphi$ .

Therefore special care has to be taken in the treatment of the diffusion coefficient. In view of further discussion we introduce some useful notation. For each set  $S \subset \Omega$  having measure  $|S|$ , we introduce the following averages of a given function  $g$  that is integrable on  $S$ :

$$\mathcal{M}_S(g) = \frac{\int_S g dS}{|S|}, \quad \mathcal{H}_S = (\mathcal{M}_S(g^{-1}))^{-1}.$$

Notice that  $\mathcal{M}_S$  is the usual integral average, while  $\mathcal{H}_S$  is the *harmonic average*. It is well-known that the use of the harmonic average provides a superior approximation performance in one spatial dimension [IE83].

The weak form (3.34) is the result of a standard displacement approach, although different variational formulations and therefore different finite element approximations may be used, like a primal mixed approach (PM). First of all it is convenient to reformulate problem (2.35) by using relations (1.38) and (1.40) in a more generical form as:

$$\begin{cases} \nabla \cdot \mathbf{J}_n(n) + \sigma n = f & \text{in } \Omega_{Si} \\ \mathbf{J}_n = q D_n e^{\varphi/V_{th}} \nabla (e^{-\varphi/V_{th}} n) & \text{in } \Omega_{Si} \\ n = n_D & \text{on } \Gamma_{D,Si} \\ \mathbf{J}_n \cdot \mathbf{n} = 0 & \text{on } \Gamma_{N,Si}. \end{cases} \quad (3.35)$$

Problem (3.35) can be discretized considering the *Edge Averaged Finite Elements* (EAFE). The complete derivation of this scheme can be found in [XZ99] [ZL12].

The EAFE scheme is particularly suited for problems with a highly variable diffusion coefficient. Furthermore this approach has several good properties, i.e. in 2D simulation if  $\mathcal{T}_h$  is a Delaunay partition the system matrix is an M-matrix [BCC98]. The main consequence of this statement is that the solution satisfying the *Discrete Maximum Principle*. This is a notable

property which implies that no negative concentrations are admitted. Unfortunately this property is not anymore valid in 3D framework, because the Delaunay condition on the mesh is not sufficient to guarantee that the system matrix is an M-matrix. A more general condition is presented in [XZ99].

**Theorem 3.1** (Zikatanov condition). *The system matrix of the EAFE scheme is an M-matrix if and only if for any fixed edge  $E$  of the partition  $\mathcal{T}_h$  the following inequality holds*

$$\omega_E = \frac{1}{d(d-1)} \sum_{K \supset E} |k_E^K| \cot \theta_E^K \geq 0, \quad (3.36)$$

where  $\sum_{K \supset E}$  means summation over all simplexes  $K$  containing  $E$ ,  $\theta_E^K$  is the angle between the faces  $f_i, f_j \in \mathcal{T}_h$  such that  $f_i \cap f_j = E$  and  $k_E^K$  is the edge in  $K$  which does not share any vertices with  $E$ .

*Observation 3.1.* For  $d = 2$ , condition (3.36) means that the sum of the angles opposite to any edge is less than or equal to  $\pi$ , which implies that the partition is a Delaunay triangulation.

*Observation 3.2.* Condition (3.36) highlights that in order to satisfy the discrete maximum principle, a partition without obtuse angles is preferable.

We remark that presently meshing algorithm are oriented to care about the minimum angle of the elements, rather than the maximum, this implying that to obtain a mesh which satisfies condition (3.36) is a really difficult task.

Fig.3.2 shows a simple partition of a cube performed with the Synopsis tool SNMESH. For every element we evaluated how many edges do not satisfy condition (3.36). It is clear that there are a lot of edges which do not fulfil the condition and a precise pattern cannot be signed out. When several bad edges belong to a single element we can identify the presence of many obtuse angles.

In order to avoid this problem some alternative solutions are proposed in the literature, like the *Orthogonal Subdomain Collocation method* [PC98], but also this approach is not a definite solution.

Therefore in presence of a negative concentration the most used technique in 3D numerical simulation is to local mesh refinement in the regions where trouble occurs, which often are the ones where the carrier density decreases.

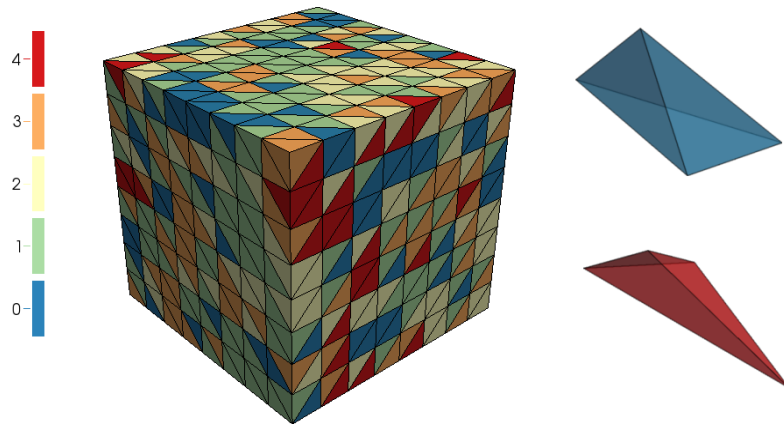


**Figure 3.2:** Evaluation of the Zikatanov condition over a simple partition. Red elements do not satisfy condition (3.36) over four edges while blue elements fully satisfy the criterion.





# Chapter 4

## Simulation results

In this chapter we present the work done in order to validate the numerical implementation of the discretization method illustrated in Chapter 3, in the FEMOS 3D code compared with a reference simulation tool (SDE-VICE, commercialized by Synopsys [Sde13]). In particular we illustrate (and compare) the algorithm used to calculate the current at the ohmic contacts.

### 4.1 Test cases

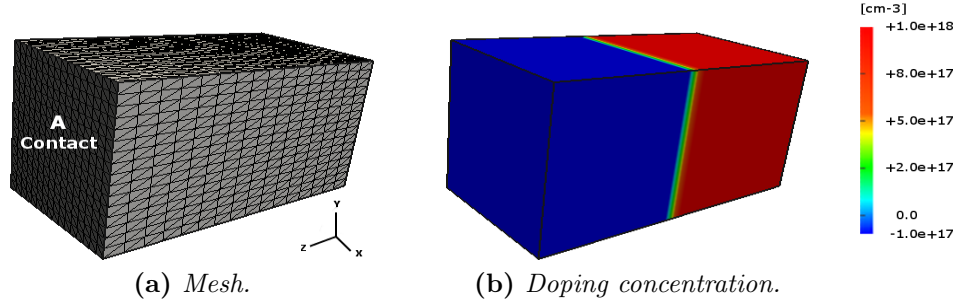
We consider three kinds of semiconductor devices:

- **p-n junction**
- **p-n junction in oxide**
- **n-channel / p-channel MOSFET**

#### 4.1.1 p-n junction

In this example we consider a simple p-n junction. Fig.4.1 presents the partition and the doping profile for this test. The section of the parallelepiped is a  $0.05 \times 0.05[\mu m^2]$  square while the device is  $0.1[\mu m]$  long. The number of vertices are 4933, while the elements are 24576. The doping concentration is obtained setting a constant profile of acceptors over all the domain ( $N_A^- = 1.0 \times 10^{17}[cm^{-3}]$ ) overwhelmed by a doping profile of donors ( $N_D^+ = 1.0 \times 10^{18}[cm^{-3}]$ ) bounded on one side of the device and resulting in an almost abrupt junction. Two contacts are defined: (A) contact is placed at  $Z = 0.1[\mu m]$  and (B) contact is placed at  $Z = 0.0[\mu m]$ .

In order to analyze the operating function of the diode, two cases of direct bias are performed:  $0.3[V]$ - $1.0[V]$ . The setting values and the parameters

**Figure 4.1:** p-n junction.

are summarized in Tab.4.1. Fig.4.2 reports the solutions for  $V_A = 0.3[V]$  and  $V_A = 1.0[V]$ , along a line parallel to the Z-axis and placed at the center of the device. Because the built-in voltage is around  $0.7 \div 0.8[V]$  the behaviour of the device is different when the applied bias is below or above this threshold. At a bias voltage of  $0.3[V]$ , potential drop is almost bounded around the junction, and due to the asymmetric doping, is mostly extended in the p-side. Carriers cannot cross the potential barrier and this causes a low current flux inside the device. At  $1.0[V]$  the minority carrier density becomes almost ten order bigger, resulting in a large amount of current toward the contacts: the device turns from exponential to linear resistive. This is clear in Fig.4.2b where the potential shape becomes similar to a that of a resistance voltage profile (linear potential profile). Comparing the quasi Fermi potentials of Fig.4.2e and Fig.4.2f the boundary layers at contacts increase with the applied bias. This effect is related to the ohmic contact hypothesis, and can be avoided by adopting different boundary condition: this occurs also for the carrier concentration because at the contacts, charge neutrality and thermodynamic equilibrium are imposed.

Figs.4.3÷4.5 shows the comparison between SDEVICE and FEMOS in 3D plots for electrostatic potential, electron and hole densities at  $0.3[V]$ , while Figs.4.6÷4.8 show the same comparison at  $1.0[V]$ . In both conditions the agreement is very good.

Test case [V]	Mobility model [ $cm^2V^{-1}s^{-1}$ ]	R/G model	$\epsilon_{Si}$
$V_A = 0.3$	$\mu_n = 1417, \mu_p = 470.5$	SRH, Auger	11.6
$V_A = 1.0$	$\mu_n = 1417, \mu_p = 470.5$	SRH, Auger	11.6

**Table 4.1:** p-n junction - list of settings, parameters and models.

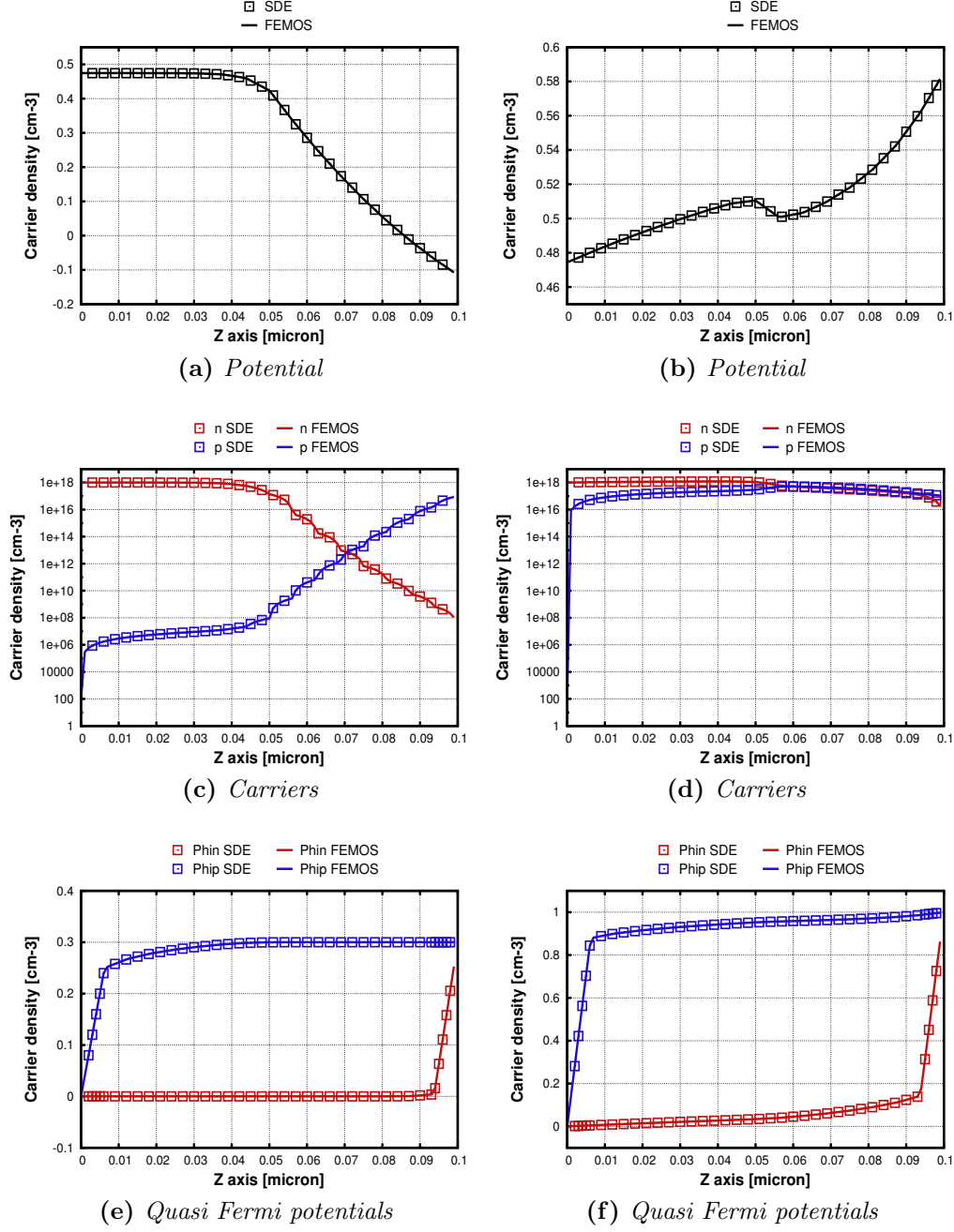


**Figure 4.2:** 1D plots of the solutions and the quasi fermi potential levels along the line parallel to the Z-axis and placed at the center of the device. On the left is presented the test case at  $V_A = 0.3[V]$  while on the right at  $V_A = 1.0[V]$ .

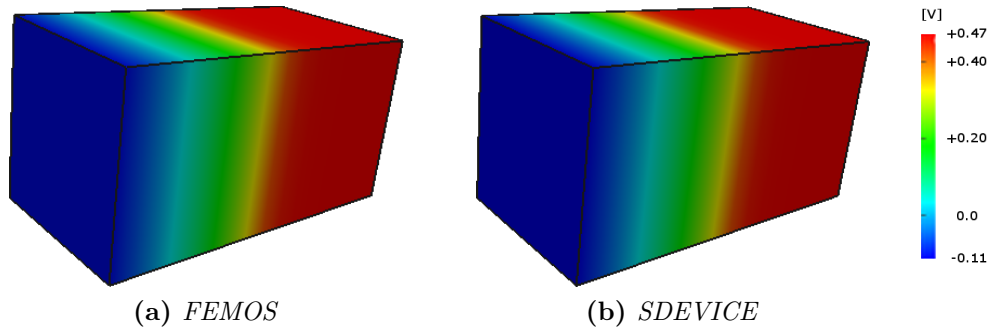


**Figure 4.3:** p-n junction 0.3[V] - Electrostatic Potential.

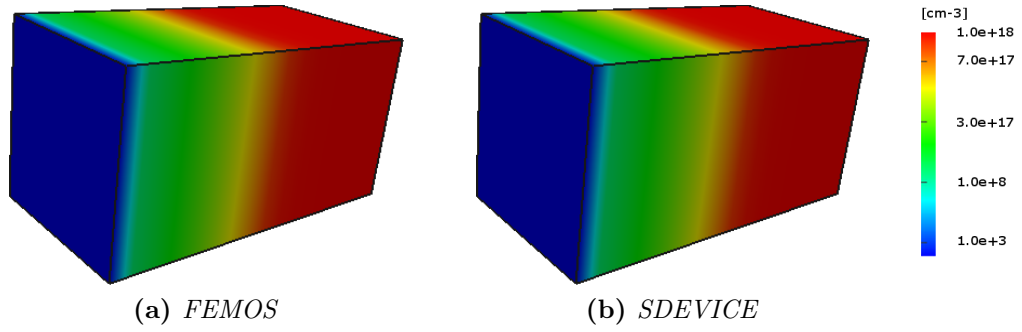


**Figure 4.4:** p-n junction 0.3[V] - Electron density.

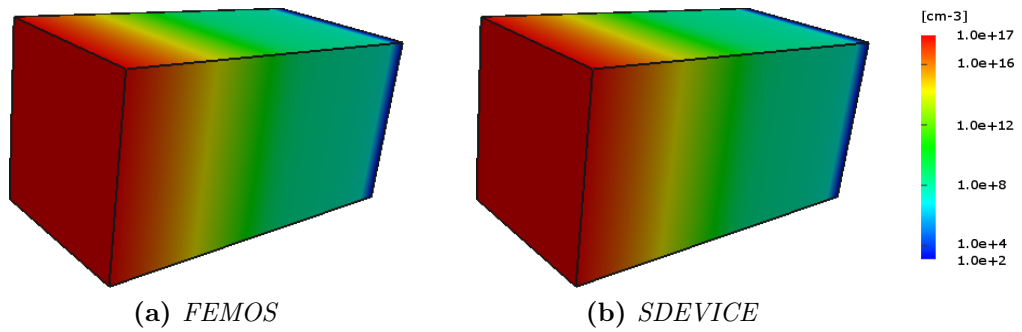


**Figure 4.5:** p-n junction 0.3[V] - Hole density.

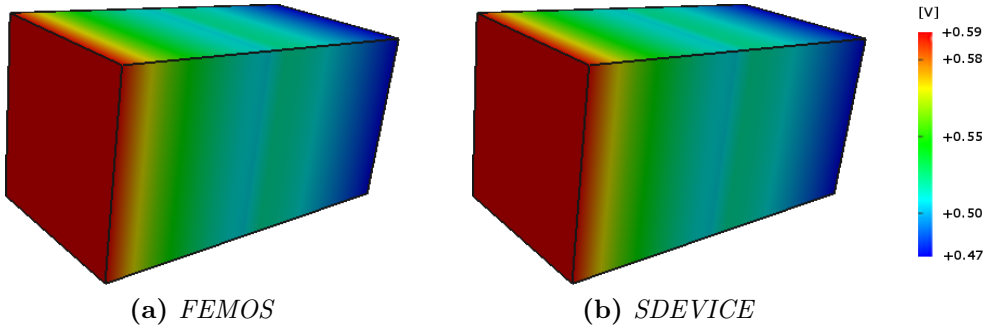


**Figure 4.6:** p-n junction 1.0[V] - Electrostatic Potential.

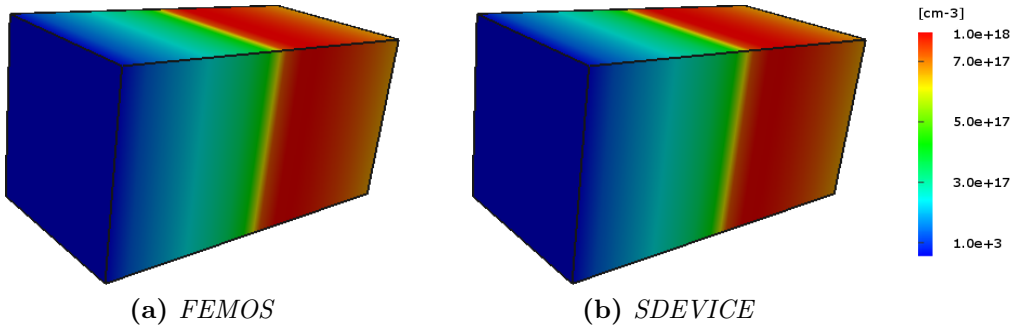


**Figure 4.7:** p-n junction 1.0[V] - Electron density.

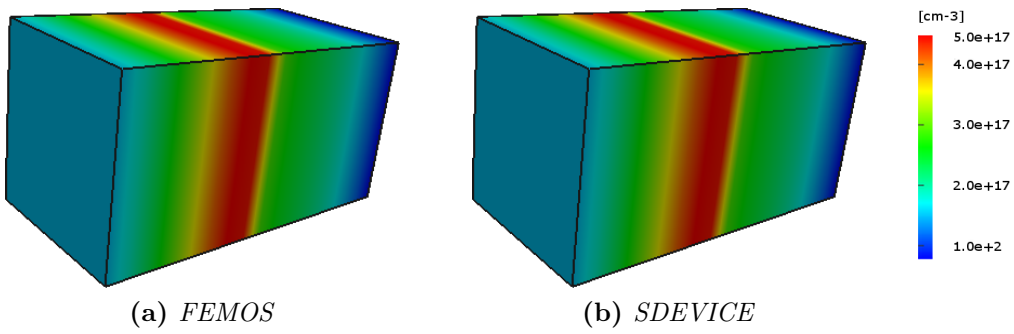


**Figure 4.8:** p-n junction 1.0[V] - Hole density.

### Computational cost and initial condition

Computational experience demonstrates that convergence of the Gummel algorithm is strictly related to the kind of chosen initial condition: the closest to solution, the better the convergence. However, to predict in every situation the possible shape of the solutions is hard (if not even impossible). For this reason we have adopted a common and general approach splitting the domain in several regions according to their doping concentration: each of the semiconductor regions are treated as they are in equilibrium with the nearest contact, then the initial guess for  $\varphi$  is obtained using the relations (1.22) or (1.23). This choice corresponds to a case close to equilibrium and guarantees good performance of the algorithm.

In order to analyze the response of the system at different bias an additional test is realized: in the range between 0.0[V] and 3.0[V] several voltages are applied on the previous device and for each bias point the initial guess is computed as described.

Fig.4.9 shows how the computational cost increases as the applied bias is increased. Moreover as expected if the mesh is finer, the time needed to find the solution increases, resulting in a rigid upper shift of the curve.

Let us consider the case with a coarse mesh. In Fig.4.10 it is clear how the average time spent to solve the NLP and the DD equations remains almost unchanged. On the contrary the number of GM iterations needed by the system to reach the solution, increases for voltages above  $\approx 1.5[V]$ .

A possible explanation of this trend can be found comparing solution

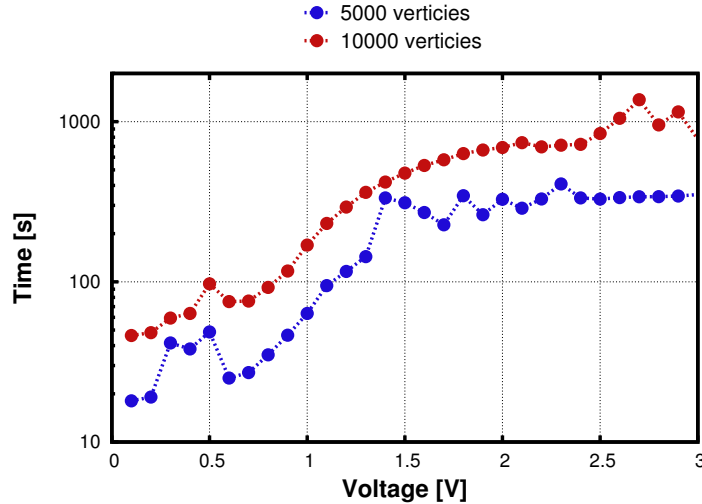


**Figure 4.9:** Total time Gummel Map.

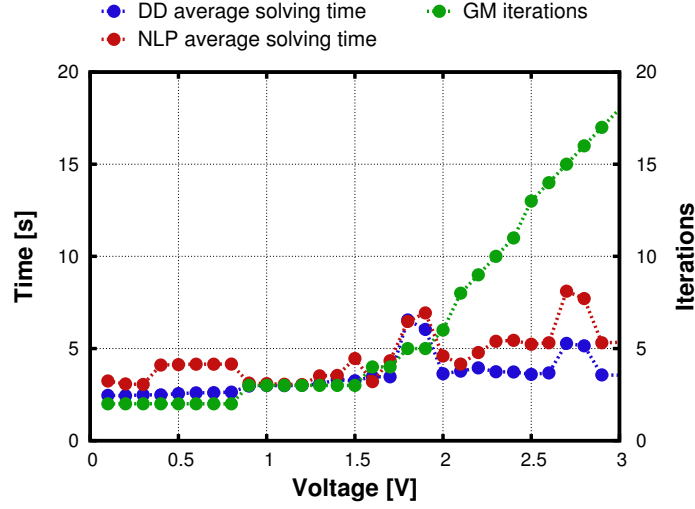


**Figure 4.10:** Time to solve the NLP and DD equations, and number of iterations of the Gummel map.

and initial guess for a bias below and above 1.5[V] (similar considerations may be done for carrier densities). When voltage is low, like in Fig.4.11a ( $V_A = 0.1[V]$ ), the potential shape is well predicted by the initial guess, resulting in a better convergence for the Gummel map algorithm. On the contrary in Fig.4.11b ( $V_A = 1.6[V]$ ) the device operates as a resistance and the potential profile is close to a linear function: this implies that the solution is far from the initial guess as equilibrium condition and the algorithm needs more steps.

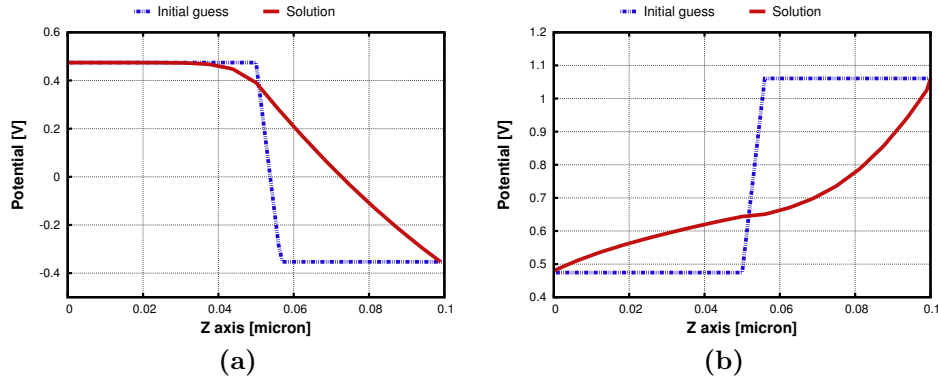


**Figure 4.11:** Initial guess for different bias compared with the final solution.

### 4.1.2 p-n junction in oxide

In this test case a silicon p-n junction  $0.3[\mu m]$  long is surrounded by an oxide layer  $0.025[\mu m]$  thick. The section of the silicon part is a  $0.1 \times 0.1[\mu m^2]$  square. We employ 6334 vertices and 33121 elements overall the domain. The structure and the doping are shown in Fig.4.12. The setting of the electrodes is similar to the previous test case and contacts are defined only on silicon surface. Tab.4.2 reports settings, models and parameters used in the simulations.

Fig.4.13 shows the solutions and the quasi Fermi potential levels along a line parallel to the Z-axis and placed at the center of the device. The main features are similar to the previous test case, also for the boundary layers at contact in carriers and quasi Fermi potentials. Figs.4.14 ÷ 4.16 show the 3D solutions for the test at  $0.3[V]$ , while Fig.4.17÷4.19 refer to the case at  $1.0[V]$ . Both the 1D cuts and 3D plots agreement with the commercial software is very good.

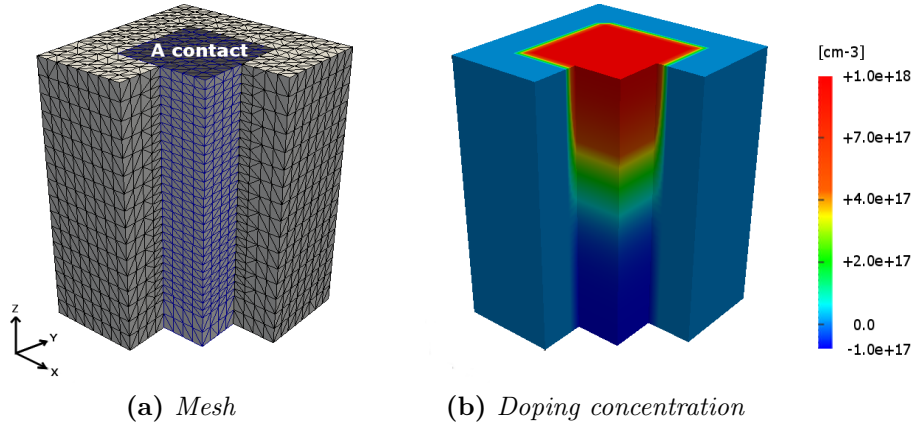


**Figure 4.12:** Test case p-n junction in oxide.

Test case [V]	Mobility model [ $cm^2V^{-1}s^{-1}$ ]	R/G model	$\epsilon_{Si}$	$\epsilon_{Ox}$
$V_A = 0.3$	$\mu_n = 1417, \mu_p = 470.5$	SRH, Auger	11.6	3.9
$V_A = 1.0$	$\mu_n = 1417, \mu_p = 470.5$	SRH, Auger	11.6	3.9

**Table 4.2:** p-n junction in oxide - list of settings, parameters and models.



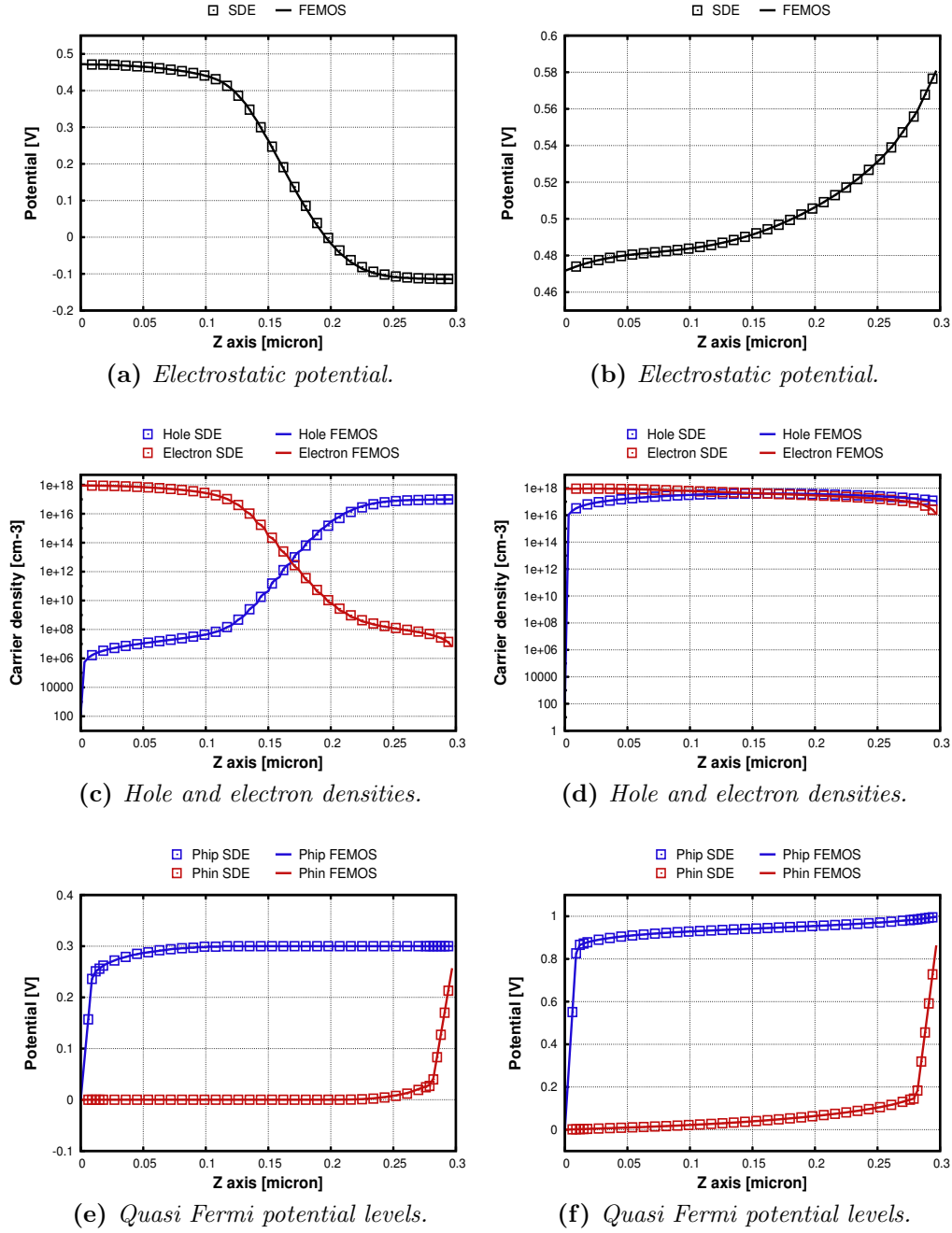


**Figure 4.13:** 1D plots of the solutions and the quasi Fermi potential levels along the line parallel to the Z-axis and placed at the center of the device. On the left test case at  $V_A = 0.3[V]$  is reported while on the right at  $V_A = 1.0[V]$ .

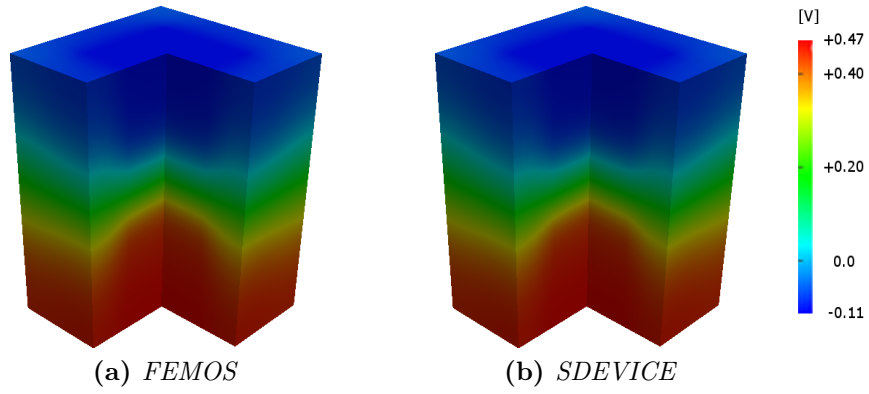


**Figure 4.14:** p-n junction in oxide 0.3[V] - ElectrostaticPotential.

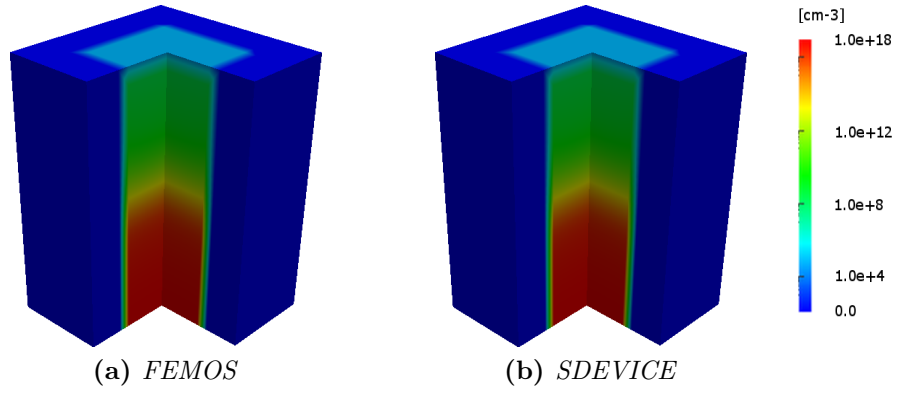


**Figure 4.15:** p-n junction in oxide 0.3[V] - Electron density.

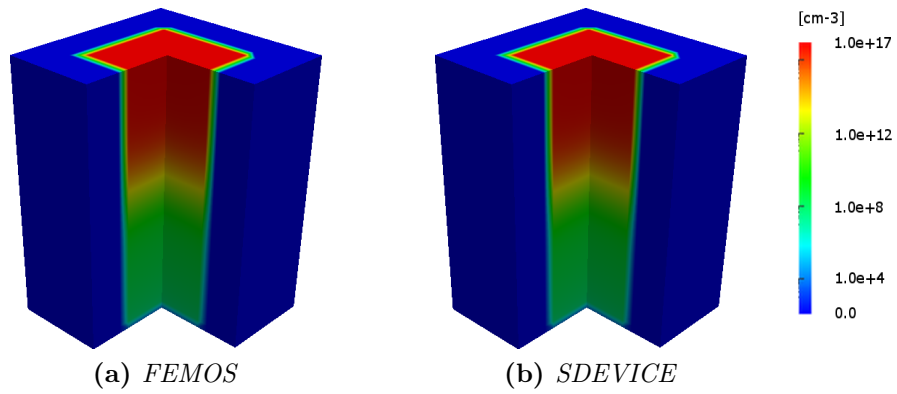


**Figure 4.16:** p-n junction in oxide 0.3[V] - Hole density.

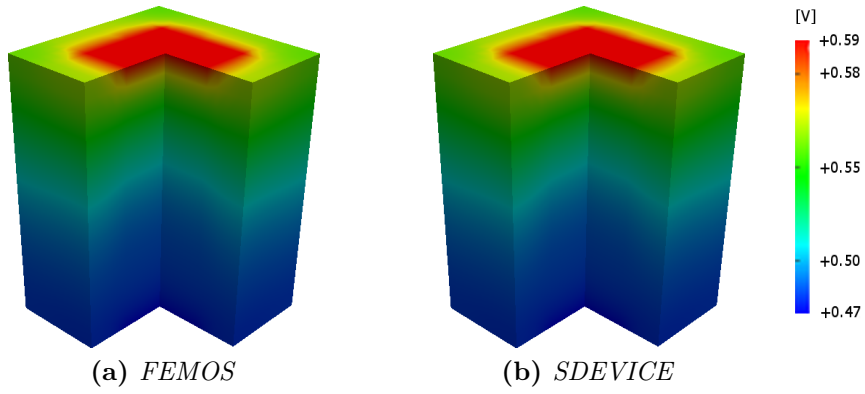


**Figure 4.17:** p-n junction in oxide 1.0[V] - Electrostatic Potential.

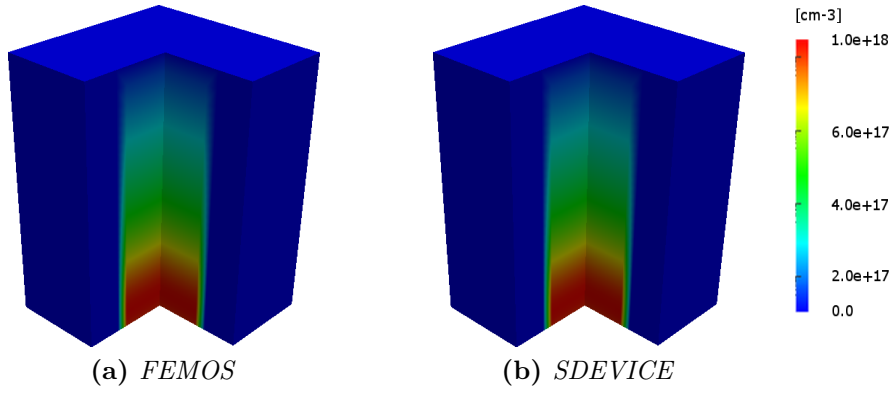


**Figure 4.18:** p-n junction in oxide 1.0[V] - Electron density.

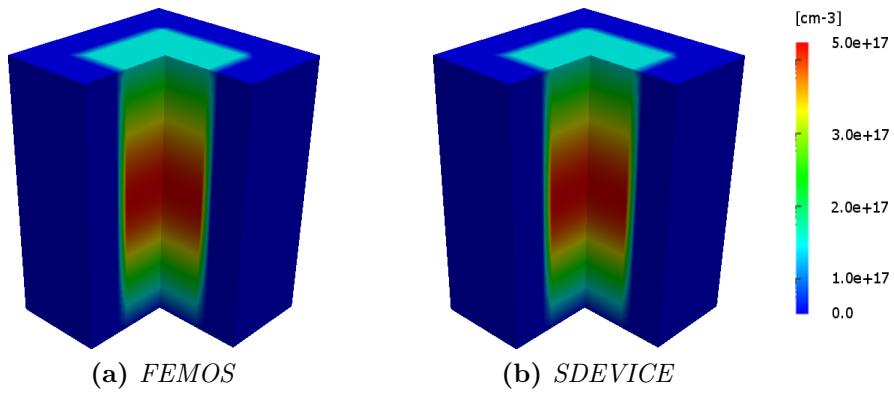


**Figure 4.19:** p-n junction in oxide 1.0[V] - Hole density.

### 3D effect on the electric field

Fig.4.14 shows how at low bias the electrostatic potential behaves in a different manner in the oxide with the respect to the silicon region. Since we impose  $\nabla\varphi \cdot \mathbf{n} = 0$  on the oxide boundary no field lines of the electric field can cross that boundary and as a consequence field lines can start and end only at contact A or B. The electric field inside the device is due only to the displacement effect in the junction of the silicon which imposes the electric response also in the oxide material where the solution is no more linear. Fig.4.20 reports the electric field lines in the case  $V_A = 0.3[V]$  compared with the commercial software. The lower magnitude of the electric field in the oxide, results in a more diffused potential.

At high bias (Fig.4.17) the influence of the contacts (A,B) becomes higher and the electrostatic potential is much more similar in the two subdomains.

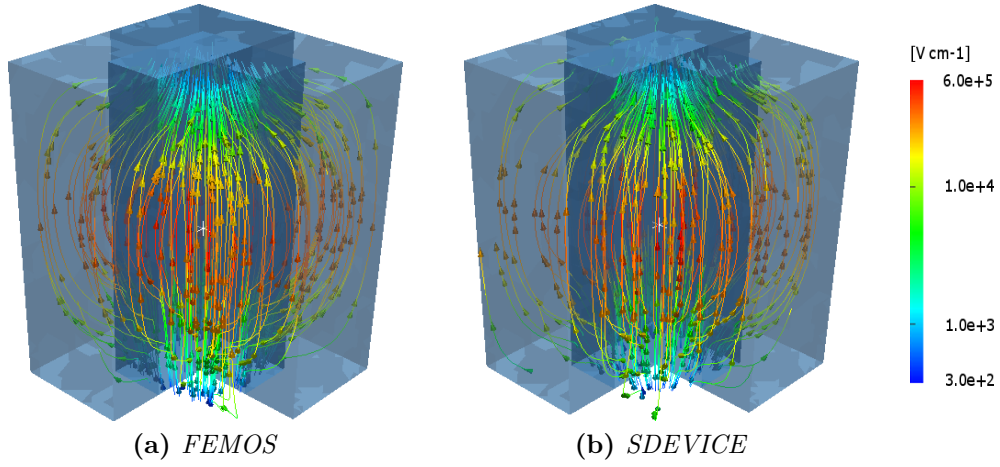


**Figure 4.20:** Test case dide p-n in oxide 0.3[V] - Electric field.

It is important to notice that the displacement formulation approach does not satisfied in a strong manner the principle of action and reaction at ? boundaries. This is equivalent to saying that given two elements  $K_i, K_j \in \mathcal{T}_h$  such that  $K_i \cap K_j = f_i$  where  $f_i \in \mathcal{F}_h$  and denoting by  $\mathbf{n}_i$  the outward normal vector of  $\partial K_i$  and  $\mathbf{n}_j$  the outward normal vector of  $\partial K_j$ , the following equations are satisfied only in a weak sense:

$$\mathbf{D}|_{K_i} \cdot \mathbf{n}_i = \mathbf{D}|_{K_j} \cdot \mathbf{n}_j \quad (4.1)$$

$$\mathbf{J}_n|_{K_i} \cdot \mathbf{n}_i = \mathbf{J}_n|_{K_j} \cdot \mathbf{n}_j \quad (4.2)$$

$$\mathbf{J}_p|_{K_i} \cdot \mathbf{n}_i = \mathbf{J}_p|_{K_j} \cdot \mathbf{n}_j. \quad (4.3)$$

In fact, taking in consideration equation (4.1), we can state that along the interface silicon-oxide the following equality holds

$$\epsilon_{ox} \mathbf{E}|_{K_i} \cdot \mathbf{n}_i = \epsilon_{Si} \mathbf{E}|_{K_j} \cdot \mathbf{n}_j \quad \Rightarrow \quad [\mathbf{E}|_{K_i}]_y = \frac{\epsilon_{Si}}{\epsilon_{ox}} [\mathbf{E}|_{K_j}]_y. \quad (4.4)$$

According with the parameters used in the simulations the jump of the electric field component from oxide to semiconductor is around 3.00. Fig.4.21 shows the plots of  $E_y$  along a line parallel to the Y-axis crossing both oxide and silicon: the ratio expressed by (4.4) is almost 3.6 at  $y = 0.05[\mu m]$  and  $y = 0.15[\mu m]$  where the interfaces are located.

Each tetrahedral interface of the partition is affected by this problem, which means that the normal component of the electric field from one element of the grid to the neighbouring is not conserved even if the material is homogeneous and there is no charge at the interface. Despite this drawback, the solutions are acceptable. But if we would satisfy equation (4.1) in a strong manner, the use of a mixed-hybrid formulation is needed which ensures the conservation of the flux also under possible strong discontinuities of material properties.

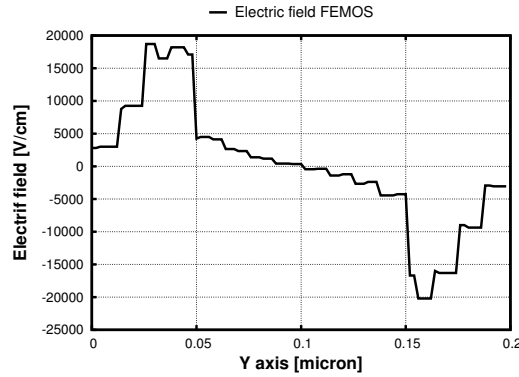


**Figure 4.21:**  $E_y$  along a line parallel to Y-axis,  $z = 0.22[\mu m]$  and  $x = 0.1[\mu m]$ .

### 4.1.3 n-channel MOSFET

The description of functioning of a MOSFET device can be found in [YT09]: it is a four-terminal device with the electrodes designated as gate (G), source (S), drain (D) and substrate or bulk (B). The gate electrode is usually made of metal or heavily doped polysilicon and is separated from the substrate by a thin silicon dioxide. The surface region under the gate oxide between source and drain is called *channel* region. Because the current in a MOSFET is due by carriers of one polarity, the MOSFET is usually referred as a unipolar or majority-carrier device: n-channel (n-MOSFET) and p-channel (p-MOSFET) are considered in the test. A *n-MOSFET* (p-MOSFET) consists of a p-type (n-type) silicon substrate into which two n-regions (p-regions) are designed as source and drain. The n-regions (p-regions) are doped according with a Gaussian profile as in a real implantation process. Fig.4.22a and Fig.4.22b show the geometry and the doping concentration for the n-MOSFET with a coarse mesh (2739 vertices and 12338 elements). We note that the mesh has been refined where the more interesting phenomena occur, i.e., along channel and at drain/source contacts.

If a sufficiently large positive voltage is applied to the gate, the silicon surface is inverted to n-type (p-type), which forms a conducting channel between the source and drain: applying a small positive voltage to the drain (source) the electrons (holes) start to flow from source (drain) to drain (source) and therefore a current is generated.

The visualization of the MOSFET working principle is better clarified in Fig.4.23 where the band profile along the channel axis is reported for two different gate bias. The voltage applied to the gate tends to decrease the energy barrier in the channel region: a little drain voltage causes the flow of the electrons. Fig.4.24a shows the profile of carrier concentrations in the

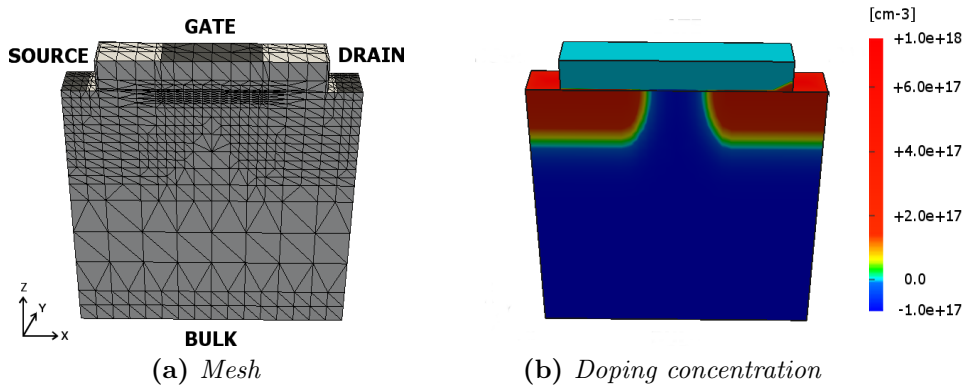


**Figure 4.22:** Geometry of a n-channel MOSFET.

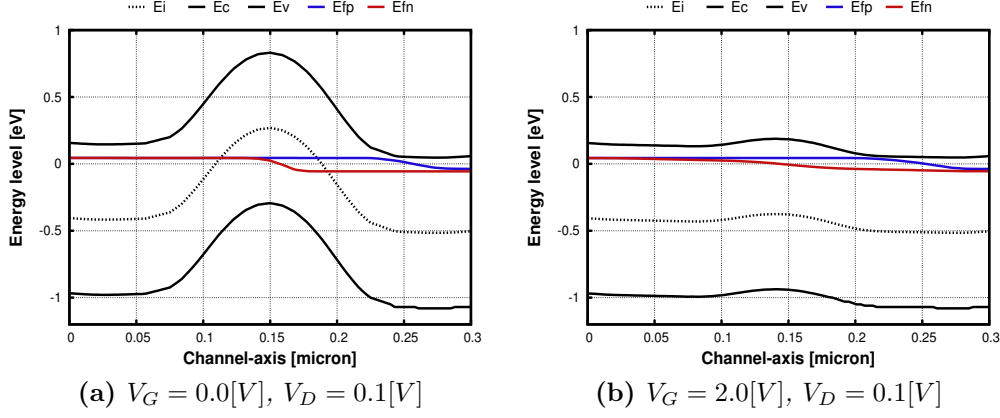


**Figure 4.23:** Energy band levels for a n-MOSFET along the channel.

middle of the channel with a cut perpendicular to the gate, for off-state and on-state: the inversion occurs when the gate voltage is higher than the well known threshold voltage. Fig.4.24b shows the 3D view of the n-channel space charge after inversion.

Finally Fig.4.25 reports the streamline plot of the electric field inside the device for FEMOS and the SDEVICE in the case of on-state MOSFET.

Settings, parameters and models used for these simulations are summarized in Tab.4.3. Figs.4.26÷4.28 show the 3D view of the electrostatic potential, electron and hole densities obtained by FEMOS and by the commercial code in the off-state ( $V_G = 0.0[V]$ ), while Figs.4.29÷4.31 refer to the on-state ( $V_G = 2.0[V]$ ): the agreement is very good.

Test case [V]	Mobility model [ $cm^2V^{-1}s^{-1}$ ]	R/G model	$\epsilon_{Si}$	$\epsilon_{0x}$
$V_G = 0.0[V]$ , $V_D = 0.0[V]$ , $V_S = V_B = 0.0[V]$	$\mu_n = 1417$ $\mu_p = 470.5$	SRH, Auger, II	11.6	3.9
$V_G = 2.0[V]$ , $V_D = 0.1[V]$ , $V_S = V_B = 0.0[V]$	$\mu_n = 1417$ $\mu_p = 470.5$	SRH, Auger	11.6	3.9

**Table 4.3:** n-MOSFET - list of settings, parameters and models.

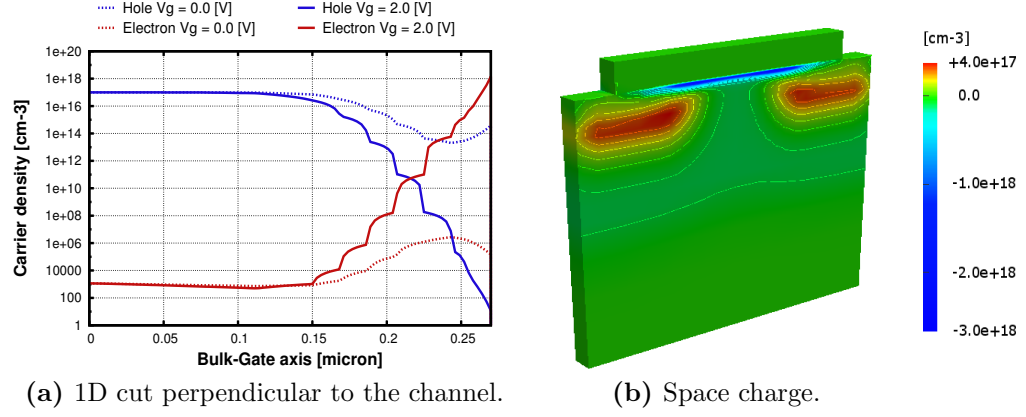


**Figure 4.24:** Channel of the n-MOSFET.

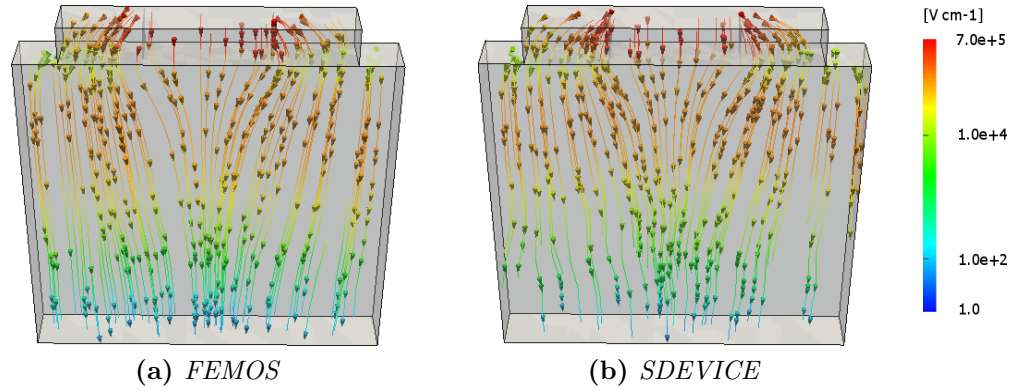


**Figure 4.25:** Electric field -  $V_G = 2.0[V]$ .



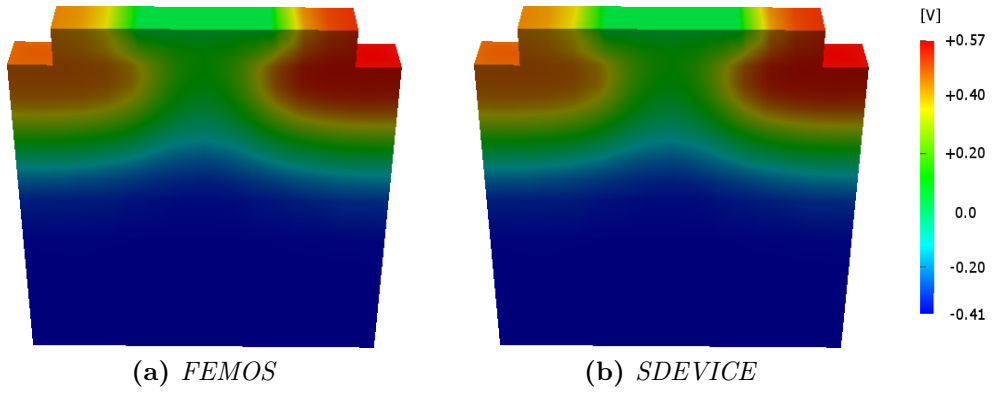


**Figure 4.26:** Electrostatic potential -  $V_G = 0.0[V]$ .

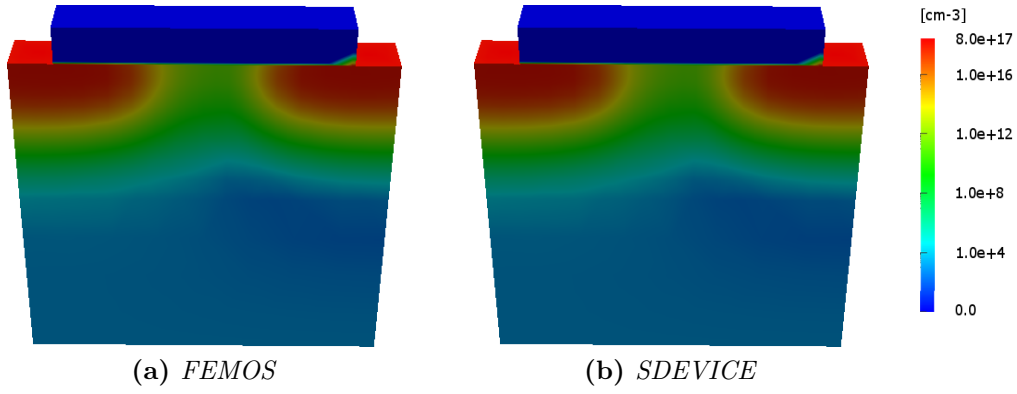


**Figure 4.27:** Electron density -  $V_G = 0.0[V]$ .

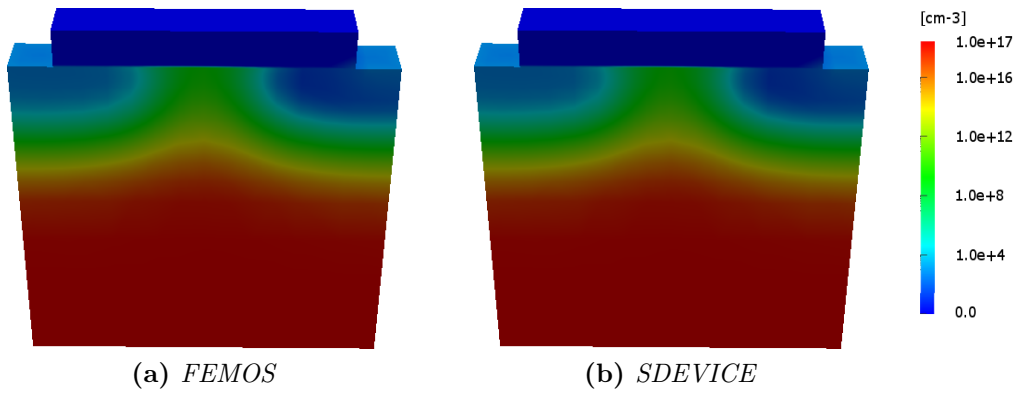


**Figure 4.28:** Hole density -  $V_G = 0.0[V]$ .

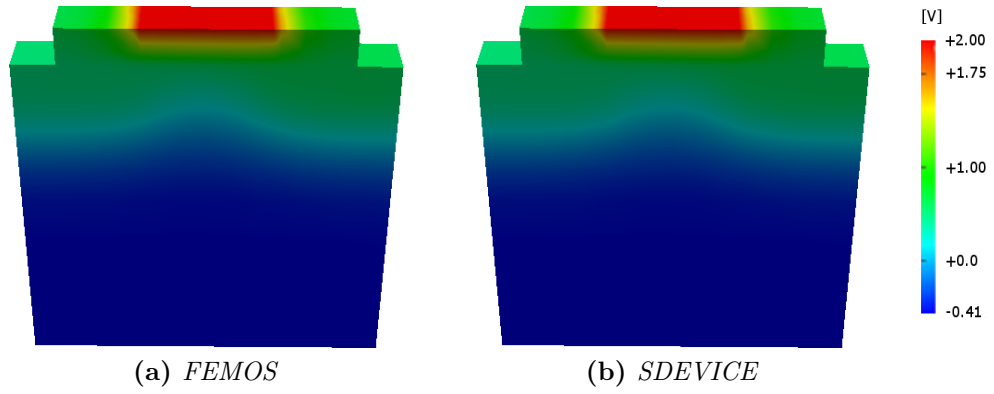


**Figure 4.29:** Electrostatic potential -  $V_G = 2.0[V]$ .

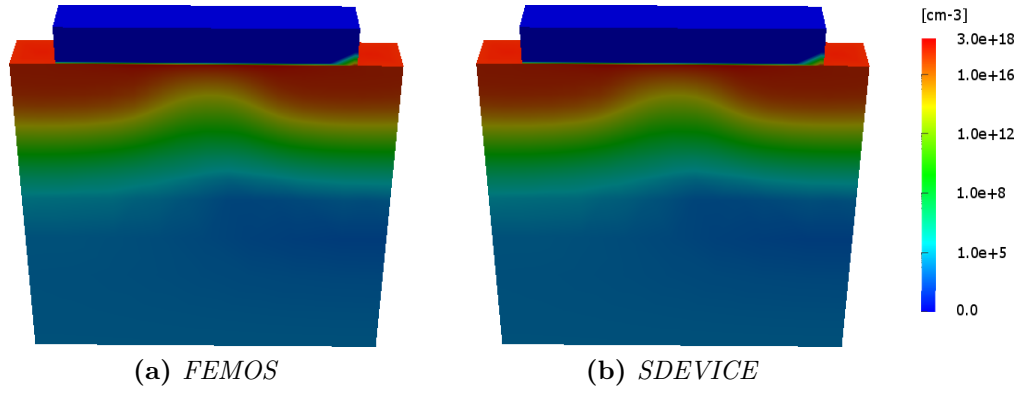


**Figure 4.30:** Electron density -  $V_G = 2.0[V]$ .

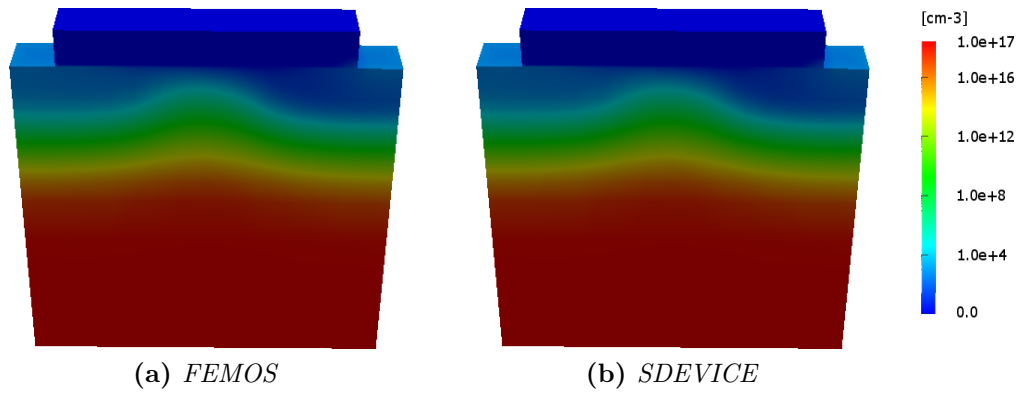


**Figure 4.31:** Hole density -  $V_G = 2.0[V]$ .

### Reverse bias

In Section 3.3.3 we pointed out that the discretization scheme (EAFE) cannot satisfy the discrete maximum principle in 3D simulations unless we satisfy condition (3.36). Therefore it is possible to encounter situations where negative solutions are obtained and this usually happens when the concentration of electrons and holes become low.

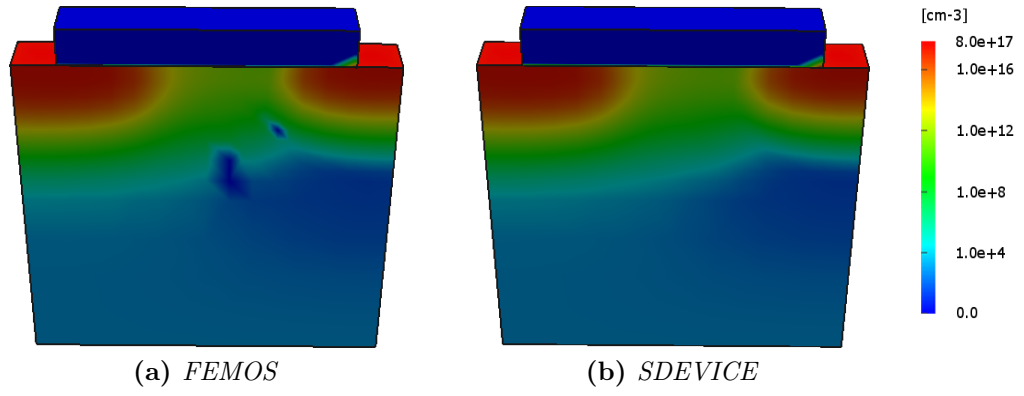
In order to highlight this possible critical situation, a n-channel MOSFET is simulated in reverse bias regime by grounding all the contacts except the drain which is ramped to 0.5[V]: Tab.4.4 reports the needed indications for the simulation.

Fig.4.32 reports the electron density computed with FEMOS and SDEVICE using the mesh presented in Fig.4.22b: the results are comparable, but near the drain-bulk junction FEMOS presents some points with negative concentrations. Increasing drain bias the phenomenon tends to spread over a larger area, until it affects irremediably the simulation of the device. As we anticipated in Chapter 3, the most practiced technique to limit this problem is local mesh refinement. Fig.4.33a represents a finer mesh with 13000 points and 67388 elements. Using this mesh the correctness of the solution is recovered Fig.4.33b. Fig.4.34 shows how the satisfaction of (3.36) changes between the different meshes: increasing the number of vertices over the critical region a better fulfillment of (3.36) is guaranteed. Results suggest that in order to treat this situation it may be useful to implement a suitable a-posteriori error estimation and adaptive mesh refinement techniques.

Finally Fig.4.35 and Fig.4.36 report FEMOS electrostatic potential and hole density for the finer mesh compared with the commercial tool: the agreement is very good.

Test case [V]	Mobility model [ $cm^2V^{-1}s^{-1}$ ]	R/G model	$\epsilon_{Si}$	$\epsilon_{0x}$
$V_G = 0.0, V_D = 0.5,$ $V_S = V_B = 0.0$	$\mu_n = 1417$ $\mu_p = 470.5$	SRH, Auger, II	11.6	3.9

**Table 4.4:** n-MOSFET (reverse bias) - list of settings, parameters and models.



**Figure 4.32:** Negative carriers spots for the electron density solution.

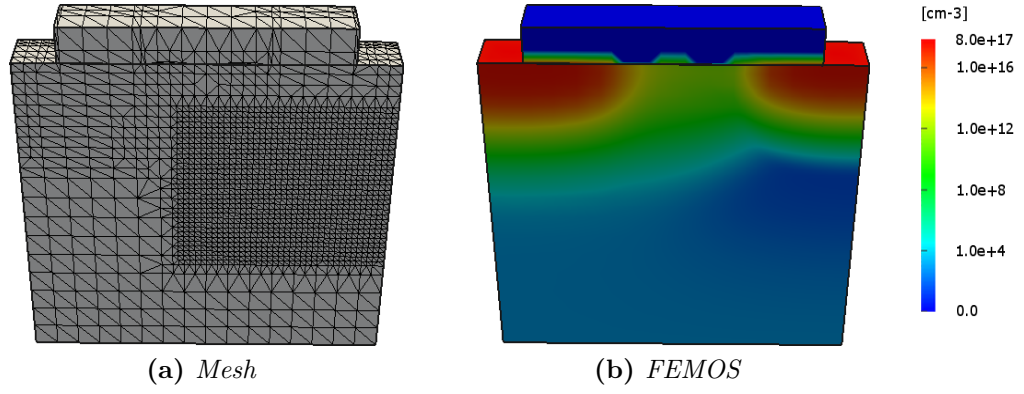


**Figure 4.33:** Electron density with finer mesh.

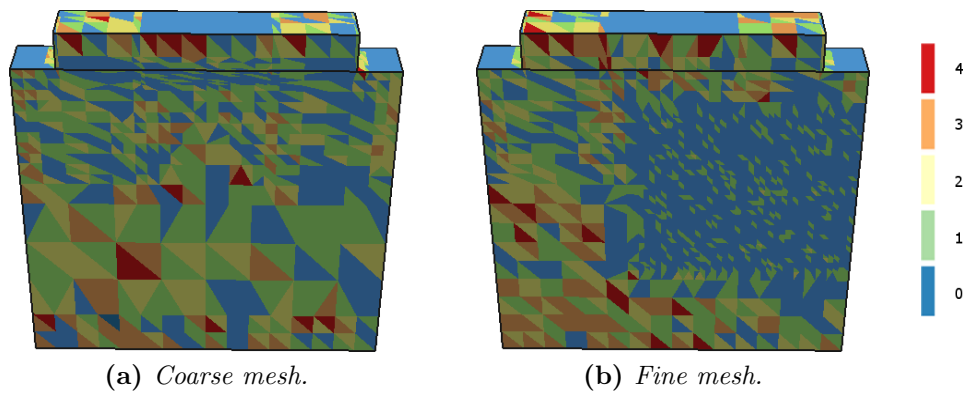


**Figure 4.34:** Zikatanov condition.

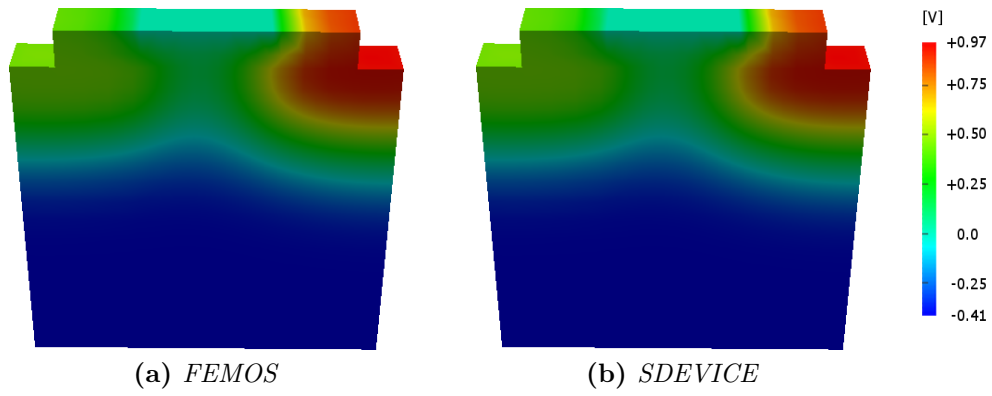


**Figure 4.35:** Electrostatic potential - Reverse bias.

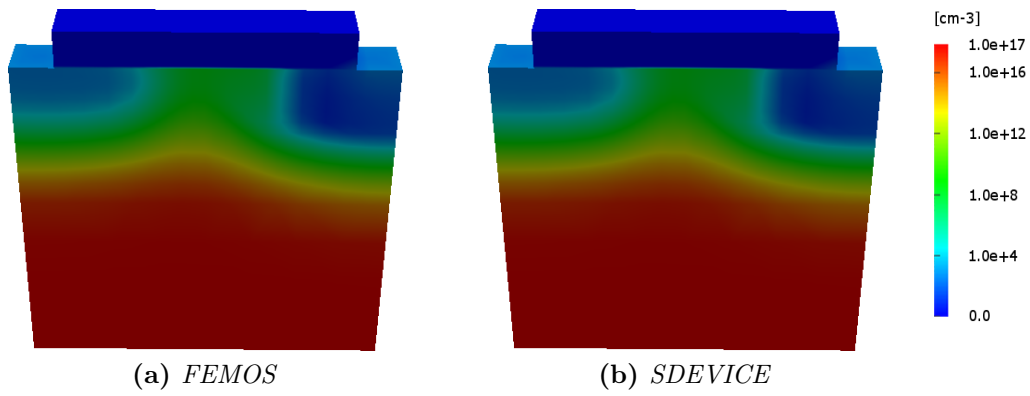


**Figure 4.36:** Hole density - Reverse bias.

## 4.2 Current evaluation at the Ohmic contacts

During the analysis of an electric device, one of the most important information is the electrical response at terminals. In order to accomplish this target we have to compute the integral of the electron and hole current density over a generic 2D electrode. We refer here to the procedure found in [GS74] (*residual method*) for the 2D case: the analysis is easily extendable to the 3D case if we consider also [HEML00]. Moreover we remark that the method can be successfully applied to a wide spread of applications, including contact charges, carrier quantum probability fluxes and heat fluxes.

A contact is defined by a surface: we can consider  $\Gamma_{D,Si} = \bigcup_{c=1}^d \Gamma_c$  where  $d$  is the number of terminals on the device and  $\forall c = 1, \dots, d$ ,  $\Gamma_c$  is the  $c$ -th contact. For each contact we need to compute the total current  $\mathcal{I}_c$  as:

$$\mathcal{I}_c = \mathcal{I}_c^n + \mathcal{I}_c^p \quad (4.5)$$

where  $\mathcal{I}_c^n$  and  $\mathcal{I}_c^p$  are the contribution of the electron and hole current. For a given contact  $\Gamma_c$ , the flux of the current density is defined as

$$\mathcal{I}_c^\nu = \int_{\Gamma_c} \mathbf{J}_\nu(\nu) \cdot \mathbf{n} d\Gamma \quad \nu = \{n, p\} \quad (4.6)$$

where  $\mathbf{n}$  is the unit outward normal of the domain boundary. It is well known that the evaluation of boundary integrals is a difficult task. Most problems in (4.6) arise from singularities in spatial derivatives of the approximate solution  $n_h$  or  $p_h$  near the contact edges, due to a change in the boundary condition type from Dirichlet to Neumann.

Let  $\eta$  be the set of all vertices of the partition  $\mathcal{T}_h$  for the discretized electron continuity problem (3.34). We can split the set of total nodes in contact nodes  $\eta_g \in \Gamma_{D,Si}$  and the complementary part  $\eta_n \in \Gamma_{N,Si}$ . We define an *auxiliary flux*  $H_h$  on  $\Gamma_{D,Si}$  as

$$H_h = \sum_{i \in \eta_g} H_{h,i} \psi_i. \quad (4.7)$$

Now, given the spaces:

$$\begin{aligned} \mathcal{V}_h &= \text{span}\{\psi_i\}_{i \in \eta_n} \\ \mathbf{V}_h &= \text{span}\{\psi_i\}_{i \in \eta_g} \\ \mathcal{S}_h &= \{u \in \mathcal{V}_h \oplus \mathbf{V}_h : u|_{\Gamma_{D,Si}} = n_D\} \end{aligned}$$

it is possible to write a modified form of Galerkin method which reads as:

find  $n_h \in \mathcal{S}_h$  and  $H_h \in \mathbf{V}_h$  such that

$$(W_h, H_h)_{\Gamma_{D,Si}} = a(W_h, n_h) - F(W_h) \quad \forall W_h \in \mathcal{V}_h \oplus \mathbf{V}_h \quad (4.8)$$

where  $a(\cdot, \cdot)$  is the bilinear form (3.34) and  $F(\cdot)$  the associated linear functional. Equation (4.8) splits into two subproblems:

$$0 = a(w_h, n_h) - F(w_h) \quad \forall w_h \in \mathcal{V}_h \quad (4.9)$$

$$(W_h, H_h)_{\Gamma_{D,Si}} = a(W_h, n_h) - F(W_h) \quad \forall W_h \in \mathbf{V}_h. \quad (4.10)$$

Problem (4.9) is identical to the unmodified case and can be treated as before or using a different discretization scheme. Once obtained the solution  $n_h$ , problem (4.10) is fully decoupled from (4.9) and we can determine  $H_h$  as follows

$$(H_h, \psi_i)_{\Gamma_{D,Si}} = a(\psi_i, n_h) - F(\psi_i) \quad \forall i \in \eta_g. \quad (4.11)$$

In [HEML00], it is shown that  $H_h$  defines the conserved total flux along  $\Gamma_{D,Si}$  and according with the boundary condition, the following equality is obtained

$$\int_{\Gamma_{D,Si}} H_h d\Gamma = - \int_{\Omega_{Si}} qR d\Omega. \quad (4.12)$$

On the other hand if we apply the divergence theorem to (2.31) we get

$$\int_{\Gamma_{D,Si}} \mathbf{J}_n \cdot \mathbf{n} d\Gamma = \int_{\Omega} -qR d\Omega. \quad (4.13)$$

Equations (4.12) and (4.13) lead us to conclude that for all contacts it holds

$$\mathcal{I}_c^n = \int_{\Gamma_c} H_h d\Gamma. \quad (4.14)$$

In order to compute (4.14), let  $\eta_c$  be the set of nodes of the contact  $\Gamma_c$ . Then, the following equalities hold

$$\sum_{l \in \eta_c} \int_{\Gamma_c} H_h \psi_l d\Gamma = \int_{\Gamma_c} H_h \sum_{l \in \eta_c} \psi_l d\Gamma = \int_{\Gamma_c} H_h d\Gamma. \quad (4.15)$$

According with (4.15) we can reinterpret  $(H_h, \psi_i)_{\Gamma_{D,Si}}$  as the contribution to the flux at node  $i$  and therefore the current at contact  $c$  is given by summing this quantity over the vertices  $\eta_c$ .

The residual method is thus defined as: given the system matrix  $A$  of the Drift-Diffusion equation, the solution  $n_h$  and the right hand side  $\mathbf{b}$ , the contribution to the total contact current  $\forall c = 1, \dots, d$  is

$$\mathcal{I}_c^n = (An_h - \mathbf{b}) \cdot \mathbb{I}_c \quad (4.16)$$

where

$$[\mathbb{I}_c]_i := \begin{cases} 0 & i \notin \eta_c \\ 1 & i \in \eta_c. \end{cases} \quad (4.17)$$

These results holds also for the hole continuity equation.

### 4.2.1 Simulation results

The residual method is applied to the devices previously presented and compared with the SDEVICE results. In this section, different mobility and recombination/generation models are tested and verified along with the commercial code solution.

#### p-n junction

Considering the p-n junction of Section 4.1.1 we ground the B contact and then A contact is ramped from  $-7.5[V]$  to  $2.0[V]$  in order to obtain the well known diode characteristic. Tab.4.5 reports the parameters used in the simulation. In Fig.4.37 we plot the electron and hole current at contact A. Diode breakdown voltage is appearing around  $-7.0[V]$  and it is quite well aligned with the SDEVICE value.

Test case [V]	Mobility model [ $cm^2V^{-1}s^{-1}$ ]	R/G model	$\epsilon_{Si}$
$V_A = -7.5 \div 1.5,$ $V_B = 0.0$	$\mu_n = 1417$ $\mu_p = 470.5$	SRH II, Auger	11.6

**Table 4.5:** p-n junction (characteristic) - list of settings, parameters and models.

Fig.4.38 shows the different behaviour of the SRH and Auger R/G contribution at two voltages (plots are made along a line parallel to the Z-axis and placed at the center of the device). Under the built-in condition, both SRH and Auger mechanisms are not significant. Auger contribution decreases in



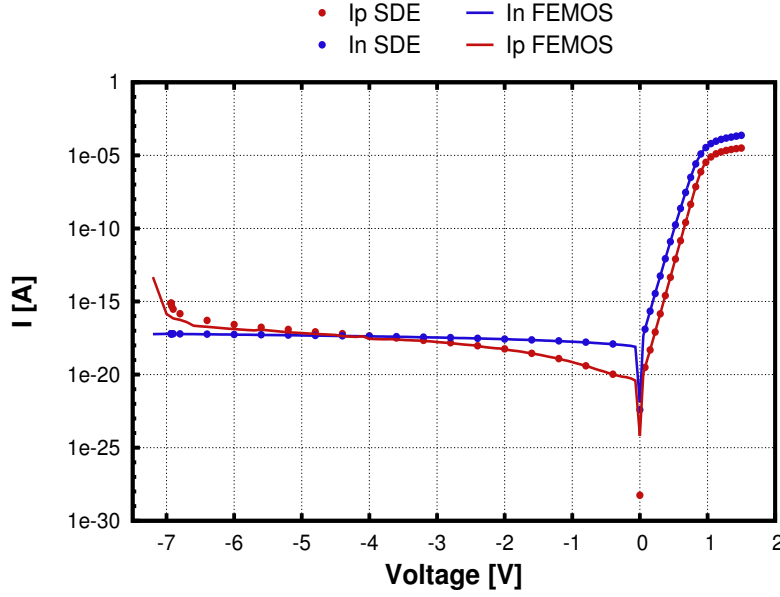


Figure 4.37: Diode characteristic.

the depletion region due to its strict dependence on the carrier concentrations. At the built-in condition the R/G phenomenon quite increase and are distributed over the entire device causing its saturation. The agreement with the commercial tool is very good.

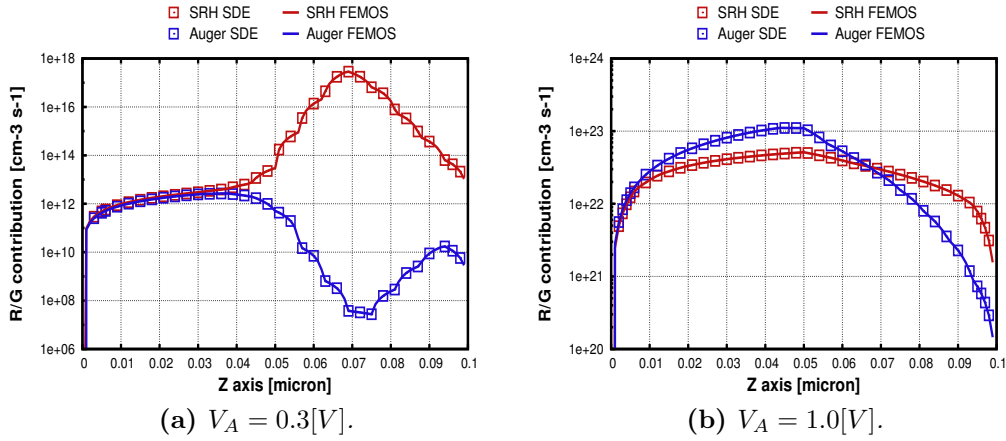
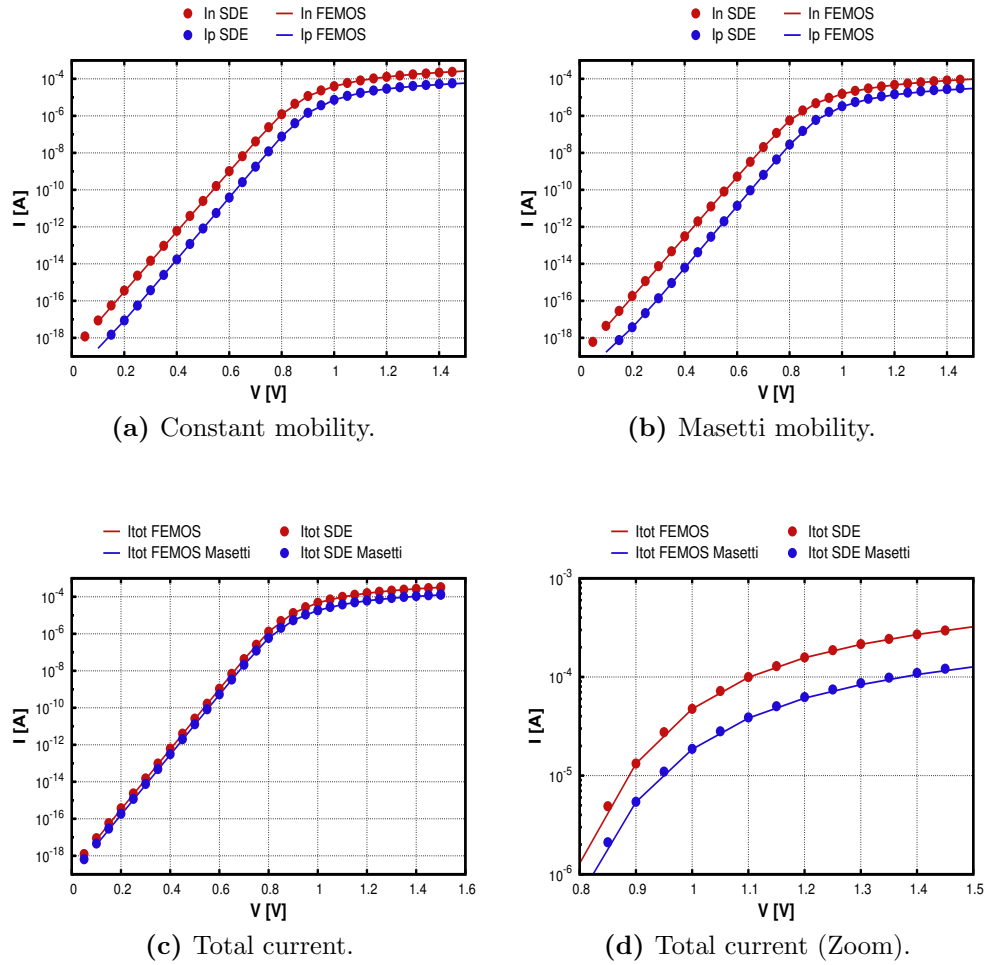


Figure 4.38: SRH and Auger RG contribution.

### p-n junction in oxide

In the case of diode in oxide we analyze the influence of the Masetti mobility model introduced in Section 1.2.3. Fig.4.39a reports electron and hole currents at contact A using the constant mobility model, while Fig.4.39b refers to the Masetti mobility model. This model predicts a decreased value of current flow due to the scattering with impurity dopants, as shown in the 1D plot proposed by Fig.4.39d. Agreement with SDEVICE is very good.



**Figure 4.39:** p-n junction in oxide current at contact - Forward bias.

Test case [V]	Mobility model [ $cm^2V^{-1}s^{-1}$ ]	R/G model	$\epsilon_{Si}$	$\epsilon_{0x}$
$V_A = 0.0 \div 1.5,$ $V_B = 0.0$	$\mu_n = 1417$ $\mu_p = 470.5$	SRH II, Auger	11.6	3.9
$V_A = 0.0 \div 1.5,$ $V_B = 0.0$	Masetti	SRH II, Auger	11.6	3.9

**Table 4.6:** p-n junction in oxide - list of settings, parameters and models.

### n-channel/p-channel MOSFET

Results for the n-MOSFET and the p-MOSFET are shown in this section. For the n-channel device we refer to Fig.4.22a while for the p-channel device Fig.4.40 shows mesh (2618 vertices and 11514 elements) and doping profile (a Gaussian profile in source and drain regions). In order to validate the code we test the following device conditions:

1.  $I_D - V_G$  characteristic at low drain bias with several mobility models;
2.  $I_D - V_G$  characteristic for different drain bias;
3.  $I_D - V_D$  characteristic in off-state (reverse bias).

Tab.4.7 and Tab.4.8 show simulation settings of the first test case for the n-MOSFET and the p-MOSFET respectively. Fig.4.41 shows the results for the n-MOSFET: Figs.4.41a÷4.41d shows how the current densities change as a function of the use of different mobility models, the agreement with SDEVICE is very good.

Similar test is performed for the p-MOSFET, but considering that a p-channel usually operates for negative values of the gate bias, we have to apply a positive bias at the source terminal. The results are shown in Fig.4.42: the agreement with SDEVICE is still good.

Fig.4.43 presents the characteristic of the n-MOSFET at different values of the drain voltage. The analogous test for the p-MOSFET is presented in Fig.4.44. Both are very well in agreement with the commercial code.

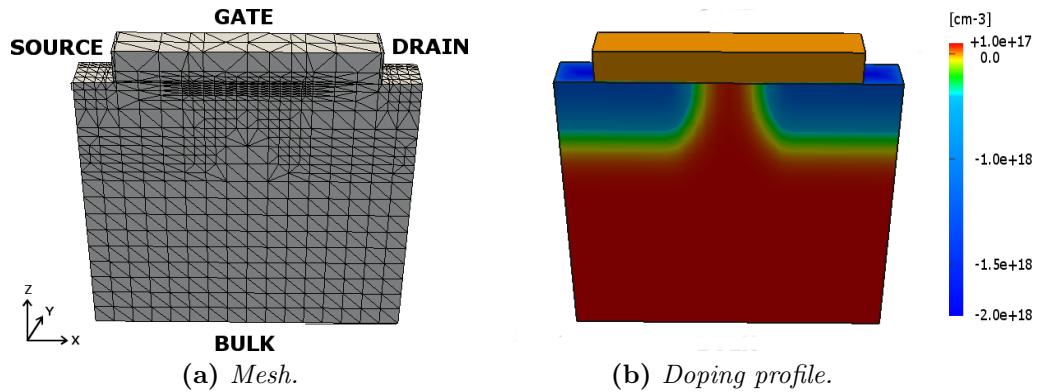
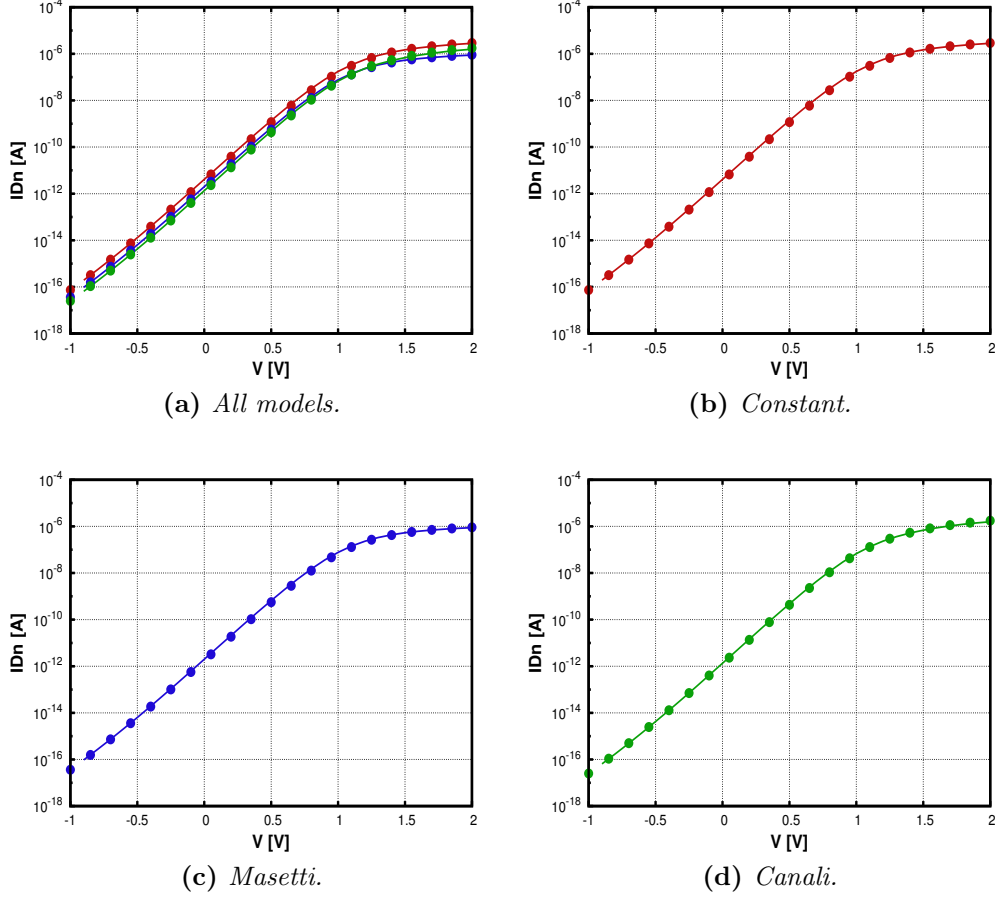
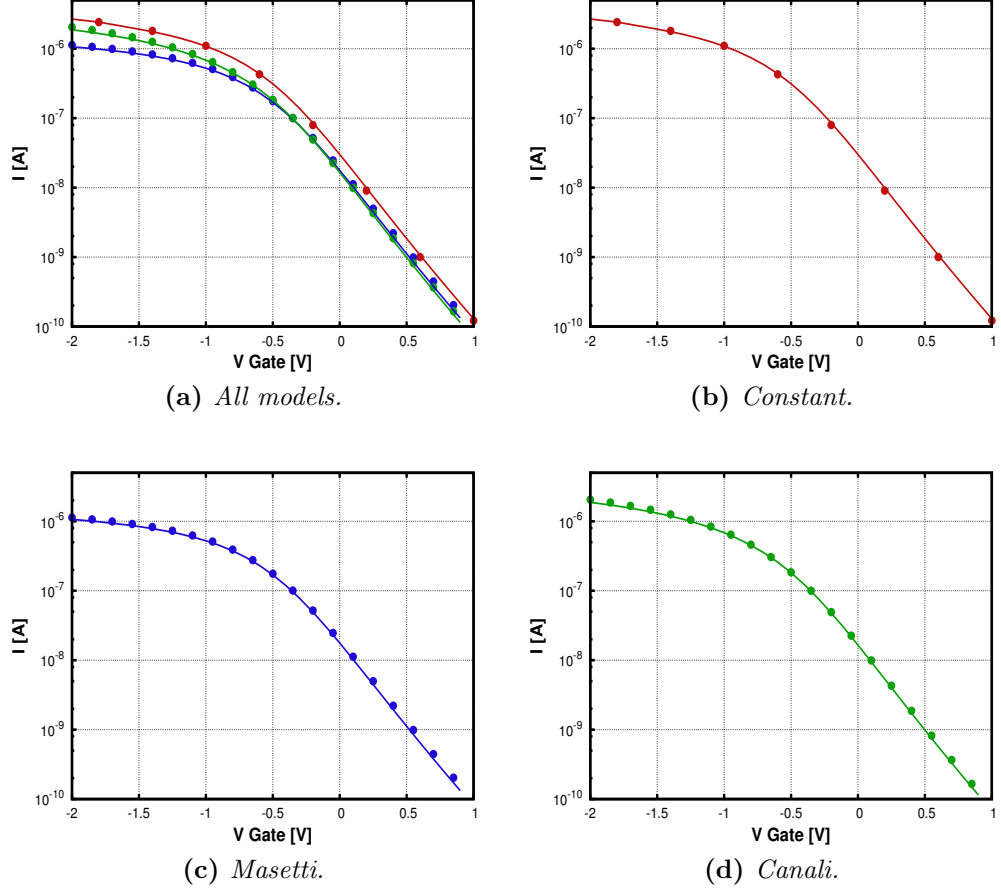


Figure 4.40: p-MOSFET.

**Figure 4.41:**  $I_D - V_G$  n-MOSFET characteristic - mobility models.

Test case [V]	Mobility model [ $cm^2V^{-1}s^{-1}$ ]	R/G model	$\epsilon_{Si}$	$\epsilon_{0x}$
$V_G = -0.5 \div 2.0,$ $V_D = 0.1, V_S = V_B = 0.0$	$\mu_n = 1417$ $\mu_p = 470.5$	SRH, Auger	11.6	3.9
$V_G = -0.5 \div 2.0,$ $V_D = 0.1, V_S = V_B = 0.0$	Masetti	SRH, Auger	11.6	3.9
$V_G = -0.5 \div 2.0,$ $V_D = 0.1, V_S = V_B = 0.0$	Canali	SRH, Auger	11.6	3.9

**Table 4.7:** n-MOSFET (low drain bias characteristic) - list of settings, parameters and models.



**Figure 4.42:**  $I_S - V_G$  p-MOSFET characteristic - mobility models.

Test case [V]	Mobility model [ $cm^2V^{-1}s^{-1}$ ]	R/G model	$\epsilon_{Si}$	$\epsilon_{0x}$
$V_G = -1.5 \div 0.5,$ $V_S = 0.1, V_D = V_B = 0.0$	$\mu_n = 1417$ $\mu_p = 470.5$	SRH, Auger	11.6	3.9
$V_G = -1.5 \div 0.5,$ $V_S = 0.1, V_D = V_B = 0.0$	Masetti	SRH, Auger	11.6	3.9
$V_G = -1.5 \div 0.5,$ $V_S = 0.1, V_D = V_B = 0.0$	Canali	SRH, Auger	11.6	3.9

**Table 4.8:** pMOSFET (low drain bias characteristic) - list of settings, parameters and models.

All values and models used for these simulations are summarized in Tab.4.9 for the n-MOSFET and Tab.4.10 for the p-MOSFET.

Test case [V]	Mobility model [ $cm^2V^{-1}s^{-1}$ ]	R/G model	$\epsilon_{Si}$	$\epsilon_{0x}$
$V_G = -0.5 \div 2.0$ , $V_D = 0.1, V_S = V_B = 0.0$	Canali	SRH, II	11.6	3.9
$V_G = -0.5 \div 2.0$ , $V_D = 0.2, V_S = V_B = 0.0$	Canali	SRH, II	11.6	3.9
$V_G = -0.5 \div 2.0$ , $V_D = 0.5, V_S = V_B = 0.0$	Canali	SRH, II	11.6	3.9
$V_G = -0.5 \div 2.0$ , $V_D = 1.0, V_S = V_B = 0.0$	Canali	SRH, II	11.6	3.9
$V_G = -0.5 \div 2.0$ , $V_D = 2.0, V_S = V_B = 0.0$	Canali	SRH, II	11.6	3.9

**Table 4.9:** n-MOSFET (different drain bias) - list of settings, parameters and models.

Test case [V]	Mobility model [ $cm^2V^{-1}s^{-1}$ ]	R/G model	$\epsilon_{Si}$	$\epsilon_{0x}$
$V_G = -1.5 \div 0.5$ , $V_S = 0.05, V_D = V_B = 0.0$	Canali	SRH, II	11.6	3.9
$V_G = -1.5 \div 0.5$ , $V_S = 0.1, V_D = V_B = 0.0$	Canali	SRH, II	11.6	3.9
$V_G = -1.5 \div 0.5$ , $V_D = 0.2, V_D = V_B = 0.0$	Canali	SRH, II	11.6	3.9
$V_G = -1.5 \div 0.5$ , $V_S = 0.5, V_D = V_B = 0.0$	Canali	SRH, II	11.6	3.9

**Table 4.10:** p-MOSFET (different drain bias) - list of settings, parameters and models.

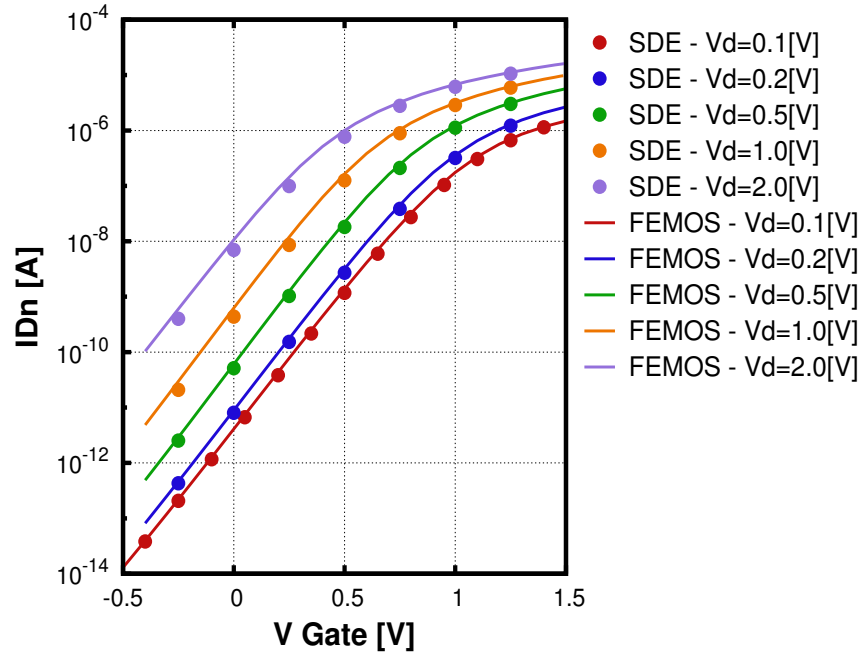


Figure 4.43:  $I_D - V_G$  n-MOSFET - several drain voltages.

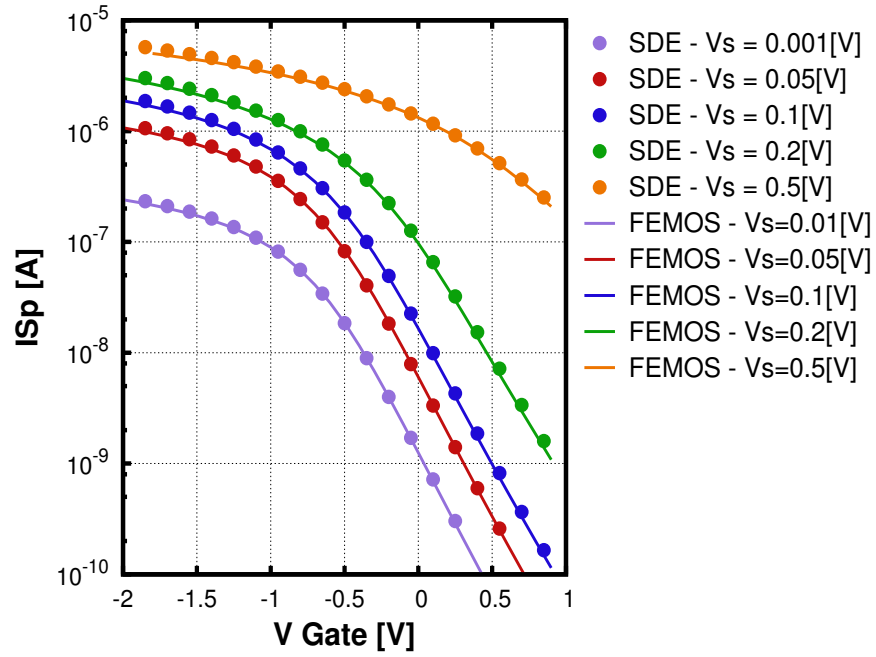


Figure 4.44:  $I_S - V_G$  p-MOSFET - several source voltages.



### Impact-ionization model

To visualize the effects of impact ionization (Van Overstraeten - de Man model see Section 1.2.2) we investigate the devices in off-state with increasing drain (n-MOSFET) or source voltage (p-MOSFET).

The parameters are summarized in Tab.4.11 for the n-MOSFET and in Tab.4.12 for the p-MOSFET.

In order to avoid possibly negative concentration also for the p-channel MOSFET, we add degrees of freedom at the source-bulk junction region as shown in Fig.4.45 (15504 vertices and 81587 elements).

For the n-MOSFET, increasing drain voltage a large amount of generation is produced around the drain-bulk junction as shown in Fig.4.46, where we compare the contribution due to II model computed at  $V_D = 0.5[V]$  between FEMOS and SDEVICE. Some differences arise but the discrepancy doesn't affect the computation of the current at contacts. Figs.4.49 and 4.50 confirm the very good agreement with the commercial tool also for the bulk current. In off-state condition no channel is formed beneath the oxide layer, therefore no preferential path is allowed for electron (or hole) conduction: carriers can move toward source (drain) and bulk contact.

Due to the difference in the doping level between n-MOSFET and p-MOSFET the generation of carriers for II is different as shown in Fig.4.46 (n-MOSFET) compared with Fig.4.47 (p-MOSFET) for  $V_S = V_D = 0.5[V]$  and Fig.4.48 also for  $V_S = 1.2[V]$ .

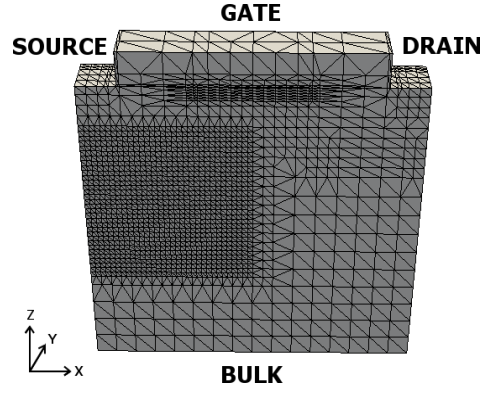


Figure 4.45: pMOSFET mesh.

Test case [V]	Mobility model [ $cm^2V^{-1}s^{-1}$ ]	R/G model	$\epsilon_{Si}$	$\epsilon_{0x}$
$V_D = 0.0 \div 1.0,$ $V_G = V_S = V_B = 0.0$	$\mu_n = 1417$ $\mu_p = 470.5$	SRH Auger, II	11.6	3.9

Table 4.11: n-MOSFET (off-state characteristic) - list of settings, parameters and models.

Test case [V]	Mobility model [ $cm^2V^{-1}s^{-1}$ ]	R/G model	$\epsilon_{Si}$	$\epsilon_{0x}$
$V_S = 0.0 \div 1.5,$ $V_G = V_D = V_B = 0.0$	$\mu_n = 1417$ $\mu_p = 470.5$	SRH Auger, II	11.6	3.9

Table 4.12: p-MOSFET (off-state characteristic) - list of settings, parameters and models.

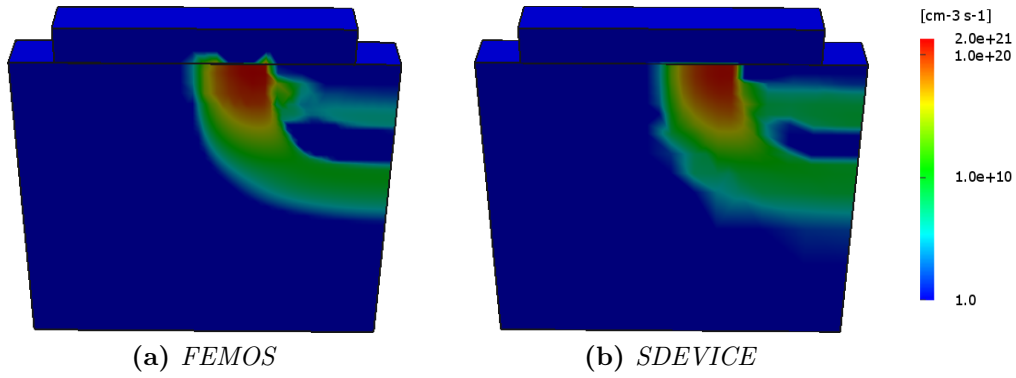


**Figure 4.46:** Contribution of the impact ionization with the Van Overstraeten - de Man model inside the n-MOSFET  $V_D = 0.5[V]$ .

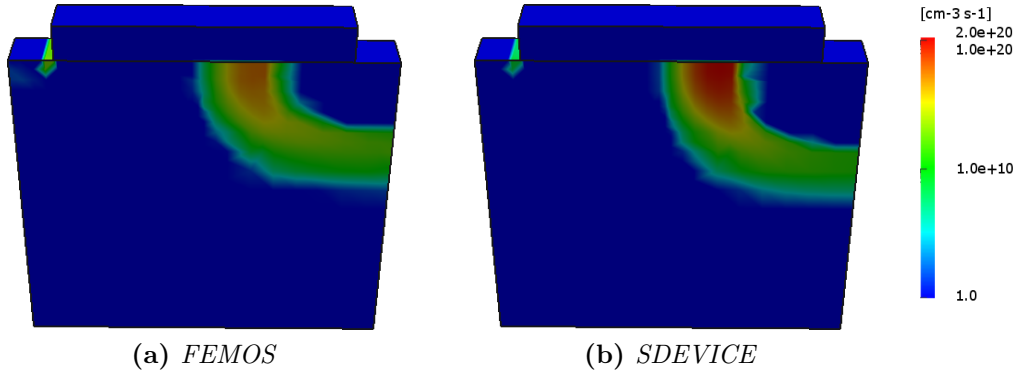


**Figure 4.47:** Contribution of the impact ionization with the Van Overstraeten - de Man model inside the p-MOSFET  $V_S = 0.5[V]$ .

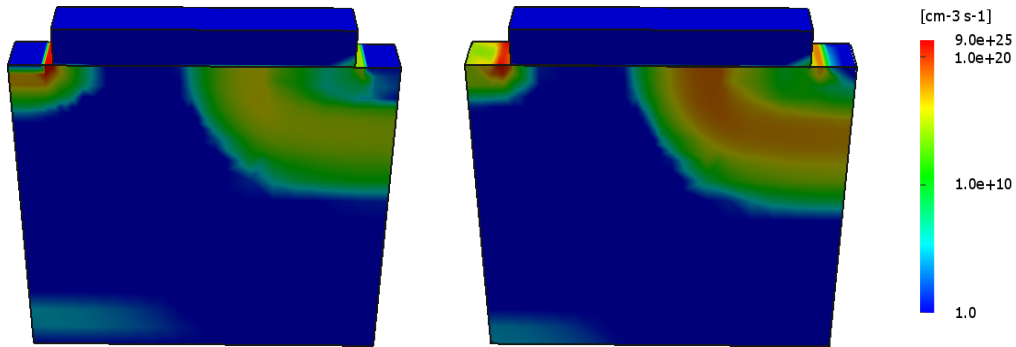


**Figure 4.48:** Contribution of the impact ionization with the Van Overstraeten - de Man model inside the p-MOSFET  $V_S = 1.2[V]$ .

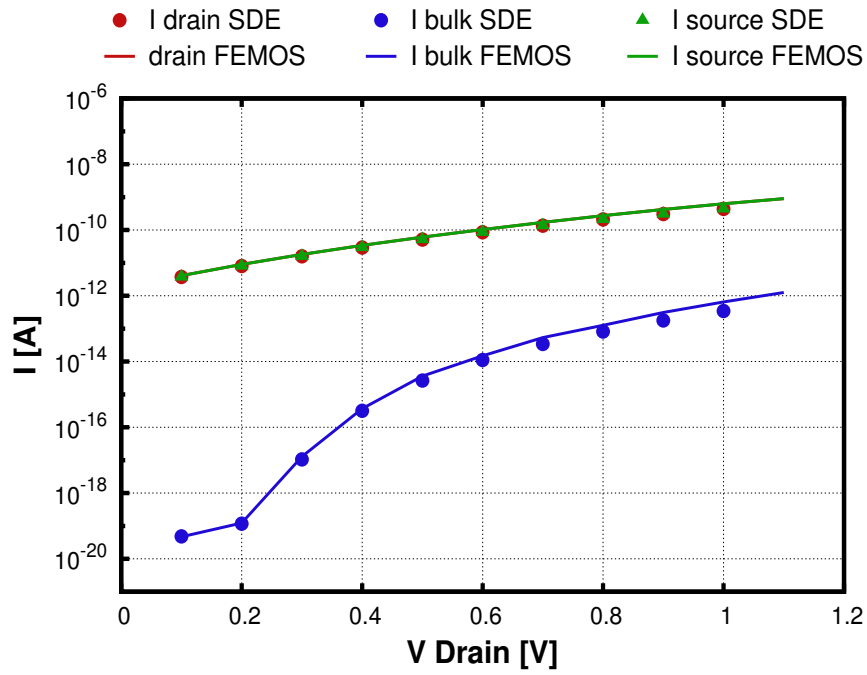


Figure 4.49: Reverse bias of the n-MOSFET.

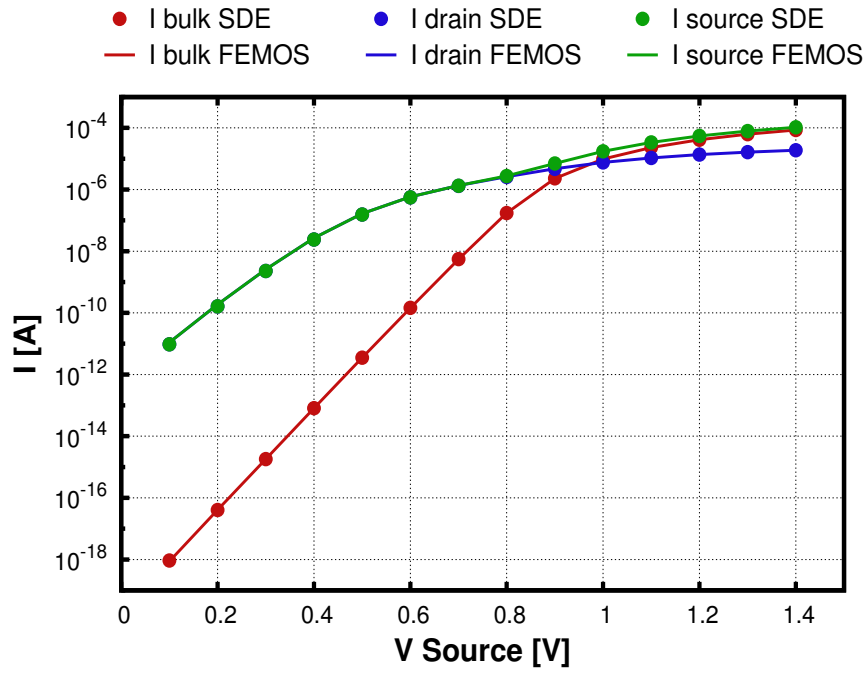


Figure 4.50: Reverse bias of the p-MOSFET.

# Chapter 5

## The current calculation problem

In many physical and engineering problems the real interesting variable of the conservation law is the flux inside the domain. The study of micro and nano electronics devices doesn't except this observation and a good description of the current density is a basic requirement.

However we recall that we chose to follow a displacement approach and this implies that the current density is not a variable of the system. Therefore we need to post-processing the carrier solutions in order to reconstruct the current density of electrons and holes.

It will be reather regrettable to lost the accuracy of our results during this computation, for this reason in this chapter we investigate some techniques in order to compute a correct current density inside the device.

### 5.1 Drift-Diffusion formula

In section 1.1.4 we saw that exist three way to represent the current density, but due to numerical issues not all of them perform a good approximation. As example we exluded from our analysis the *Slotboom equations* (1.40) (1.41) because the exponential dependency by the factor  $\varphi/V_{th}$  brings unavoidable numerical instability. The classical *Drift-Diffusion formula* (1.31) (1.32) presents also some difficulties: the drift and the diffusion contributions are respectively well defined but the combination of them brings often problematic oscillations.

Let us introduce some useful notations: with the subscript  $K$  we refer to a quantity defined on elements, while the  $h$  subscript refers to a quantity defined on vertices. The solutions  $\varphi_h$ ,  $n_h$  and  $p_h$  obtained with the discretization

scheme presented in chapter 3.3 are linear continuous functions. Accordingly to (1.31) and (1.32), in order to compute  $\mathbf{J}_n$  and  $\mathbf{J}_p$  numerical derivatives of the solutions must be done. As a consequence in this framework the discrete current densities live in different discretized spaces, indeed they are naturally constant element piecewise functions ( $\mathbf{J}_n, \mathbf{J}_p \in [X_h^0]^3$ ). If we want combine solutions and their derivatives, we have to compute appropriate projection of  $n_h$  and  $p_h$

$$\begin{aligned} n|_K &:= \langle n_h \rangle \\ p|_K &:= \langle p_h \rangle \end{aligned}$$

where with the symbol  $\langle \cdot \rangle$  we refer to a suitable average on the element, for example this operation could be the standard integral or the armonic average. If the diffusion and the mobility coefficients are variable functions of the space and defined on vertices they also have to be projected on the space  $X_h^0$ .

We implemented a numerical derivation based on the Lagrange polynomial interpolator of the first order

$$\nabla n \simeq \nabla(\Pi_h^1 n) = \sum_{i=1}^{N_h} n_i \nabla \psi_i = \nabla n_h \quad (5.1)$$

Notice that  $\nabla n_h \in X_h^0$ . The discretized form of the equations (1.34), (1.35) reads as

$$\mathbf{J}_n|_K = -qn|_K \mu_n \nabla \varphi + qD_n n|_K \nabla n_h \quad (5.2)$$

$$\mathbf{J}_p|_K = -qp|_K \mu_p \nabla \varphi - qD_p p|_K \nabla p_h \quad (5.3)$$

for the sake of the simplicity we consider only constant diffusion and mobility coefficients.

Equations (5.2) and (5.3) can be easily computed over each elements of  $\mathcal{T}_h$ , but the results are often bad.

Aggiungere figure dei contributi drift a diffusion separati e del bilancio oscillante per un caso semplice come il diodo. Aggiungere inoltre un caso con il MOS n-channel che verrà confrontato con le modifiche apportate dalla formula nella sezione upwinding.

## 5.2 Edge average techniques

It's well known that the classical Scharfetter-Gummel scheme for discretizing drift-diffusion models has proven itself to be the workhorse for semiconductor device modeling codes, indeed the EAFE scheme proposed in section 3.3.3 is strictly related to the FVSG (Finite Volume Scharfetter-Gummel) method presented by Bank, Fichtner and Rose [? ].

In this section we exposed briefly the Scharfetter-Gummel formula for a one spatial domain and we reported the extension for the 2D proposed in [? ]. Finally we present an innovative method in order to extend the Scharfetter-Gummel approach to the 3D framework.

### 5.2.1 Scharfetter-Gummel 1D

Consider the resolution of the continuity equation along a monodimensional domain. For the sake of simplicity we contemplate a uniform partition (this hypothesis is not necessary for a more generic analysis). Moreover on every nodes is defined the electrostatic potential  $\varphi$ , and on every elements the relative electrostatic field  $\mathbf{E}$ . In order to avoid redundant considerations and calculuses, we proceed with our analysis considering only the current density of electrons ( $\mathbf{J}_n$ ).

In 1969 D. Scharfetter and H.K. Gummel (two scientists of Bell Labs), introduced a formula to compute the current density in this case, given  $\varphi$  and the density solution ( $n$ ) on every nodes. This innovative approach led for the twenty years to follow every simulation which contemplates electric-devices.

We know that the constitutive law is composed by a drift component, which depends on the electric field, and a diffusion component, which depends on the variation of the carrier density. Consider a generic element  $K$ , we define the drop in voltage  $\Delta\varphi^k = \varphi_{i+1} - \varphi_i$ . There are three possible situations which are well explain in Fig.5.1:

- $\Delta\varphi \gg 0$ , mainly drift component from right to left
- $\Delta\varphi \ll 0$ , mainly drift component from left to right
- $\Delta\varphi \simeq 0$ , mainly diffusion component

With the *Scharfetter – Gummel* formula it's possibile taking into account every of these situations and solve boundary layer problems which occurs often in presence of strong drift component contribute.

$$J_n^k = q \frac{D_n}{h} \left[ n_{i+1} \mathcal{B} \left( \frac{\Delta\varphi^k}{V_{th}} \right) - n_i \mathcal{B} \left( -\frac{\Delta\varphi^k}{V_{th}} \right) \right] \quad (5.4)$$

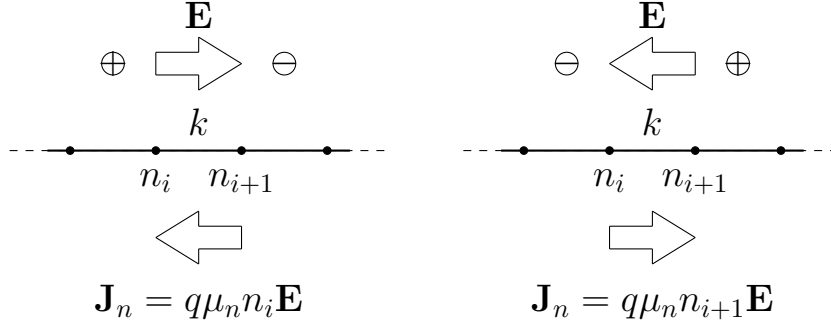


**Figure 5.1:** Effect of high electric field over the current density of electron.

In the latter case  $\Delta\varphi = 0$  the formula became:

$$J_n^k = qD_n \frac{n_{i+1} - n_i}{h} \quad (5.5)$$

which is the correct approximation of the current density using  $\mathbb{P}_1$  basis.

### 5.2.2 Scharfetter-Gummel 2D

One of the main results presented in [?] is the equivalence between the finite volume and Galerkin discretizations of the continuity equation. In order to facilitate the connection between these different discretization approaches the authors introduced for each  $K \in \mathcal{T}_h$  a linear map  $\mathcal{J}_K : \mathbb{R}^3 \rightarrow \mathbb{R}^2$  defined by

$$\mathcal{J}_K(\{\gamma_i\}_{i=1}^3) = \frac{1}{|K|} \sum_{i=1}^3 \gamma_i |e_i| s_i \mathbf{t}_i \quad (5.6)$$

where  $s_i$  is the measure of the segment from the midpoint of  $e_i$  to the intersection of the perpendicular edge bisectors and  $\mathbf{t}_i$  denote the unit tangent vector of the edge  $e_i$ .  $\mathcal{J}_K$  has the following properties:

$$\mathcal{J}_K(\{\mathbf{J} \cdot \mathbf{t}_i\}_{i=1}^3) = \mathbf{J} \quad (5.7)$$

$$\mathcal{J}_K(\{s_i^{-1}\}_{i=1}^3) = 0 \quad (5.8)$$

$$\int_K \mathcal{J}_K(\{\gamma_i\}_{i=1}^3) \cdot \nabla \psi dK = \gamma_{i+1} s_{i+1} - \gamma_{i-1} s_{i-1} \quad (5.9)$$

Equation (5.7) says that if we are able to compute the tangential component of the current density over all edges, we can combine those values accordingly with (5.6) and obtain the total current density  $\forall K \in \mathcal{T}_h$ .

We already introduced a formula for the computation of  $\mathbf{J} \cdot \mathbf{t}_i$  in section 3.3.3, indeed for the EAFE scheme in the case of electron we have



$$\mathbf{J} \cdot \mathbf{t}_i = j_{e_i} = \mathcal{H}_{e_i}(qD_n e^{(\varphi/V_{th})}) \frac{\mathcal{B}(\delta_i(\varphi/V_{th}))n_{h,k} - \mathcal{B}(-\delta_i(\varphi/V_{th}))n_{h,j}}{|e_i|} \quad (5.10)$$

similarly for the classical FVSG scheme this contribution is defined as

$$\mathbf{J} \cdot \mathbf{t}_i = j_{e_i} = \mathcal{H}_{e_i}(qD_n e^{(\varphi/V_{th})}) \nabla(e^{-\varphi/V_{th}} n_h) \cdot \mathbf{t}_i \quad (5.11)$$

where for both  $\varphi$  is the solution of the electrostatic potential given by the resolution of the non linear poisson equation.

The extension of this procedure to the 3D case is not trivial: the meaning of the cross-section  $s_i$  becomes more involved and equation (5.6) is a sum over six edges rather than three which lead to increasing computational costs and possible numerical instabilities.

### 5.2.3 Scharfetter-Gummel 3D

In the previous sections we have discussed the goodness of the Sharfetter-Gummel formula, but in the 2D case we see also that the computation of the total current density becomes more complex as the dimension of the simulation increases. In this section we present and validate an innovative method which can go beyond the above limitations.

Without loss of generality we show the procedure only for the electron continuity equation. We recall here the quasi fermi formula for the electron current density:

$$\mathbf{J}_n = -q\mu_n n \nabla \varphi_n \quad (5.12)$$

(5.12) can be rewritten considering equation (1.22):

$$\mathbf{J}_n \frac{\exp\left(\frac{\varphi_n - \varphi}{V_{th}}\right)}{q\mu_n n_i} + \nabla \varphi_n = 0 \quad (5.13)$$

Let be  $\mathbf{J}_n \in [L^2(\Omega)]^3$  and  $\varphi_n, \varphi \in H^1(\Omega)$ . We are able to multiply (5.13) with a generic function  $\mathbf{q} \in [L^2(\Omega)]^3$  and then integrate over the domain  $\Omega$ :

$$\int_{\Omega} \frac{\exp\left(\frac{\varphi_n - \varphi}{V_{th}}\right)}{q\mu_n n_i} \mathbf{J}_n \cdot \mathbf{q} d\Omega + \int_{\Omega} \nabla \varphi_n \cdot \mathbf{q} d\Omega = 0 \quad (5.14)$$

We proceed taking the usual discrete space of the constant elemenwise functions:

$$V_h = \{w \in L^2(\Omega) : w|_K \in \mathbb{P}_0 \forall K \in \mathcal{T}_h\} \quad (5.15)$$

Now the discrete quantities are  $\mathbf{J}_n^h \in [V_h]^3$  and  $\nabla \varphi_n^h \in V_h$ . We consider the following choice of the test function  $\mathbf{q}_h \in [V_h]^3$ :

$$\mathbf{q}_{1,2,3}^h = \left\{ \begin{bmatrix} 1 \\ 0 \\ 0 \end{bmatrix} \begin{bmatrix} 0 \\ 1 \\ 0 \end{bmatrix} \begin{bmatrix} 0 \\ 0 \\ 1 \end{bmatrix} \right\} \quad (5.16)$$

From (5.14) we obtain a system of equations defined for each  $K \in \mathcal{T}_h$ :

$$\int_K \frac{\exp\left(\frac{\varphi_n - \varphi}{V_{th}}\right)}{q\mu_n n_i} \mathbf{J}_n^h \cdot \mathbf{q}_i^h dK + \int_K \nabla \varphi_n^h \cdot \mathbf{q}_i^h dK = 0 \quad \forall i = 1, 2, 3 \quad (5.17)$$

After the integration we obtain the formula for the generic component of the current density:

$$[\mathbf{J}_n]_i = -\mathcal{H}_K \left( q\mu_n n_i \exp\left(\frac{\varphi - \varphi_n}{V_{th}}\right) \right) \frac{\partial \varphi_n^h}{\partial x_i} \quad i = 1 \dots d \quad \forall K \in \mathcal{T}_h \quad (5.18)$$

We have no intention to resolve the harmonic average with a complete 3D integration which may be expensive in calculation time. Therefore we suppose that there is an edge of  $K$  such that

$$\left( \frac{\int_K f^{-1} dK}{|K|} \right)^{-1} \simeq \left( \frac{\int_{e^*} f^{-1} de}{|e^*|} \right)^{-1} \quad (5.19)$$

where  $f = q\mu_n n_i \exp((\varphi - \varphi_n)/V_{th})$ . We are assuming that the diffusive coefficient could be predicted if we consider only the edge where the phenomena is more significative rather than the entire element. In order to define which is the correct edge consider a quantity defined on the vertices

$$\Phi := \varphi - \varphi_n \quad (5.20)$$

which is the difference between the electrostatic potential and the quasi fermi potential level. Now for every element consider two vertices:  $\mathbf{x}_m$  s.t.  $\Phi(\mathbf{x}_m) = \Phi_m := \min_K(\Phi)$  and  $\mathbf{x}_M$  s.t.  $\Phi(\mathbf{x}_M) = \Phi_M := \max_K(\Phi)$ . Obviously it exists only one edge which connects these two points and on this one we perform the 1D integration (5.19).

Along the edge  $e^*$  we can consider

$$f(s) = q\mu_n n_i \exp\left(\Phi_m + (\Phi_M - \Phi_m) \frac{s - s_m}{|e^*|}\right) \quad (5.21)$$

where  $s \in [s_m, s_M]$  is the parameter referred to the edge  $e^*$  s.t.  $f(s_m) = f(\mathbf{x}_m)$  and  $f(s_M) = f(\mathbf{x}_M)$ . We can solve (5.19) with the following change in variable

$$\eta := \frac{s - s_m}{|e^*|}$$

and proceed with trivial integration steps

$$\begin{aligned} \int_{e^*} f^{-1} de &= |e^*| \int_0^1 \frac{\exp(-\Phi_m - (\Phi_M - \Phi_m)\eta)}{q\mu_n n_i} d\eta \\ &= |e^*| \frac{\exp(-\Phi_m)}{q\mu_n n_i} \frac{\exp(\Phi_m - \Phi_M) - 1}{\Phi_m - \Phi_M} \\ &= |e^*| \frac{\exp(-\Phi_m)}{q\mu_n n_i} \frac{1}{\mathbf{B}(\Phi_m - \Phi_M)} \end{aligned}$$

finally we obtain

$$\int_K f^{-1} dK \simeq q\mu_n n_i \exp(\Phi_m) \mathbf{B}(\Phi_m - \Phi_M) \quad (5.22)$$

Similar results may be obtained repeating the integration and considering  $s_M$  as start point:

$$\int_K f^{-1} dK \simeq q\mu_n n_i \exp(\Phi_M) \mathbf{B}(\Phi_M - \Phi_m) \quad (5.23)$$

Equation (5.22) and (5.23) can be combined and find

$$\mathbf{J}_n|_K = -q\mu_n \left[ \frac{n_{min} \mathbf{B}(-\Delta\Phi_{max}) + n_{max} \mathbf{B}(\Delta\Phi_{max})}{2} \right] \nabla \varphi_n^h \quad (5.24)$$

where  $n_{min} = n_i e^{\Phi_m}$  and  $n_{max} = n_i e^{\Phi_M}$ .

If we consider equation (5.24) over a one spatial domain we can recover equation (5.4), then we can say that this approach is the natural extension of the *Sharfetter – Gummel* formula for the 3D case.

### 5.3 Upwinding techniques

It's well known that classical finite element method is unstable when the Péclet number ( $\mathbb{P}e$ ) is large. Coefficient  $\mathbb{P}e$  includes the influence of the drift component and is proportional to the product  $|\nabla\varphi|h$ . Therefore the presence of boundary layers for the electrostatic potential makes problematic the resolution of the continuity equation. This has led to the use of upwind finite element techniques: in one spatial domain this contribution is written as artificial diffusion term which modifies the convection diffusion equation. Generally speaking we can define a function  $\Phi$  of the Péclet number such that

$$\lim_{h \rightarrow 0} \Phi = 0 \quad (5.25)$$

The perturbed problem in the case of the electron continuity equation becomes

$$-\nabla \cdot (qD_n(1 + \Phi)\nabla n - q\mu_n n \nabla \varphi) = -qR \quad (5.26)$$

Similarly the new weak form is

$$a_h(n, v) = a(n, v) + \int_{\Omega} \Phi \nabla n \cdot \nabla v \, d\Omega \quad (5.27)$$

Property (5.25) is fundamental in order to guarantee the consistence of (5.27) with respect to the standard Galerkin weak form.

Considering the framework just presented the *Sharfetter-Gummel* discretization scheme in one spatial domain can be obtained using the following shape for the function  $\Phi$

$$\Phi = \mathcal{B}(2\mathbb{P}e) + \mathbb{P}e - 1 \quad (5.28)$$

It's possible deduce equation (5.28) considering (1.34) and (1.35) in some interesting borderline cases:

- **Constant carriers**, in the semiconductor device we have a current density due only to the drift contribution

$$\begin{aligned} \mathbf{J}_n &= q\mu_n n \mathbf{E} \\ \mathbf{J}_p &= q\mu_p p \mathbf{E} \end{aligned}$$

- **Constant potential**, then we have  $\mathbf{E} = 0$  and the current density is due only to the diffusive contribution

$$\begin{aligned}\mathbf{J}_n &= qD_n \nabla n \\ \mathbf{J}_p &= -qD_p \nabla p\end{aligned}$$

- **Constant quasi fermi potential**, then we have  $n = C_1 e^{\varphi/V_{th}}$  and  $p = C_2 e^{-\varphi/V_{th}}$  where  $C_1$  and  $C_2$  are two arbitrary constants such that

$$C_1 = \exp(-\varphi_n/V_{th}) \quad C_2 = \exp(\varphi_p/V_{th})$$

Considering this hypothesis from equations (1.34) and (1.35) we can establish that

$$\begin{aligned}\mathbf{J}_n &= -q\mu_n(n\nabla\varphi - V_{th}(\frac{C_1}{V_{th}}\nabla\varphi e^{\varphi/V_{th}})) = 0 \\ \mathbf{J}_p &= -q\mu_p(p\nabla\varphi + V_{th}(-\frac{C_1}{V_{th}}\nabla\varphi e^{-\varphi/V_{th}})) = 0\end{aligned}$$

Take into account constant quasi fermi potential lead to thermodynamical equilibrium condition for the carrier densities and this implies no current densities.

Consider the following perturbation of (5.2) restricted to a single element  $K$  included between two vertices (for the sake of simplicity we consider local indices for the vertices)

$$J_n|_K = -q\mu_n \langle n_h \rangle \partial_x \varphi_h + qD_{n,h} \partial_x n_h \quad (5.29)$$

where

$$\begin{aligned}D_{n,h} &= (1 + \Phi_K(\mathbb{P}e))D_n \\ \langle n_h \rangle &= \frac{\int_K n_h dx}{|K|} = \frac{n_1 + n_2}{2} \\ \partial_x \varphi_h &= \frac{\varphi_2 - \varphi_1}{h} = \frac{\Delta\varphi}{h} \\ \partial_x n_h &= \frac{n_2 - n_1}{h}\end{aligned}$$

Equation (5.28) can be obtained imposing that

$$J_n|_K(\Pi_1^k(Ce^{\varphi/V_{th}})) = 0 \quad (5.30)$$

From (5.29) we have

$$\begin{aligned} q\mu_n < n_h > \partial_x \varphi_h &= qD_n(1 + \Phi_K)\partial_x n_h \\ < n_h > \partial_x \varphi_h &= V_{th}(1 + \Phi_K)\partial_x n_h \\ \Phi_K &= \sigma \mathbb{P}e \frac{n_1 + n_2}{n_2 - n_1} - 1 \end{aligned}$$

where

$$\begin{aligned} \mathbb{P}e &= \frac{\partial_x \varphi_h h}{2V_{th}} = \frac{\Delta\varphi}{2V_{th}} \\ \sigma &= \text{sign}(\Delta\varphi) \end{aligned}$$

Now we impose the constant quasi fermi potential hypothesis

$$\begin{aligned} \Phi_K &= \sigma \mathbb{P}e \frac{e^{\varphi_1/V_{th}} + e^{\varphi_2/V_{th}}}{e^{\varphi_2/V_{th}} - e^{\varphi_1/V_{th}}} - 1 \\ &= \sigma \mathbb{P}e \frac{e^{\Delta\varphi/V_{th}} + 1}{e^{\Delta\varphi/V_{th}} - 1} - 1 \\ &= \sigma \mathbb{P}e \frac{e^{2\sigma \mathbb{P}e} + 1}{e^{2\sigma \mathbb{P}e} - 1} - 1 \end{aligned}$$

Considering  $X := 2\sigma \mathbb{P}e$  we have

$$\begin{aligned} \Phi_K &= \frac{X}{2} \left( \frac{e^X}{e^X - 1} + \frac{1}{e^X - 1} \right) - 1 \\ &= \frac{1}{2} (\mathcal{B}(-X) + \mathcal{B}(X)) - 1 \\ &= \frac{1}{2} (X + \mathcal{B}(X) + \mathcal{B}(X)) - 1 \\ &= \mathcal{B}(X) + \frac{X}{2} - 1 \end{aligned}$$

Replacing  $X$  we obtain for both  $\Delta\varphi > 0$  and  $\Delta\varphi < 0$

$$\Phi_K = \mathcal{B}(2\mathbb{P}e) + \mathbb{P}e - 1 \quad (5.31)$$

From these calculations we can say that a simple extension for the 3D case of the Scharfetter-Gummel stabilization could be found considering a 3D vector  $\Phi^k$  defined on each elements as follows

$$[\Phi|_K]_i = -\frac{\langle \Pi_1^k(e^{\varphi/V_{th}}) \rangle \partial_{x_i} \varphi}{\partial_{x_i} \Pi_1^k(e^{\varphi/V_{th}}) V_{th}} - 1 \quad i = 1, 2, 3, \quad (5.32)$$

In (5.33) the argument of the exponential could be an high variable function, therefore it's preferable consider a reference value for the electrostatic potential. Observe that  $\varphi \in [\varphi_{min}, \varphi_{max}]$  and therefore we can use one of these values as reference and obtain

$$[\Phi|_K]_i = -\frac{\langle \Pi_1^k(e^{(\varphi - \varphi_{min})/V_{th}}) \rangle \partial_{x_i} \varphi}{\partial_{x_i} \Pi_1^k(e^{(\varphi - \varphi_{min})/V_{th}}) V_{th}} - 1 \quad i = 1, 2, 3, \quad (5.33)$$

### 5.3.1 Results

In this section we compare the performance of the different current computation methods. The test problems are the p-n junction presented in Tab.4.1 with  $V_A = 1.0[V]$  and the nMOSFET Tab.4.3 in on-state condition. The procedures considered are:

- **Drift-Diffusion** defined by (5.2) and (5.3) with  $n|_K = \mathcal{M}(n_h)$ , where  $\mathcal{M}(\cdot)$  is the standard integral average;
- **Scharfetter-Gummel 3D** method described in section 5.2.3;
- **Modified Drift-Diffusion** which is for the electron current density

$$\mathbf{J}_n|_K = -qn|_K \mu_n \nabla \varphi + qD_n n|_K (\mathcal{I} + \mathcal{I} \Phi_K) \nabla n_h \quad (5.34)$$

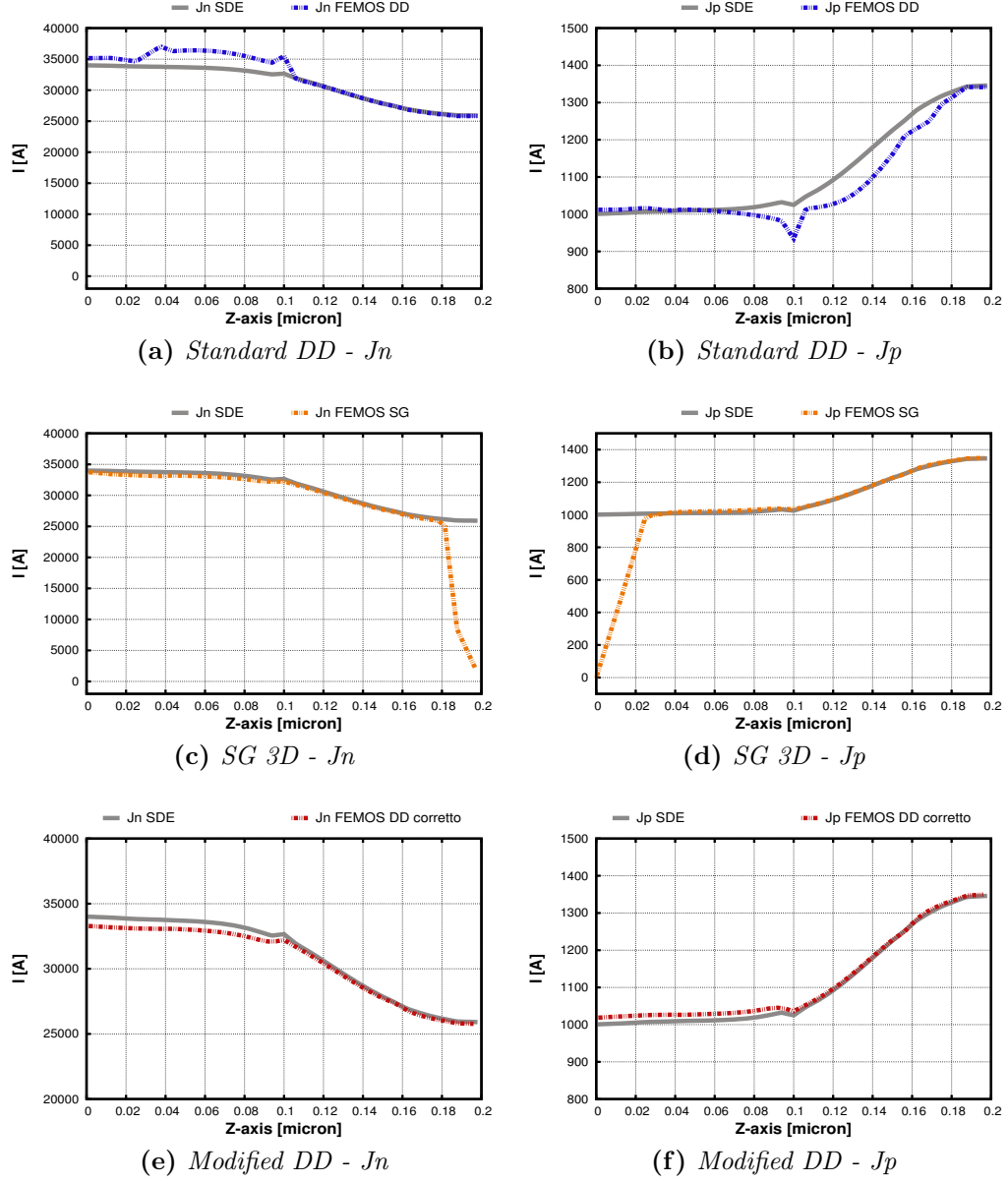
considering  $n|_K = \mathcal{M}(n_h)$  and  $\Phi_K$  as equation (5.33).

The comparison currents for the p-n junction are depicted in Fig.5.2 using 1D plots along a line parallel to the Z-axis and placed at the center of the device. Both electron and hole current densities are shown for the three methods.

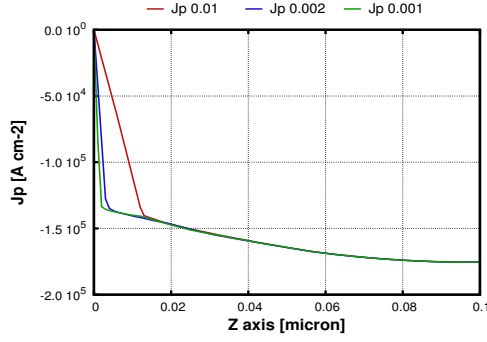
Apparently from this test case the best result is obtained with the modified DD method, as the standard DD is unstable and the SG 3D computes wrong values next to the contacts. Although the latter problem is strictly related with the mesh refinement, indeed fig shows the results

Aggiungere le figure del diodo in 3D

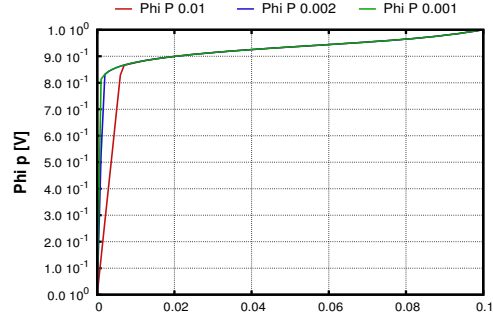
When  $(\varphi_{max} - \varphi_{min})$  is small or when the diode is in high direct polarization the modified technique works (Fig.5.3) better than the Drift-Diffusion formula (Fig.5.5).

Figure 5.2: 1D plot p-n junction -  $V_A = 1.0[V]$

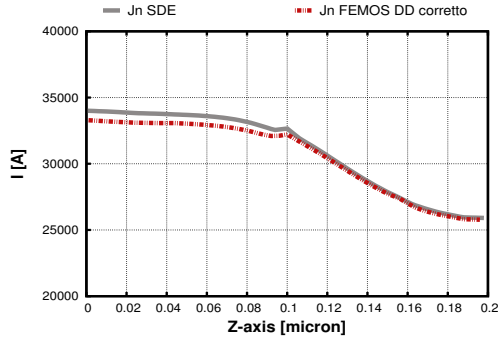
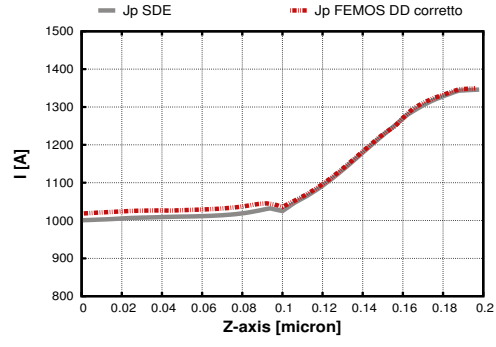
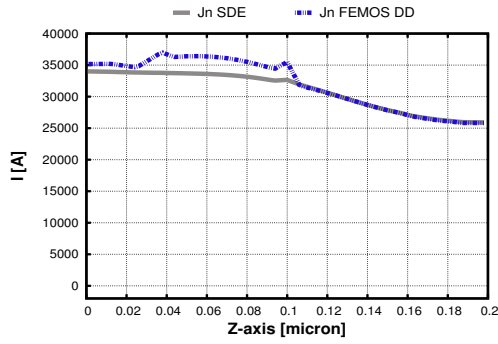
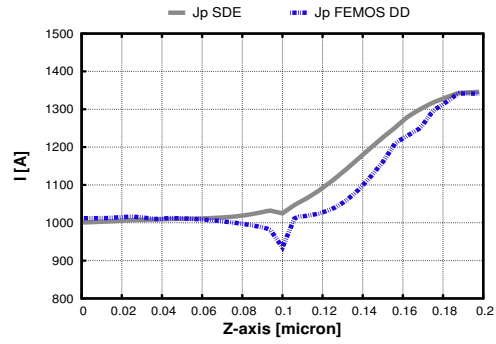




(a) Hole current density.



(b) Hole quasi fermi potential.

(a)  $J_n$ (b)  $J_p$ Figure 5.3: 1D plot p-n junction -  $V_A = 1.0[V]$ .(a)  $J_n$ (b)  $J_p$ Figure 5.4: 1D plot p-n junction -  $V_A = 1.0[V]$ .

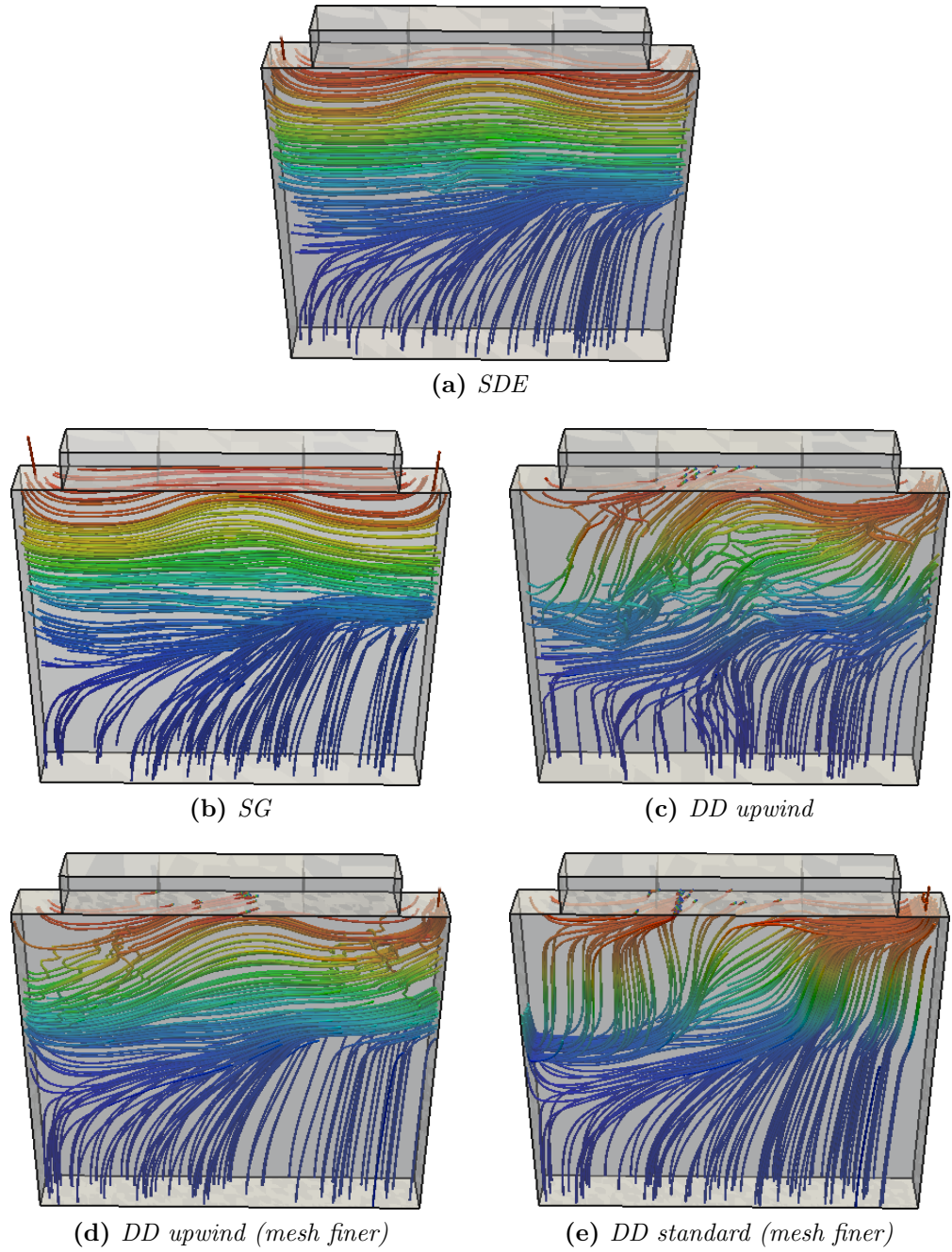


**Figure 5.5:** 1D plot p-n junction -  $V_A = 1.0[V]$ .

# Conclusions and future work

In this MD Thesis, we have presented

We accomplished our goal

A great effort has been spent in order to compute the current both at contacts and inside the device. In the first case we extended to the 3D framework the *residue method* with excellent results over all tests performed. About the current density we investigated the standard approaches using equation and . As expected the standard Drift-Diffusion formula gives bad results especially when the balance between the drift and diffusion component becomes critical. On the other side using the gradient of the quasi fermi potentials ensure good results neglecting the contact problems due to the boundary layers. Some modifications has been presented for both methods. We presented the extension to the 3D case of the Sharfetter-Gummel formula and we obtained good results

Although the boundary layer problems still remains at contacts.

Despite our best efforts, there are still many issues to be addressed:

- the conservation of the fluxes between neighbouring elements is a condition
- From the mathematical point of view, it would also be interesting to investigate the problems related to the fulfilment of the condition Zikatanov and proposed alternative algorithm in order to ensure the discrete maximum principle.
- Metodo SG vantaggi a livello computazionale, estensione naturale 3D del metodo SG 1D
- Metodo DD corretto risolve i problemi di contatto, più soggetto ad instabilità numeriche, rispetta una proprietà importante in maniera forte
- Possibilità di utilizzare questi metodi come nuovo schema di discretizzazione: problemi al contatto per il metodo SG (problema della me-

dia armonica con metodo misto).Per quanto riguarda il DD corretto bisogna pensarci.

# Bibliography

- [AF03] R. A. Adams and J. J. F. Fournier. *Sobolev Spaces*. Academic Press, 2003.
- [BCC98] R. E. Bank, W. Coughran, and L. C. Cowsar. The finite volume sharfetter-gummel method for steady convection diffusion equations. *Computing and Visualization in Science*, 1:123–136, 1998.
- [BGB00] Streetman Ben G. and Sanjay Banerjee. *Solid State electronic Devices*. New Jersey: Prentice Hall, 2000.
- [Can75] C. Canali. Electron and hole drift velocity measurements in silicon and their empirical relation to electric field and temperature. *IEEE Transactions on Electron Devices*, 22:1045–1047, 1975.
- [Chy58] A. G. Chynoweth. Ionization rates for electrons and holes in silicon. *Physical Review*, 109:1537–1540, 1958.
- [Deu74] P. Deuffhard. A modified newton method for the solution of ill-conditioned system of nonlinear equations with application to multiple shooting. *Numer. Math*, 22:289–315, 1974.
- [GH92] H Goebel and K. Hoffmann. Full dynamic power diode model including temperature behavior for use in circuit simulations. *Proceedings of the 4th International Symposium on Power Semiconductor Devices & ICs*, pages 130–135, 1992.
- [GS74] R. Gusmeroli and A. S. Spinelli. Accurate boundary integrals calculation in semiconductor device simulation. *Numer. Math*, 22:289–315, 1974.
- [Gum64] H. K. Gummel. A self-consistent iterative scheme for one-dimensional steady state transistor calculations. *Electron Devices*, pages 455–465, 1964.

- [HEML00] Thomas J.R. Hughes, Gerald Engel, Luca Mazzei, and Mats G. Larson. The continuous galerkin method is locally conservative. *Journal of Computational Physics*, 163:467–488, 2000.
- [IE83] Babuška I. and Osborn J. E. Generalized finite element methods: Their performance and their relation to mixed methods. *Numer. Anal.*, 20:510–536, 1983.
- [Jac84] J. D. Jackson. *Elettrodinamica Classica*. Zanichelli, 1984.
- [Jer96] J. W. Jerome. *Analysis of Charge Transport*. Springer, 1996.
- [LH80] W. Lochmann and A. Haug. Phonon-assisted auger recombination in si with direct calculation of the overlap integrals. *Solid State Communications*, 35:553–556, 1980.
- [Lom88] C. Lombardi. A physically based mobility model for numerical simulation of nonplanar devices. *IEEE Transactions on Computer-Aided Design*, 7:1164–1171, 1988.
- [MS83] G. Masetti and M. Severi. Modeling of carrier mobility against carrier concentration in arsenic-, phosphorus-, and boron-doped silicon. *IEEE Transactions on Electron Devices*, 7:764–769, 1983.
- [PC98] M. Putti and C. Cordes. Finite element approximation of the diffusion operator on tetrahedra. *Society for Industrial and Applied Mathematics*, 19:1154–1168, 1998.
- [PN] R. F. Pierret and G. W. Neudeck. *Advanced Semiconductor Fundamentals*, volume 6. Prentice Hall.
- [PTVF07] William H. Press, Saul A. Teukolsky, William T. Vetterling, and Brian P. Flannery. *Numerical Recipes, The Art of Scientific Computing*. Cambridge University Press, New York, 2007.
- [Qua08] Alfio Quarteroni. *Modellistica Numerica per Problemi Differenziali*. Springer Italia, Milan, 2008.
- [QV08] Alfio Quarteroni and Alberto Valli. *Numerical Approximation of Partial Differential Equations*. Springer, 2008.
- [Sal10] Sandro Salsa. *Equazioni a Derivate Parziali, metodi, modelli e applicazioni*. Springer Italia, Milan, 2010.
- [Sde13] *Sentaurus Device User Guide*. Synopsis Inc., 2013.

- [Sie84] Selberherr Siegfried. *Analysis and Simulation of Semiconductor Devices*. Springer-Verlag, Wien, 1984.
- [vOdM70] R. van Overstraeten and H. de Man. Measurement of the ionization rates in diffused silicon p-n junctions. *Solid-State Electronics*, 13:583–608, 1970.
- [VOT83] R. Van Overstraeten and M. S. Tyagi. Minority carrier recombination in heavily-doped silicon. *Solid-State Electronics*, 26:577–597, 1983.
- [XZ99] Jinchao Xu and Ludmil Zikatanov. A monotone finite element scheme for convection-diffusion equations. *Mathematics of Computation*, 68:1429–1446, 1999.
- [YT09] Taur Yuan and H. Ning Tak. *Fundamentals of Modern VLSI Devices*. Cambridge University Press, 2009.
- [ZL12] L. T. Zikatanov and R. D. Lazarov. An exponential fitting scheme for general convection-diffusion equations on tetrahedral meshes. *math*, pages 455–465, 2012.





# Ringraziamenti